Comprehensive Pneumology Center / Institute of Lung Biology and Disease (CPC/iLBD)
Helmholtz Zentrum München
and
Ludwig-Maximilians-Universität München

Dissertation
for the awarding of a Doctor of Philosophy
(Ph.D.)
at the Medical Faculty of the
Ludwig-Maximilians-Universität München

‘‘**Adipocytes mobilize in response to injury without plasticity**’’

Submitted by:

Shruthi Kalgudde Gopal

From:

Chickmagalur, India

On:

24.07.2020

Mit freundlicher Genehmigung der Ludwig-Maximilians-Universität München

First supervisor **:** Prof. Dr. Silke Meiners, CPC, Helmholtz Zentrum München

Second supervisor **:** PD. Dr. Claudia Staab-Weijnitz, CPC, Helmholtz Zentrum München

Direct supervisor **:** Dr. Yuval Rinkevich, CPC, Helmholtz Zentrum München

External Advisor **:** Dr. Siegfried Ussar, IDO, Helmholtz Zentrum München

Dean: **Prof. Dr. med. dent. Reinhard Hickel**

Date of oral defense:

10.08.2021

LMU LUDWIG-MAXIMILIANS-UNIVERSITÄT MÜNCHEN

Dean's Office
Medical Faculty

MMRS

Affidavit

Kalgudde Gopal, Shruthi

Surname, First name

Germany

Country

I hereby declare, that the submitted thesis entitled:

Adipocytes mobilize in response to injury without plasticity

is my own work. I have only used the sources indicated and have not made unauthorised use of services of a third party. Where the work of others has been quoted or reproduced, the source is always given.

I further declare that the submitted thesis or parts thereof have not been presented as part of an examination degree to any other university.

Munich, 12.08.2021

Place, date

Shruthi Kalgudde Gopal

Signature doctoral candidate

LMU LUDWIG-MAXIMILIANS-UNIVERSITÄT MÜNCHEN

Dean's Office
Medical Faculty

MMRS

Confirmation of congruency between printed and electronic version of the doctoral thesis

Kalgudde Gopal, Shruthi

Surname, First name

Germany

Country

I hereby declare, that the submitted thesis entitled:

Adipocytes mobilize in response to injury without plasticity

is congruent with the printed version both in content and format.

Munich, 12.08.2021

Place, date

Shruthi Kalgudde Gopal

Signature doctoral candidate

Table of Contents

Abstract

Cutaneous injury triggers cellular processes such as wound healing, tissue fibrosis, and scar development, which involve many different cell types. Successful regeneration after cutaneous injury requires timely coordinated actions of diverse cell types. Fibroblasts and adipocytes are two critical cell types in these processes and are thought to be displaying cellular plasticity. Cellular plasticity refers to the ability of a terminally differentiated cell type to take on the characteristics of another differentiated cell type. For example, an adipogenic fate gains plasticity towards a fibrogenic fate resulting in loss of cellular identity and normal function, with deleterious implications for regenerative healing.

Current research in the field does not provide concrete evidence to show the two cell types' inter-conversion capacity. Hence, it was crucial to make a head-on comparison of cellular and molecular signatures and features of these two cell types and show the fate of the two cell types upon injury. The results we obtained from this study enabled us to decipher the possible Fibro-adipogenic plasticity during wound healing and scar development.

In the first part of the study, we developed an ex-vivo 3D disease model termed "SCAD (Scar-like tissue in a Dish)" that can recapitulate specific wound healing and scar development processes in a dish setting. We used the SCAD model to study certain cell-specific functions and processes involved in scar development. An extracellular matrix (ECM) is a significant scar tissue component, which is synthesized and deposited predominantly by the activated state of a fibroblast called a Myofibroblast. Hence, we used a transgenic mouse line that labels scar-forming fibroblasts to characterize scar development processes. Our results showed collective migration and upregulation of cell adhesion molecule N-cadherin in scarring fibroblasts upon injury. To functionally validate N-cadherin as a critical target gene enabling fibroblast collective migration, we combined the Adeno associated virus-based gene targeting and CRISPR-cas9 based gene manipulation technologies. Blocking N-cadherin inhibited fibroblast swarming and collective migration, leading to reduced scarring in ex-vivo SCADs and animal models.

In the next part of the study, we uncovered the cellular plasticity features of fibroblast and adipocytes during scar development. We used transgenic mouse lines to label fibroblasts and adipocytes with a GFP reporter gene specifically. Evidence from transcriptomic signatures of both cell types by single-cell RNA sequencing showed that these cell types do not display cell plasticity but instead remain lineage-restricted. We further confirm lineage restriction with the ex-vivo scar model SCAD and time-lapse imaging and show that adipocytes reposition during injury, attain fibroblast-like morphology but do not transition into a fibrogenic fate. We also show that adipocytes migrate differently, deposit a meager amount of ECM, and do not transition into a myofibroblast. We conclude that adipocytes do not exhibit cellular plasticity in response to injury and remain as terminally differentiated types.

We can utilize the knowledge of molecular and cellular mechanisms of adipocyte and fibroblast plasticity to develop cell-type targeted therapies in wound healing, tissue fibrosis, and scar development.

I Chapter 1: Development of ex-vivo 3D scar models

1. Introduction

Scarring is a global concern where every year, about 100 million people acquire scars. Over 11 million people have keloids, and 4 million acquire burn scars, 70% of which occur in children. Among children, one in five of them require reconstructive surgery after a scar caused joint contraction. Scarring of the skin affects millions of patients, particularly children and burn victims, which causes a great deal of suffering. (A Bayat et al., 2003, Palmieri et al., 2003, Prasad et al., 1991, Sen et al., 2009, Sund B et al., 2000, Marshal CD et al., 2018). Scarring and impaired wound-healing are major clinical problems and a tremendous burden for patients and global healthcare systems, costing tens of billions of dollars per year in the U.S. (Jiang D et al., 2020).

Mammalian tissue injury typically results in a noticeable scar. Scar prevention consists of the principles of wound closure without traction or stress. It also includes avoiding infection and wound breakdown. The clinical phenotypes usually vary from a fine line scar, which is less severe, to hypertrophic, keloid, and scar contractures that are more severe forms of the scar (Bayat A et al., 2003). Impaired wound healing can cause abnormal and pathological scarring resulting in psychological and social distress, impairment of quality of life (Bock O et al., 2006), skin depression, stretch marks, disfiguring, and even restricted movement or physical disability. Excessive scarring can also have physical symptoms such as itching, stiffness, scar contractures, tenderness, and pain (Van Loey NE et al., 2008). The psychosocial effects of unaesthetic scarring include diminished self-esteem, stigmatization, disruption of daily activities, anxiety, and depression (Bakker A et al., 2013, Monstrey S et al., 2014).

Extensive research is ongoing to study scarring, as understanding the scar development mechanisms will pave the way towards achieving scarless regeneration. Various treatments exist for established scars, with varying effectiveness levels (Marshal CD et al., 2018). Burn scars are particularly challenging, and treatment primarily supports revision surgery to remove scarred skin. Existing treatments mainly focus on surgical excision, radiotherapy, or corticosteroids, or a combination of these procedures (Marshal

CD et al., 2018). Molecular and cellular therapeutics are gaining importance in other fields like cancer, and there is a broader scope of such therapies for pathologies like scarring (Qunakun L et al., 2016, Rhett J W et al., 2007). Wound healing and scar development processes are characterized at the cellular and molecular level, but truly successful molecular level anti-scarring agents do not exist. The development of anti-scarring molecules from bench to clinical use requires extensive screening and validation of potential candidate molecules. In parallel, driving the growth from target identification to preclinical development must involve robust and efficient in-vitro disease models to screen potential candidate molecules. Some agents have been tested for efficacy in treating scarring and fibrotic conditions, but the results are ineffective. Human recombinant TGFβ3 failed in phase III clinical trial on human scarring (NCT00432328). Similarly, a study involving the use of dermal fibroblasts to treat burn scars was terminated early (NCT01564407). EXC 001, CTGF (connective tissue growth factor) inhibitor, an antisense nucleotide which showed promising results in phase ll, but the current status is not available (Galiano RD, 2011). RXI 109, an RNAi-based inhibitor of CTGF, is currently in phase 1(NCT02246465).

A novel drug-based treatment that uses a specific molecular or cellular target in the scarring pathway will revolutionize scar treatment. It would potentially improve many patients' lives (Marshal CD et al., 2018).

1.1 Structure of the skin

Skin is the biggest organ; therefore, it is the most vital component in the body's overall health. The skin is an intricate and complex structure consisting of the epidermis and dermis, including the dermal adipocyte and subcutaneous fat layers (Takeo M et al., 2015). Epidermis, the topmost layer, is made up of keratinized stratified squamous epithelium, which acts as a protective layer preventing water loss, the barrier against mechanical injury and infection. Keratinocytes are the primary cell type. The dermis is the next layer below and is composed of fibrous connective tissue, consisting of collagen, elastic fiber, and other extracellular components. It provides elasticity, protects more deep layers of the skin, cushions the hair follicles, sebaceous glands, nerves, and blood vessels. Fibroblasts are the primary cell type of the dermis. The third main layer is the

subcutaneous fat layer, whose primary function is energy storage and thermoregulation. Adipocytes are the principal cell type of this layer of the skin (Fig. 1 A).

1.2 Introduction to scar development

Skin is continuously injured and regenerated, and during this process, connective tissue responds to the damage leading to a process called scarring (Krafts KP 2010). Injured tissue is sealed by the deposition of dense fibrous tissue, which usually results in a noticeable scar. Scars replace the original tissue with thick plugs of matrix fibers that tighten the tissue and reduce its flexibility, as seen in (Fig. 1 B) and described in (Huang et al., 1978, Palmieri et al., 2003, Correa-Gallegos D et al., 2019).

A.

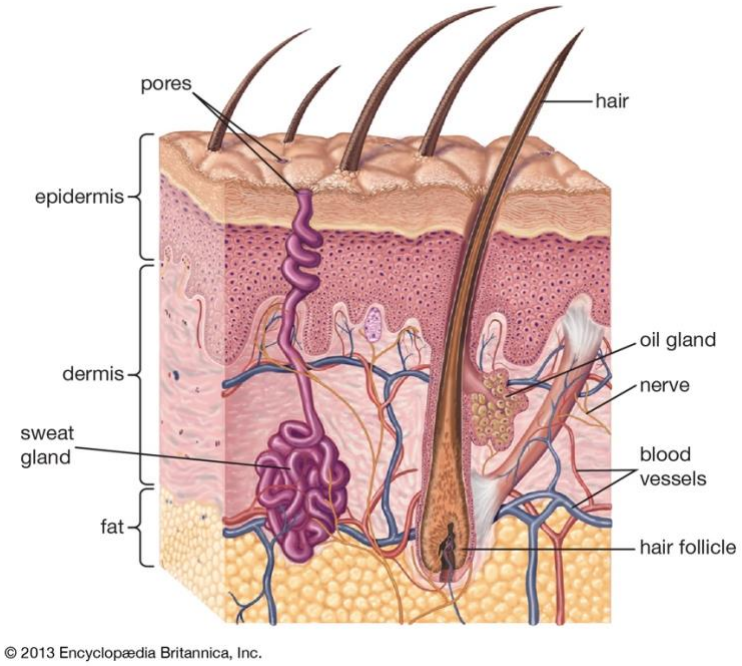

Structure of the skin

B.

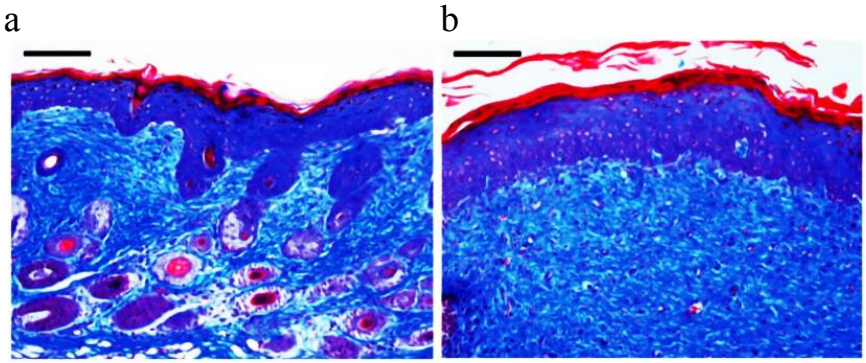

(adapted from Marshal CD et al., 2018)

***Figure 1**: **A**. Structure of skin. **B**. Histology of normal and scarred skin. Normal (a) and scarred (b). The hair follicle is present, the epidermis is normal in healthy skin, but in scarred skin, the hair follicle absent, epidermal thickening is seen, and cell proliferation is evident. Scale bar:100µm.*

1.3 Wound healing and scar development

Both wound healing and scar development processes go sequentially with much overlap, and the formation of pathological scar results due to impaired wound healing (Reinke JM, and Sorg H 2012). Wound healing occurs mainly in 4 stages: hemostasis, inflammatory, proliferative, and remodeling or restoration. (Negut I et.al., 2018, Mellott AJ et.al., 2016, Pinto AM et.al., 2020). Upon injury, a series of processes occur, and a series of events take place to repair the injured tissues.

Phase 1: Hemostasis Phase

Hemostasis is primarily coagulation and is the first phase of wound healing, which begins at the onset of the injury. Here the body activates the blood clotting machinery and mainly bringing platelets and fibrin clots to the site of injury. Enzyme thrombin helps form the stable fibrin clot to stop the blood flow (Fig. 2 Aa).

Phase 2: Inflammatory Phase

In the inflammatory phase, destroying bacteria and removing debris is brought about by neutrophils and macrophages. Preparing of wound bed for the growth of new tissue takes place. Neutrophils arrive first and populate between 24 and 48 hours after injury. Later, macrophages arrive to continue clearing debris. Macrophages secrete growth factors and proteins that attract other immune cells to the wound site to facilitate tissue repair. This phase often lasts 4 to 6 days and is associated with edema, erythema (reddening of the skin), heat, and pain (Fig. 2 Ab and B).

Phase 3: Proliferative Phase

Once the wound is clean, it enters the next phase, the Proliferative Phase, where the focus is to fill and cover the wound. The Proliferative phase features three distinct stages: 1) filling the wound; 2) contraction of the wound margins; and 3) covering the wound, re-epithelialization. During the first stage, shiny, deep red granulation tissue fills the wound

bed with connective tissue, and new blood vessels are formed. During contraction, the wound margins contract and pull toward the center of the wound. In the third stage, epithelial cells arise from the wound bed or margins and begin to migrate across the wound bed until the injury is covered with epithelium. The Proliferative phase often lasts anywhere from 4 to 24 days (Fig 2. Ac and B).

Phase 4: Remodelling or restoration Phase

During the restoration phase, the new tissue slowly gains strength and flexibility. Here, collagen fibers reorganize, the tissue remodels and matures, and an overall increase in tensile strength (though maximum strength is limited to 80% of the pre-injured strength). The Maturation phase varies significantly from wound to wound, often lasting anywhere from 20 to 25 days (Fig 2. Ad and B).

A.

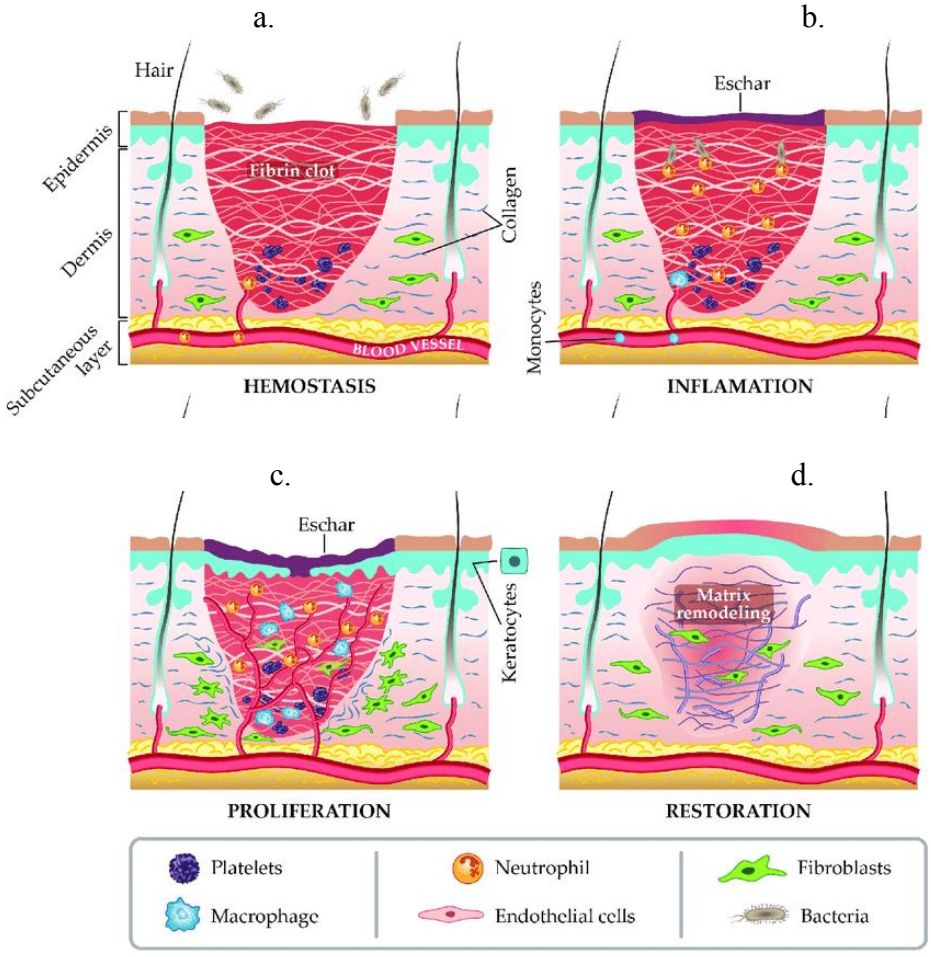

B.

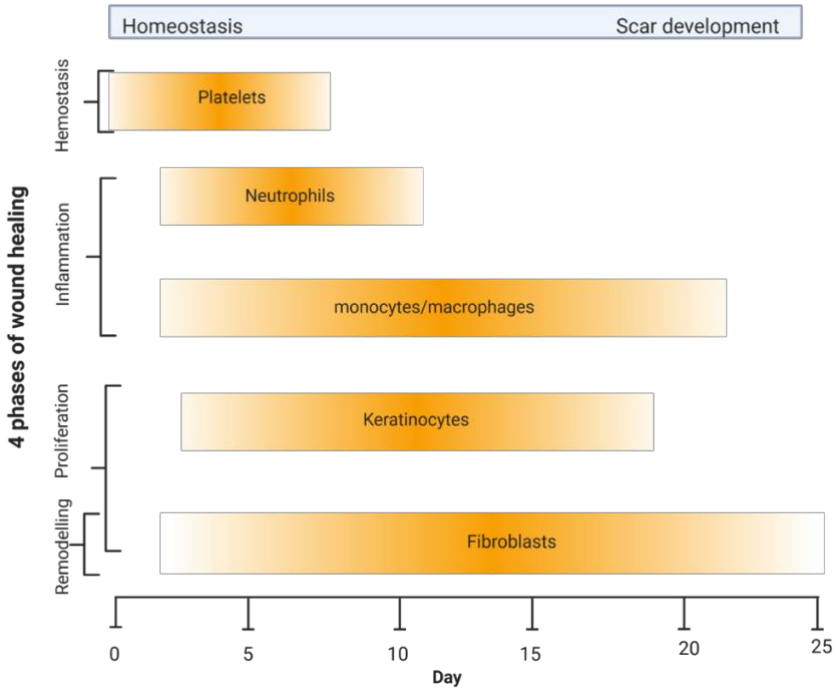

***Figure 2**: **A.** Four phases of wound healing (adapted from* Negut I et al., 2018) *and **B**. Involvement of different cell types from homeostasis to scar development. On the y axis is the number of days that a particular cell type is involved during the process of wound healing (edited from Marshal CD et al., 2018).*

The entire process involves an orchestrated contribution of many different cell types. Platelets respond immediately at the time of onset injury. In the inflammation phase, the immune system cells such as neutrophils and macrophages are prevalent from day 3 to day 21. In the proliferative phase, where re-epithelialization occurs by keratinocytes and blood vessel reconstruction by endothelial cells, it can last up to 20 days. In the remodeling phase, fibroblasts are involved in laying down collagen fiber that eventually covers the wound, leading to scar formation. Fibroblasts are present throughout all the phases up to more than 25 days from the onset of injury and are thus one of the crucial cells that contribute to scar formation. The remodeling phase sometimes last up to one year (Xue M and Jackson CJ 2015).

1.4 Types of scars

Scarring occurs both after accidental injuries and after surgery. It ranges from typical fine line scar to abnormal phenotypes. Some of the main types of abnormal scars are

widespread scars, scar contractures, hypertrophic scars, and keloid scars. (A Bayat et al., 2003, Mokos ZB et al., 2017 and Reviewed in Alster T.S. and Tanzi EL 2003, Brissett AE and Sherris DA 2001, Xue M and Jackson CJ 2015, Juckett G and Hartman-Adams H 2009, Goldenberg G and Luber AJ 2013).

1. **Widespread scars** appear as lines of surgical sutures look stretched, widened, typically flat, pale, soft, with no nodularity or elevation. Stretch marks after pregnancy are an example of widespread scars where the dermis and subcutaneous tissues are injured, but the epidermis is not (Fig. 3 A).

2. **Hypertrophic scars (H.S.)** are characterized by deposits of excessive amounts of collagen are raised scars confined to wound edges, are often red, inflamed, itchy, and even painful (Fig. 3 B).

3. **Contracture scars** occur due to a contractile wound-healing process that forms mainly after a burn or other injuries that resulted in a loss of a larger area of skin tissue that forms a scar pulling the edges of the skin together. They are fixed and rigid, which leads to physical deformities and movement restriction (Fig. 3 C).

4. **Keloids-** These are thick, pruritic, itchy bumps of darker scar tissue that grow beyond the injury site's edges or incision and invade the surrounding tissue. Keloids have the potential to regrow after being removed surgically. Keloids are referred to as benign fibroproliferative tumors characterized by excess collagen at previous skin injury sites. A histological examination of a keloid reveals larger, thicker, and more disorganized collagen fibers than those seen in normal skin (Fig. 3 D) (Har-Shai Y et al., 2010).

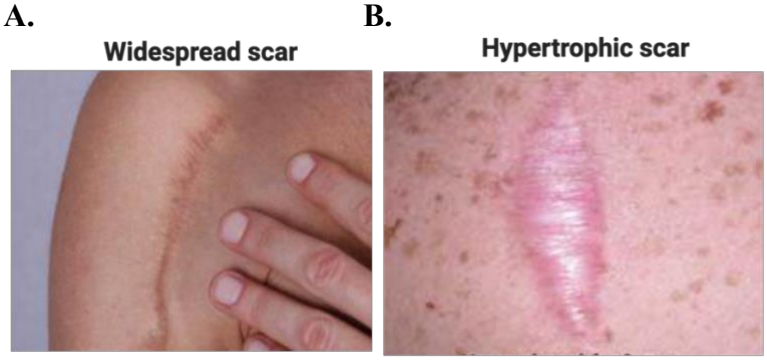

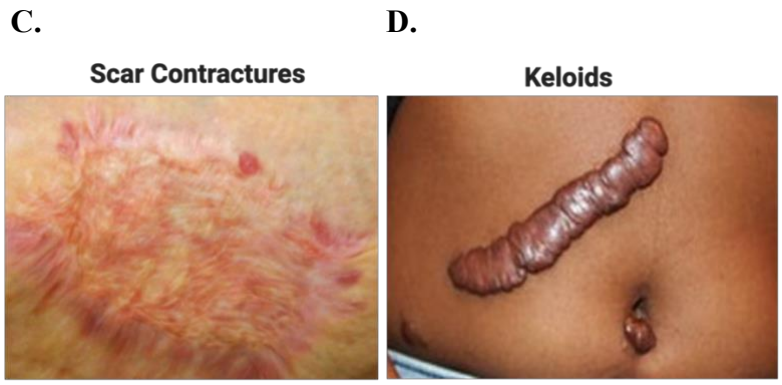

Figure 3**: **Examples of common scar types**. **A. Widespread scar. **B**. Hypertrophic scar. **C**. Contracture scars. **D.** Keloids.

1.5 Current scar treatment approaches

All current scar minimization treatments deal primarily with symptoms. Some of the treatments currently include the use of lasers and surgery. Photothermolysis is the commonly used method that involves laser resurfacing, and others include stem cell-based therapies, chemical peels, collagen injections, cortisone injections, surgical scar revision, radiation therapy, etc. (Bayat A et al., 2003). Silicone gel sheeting (J. Poston 2000, O'Brien L and Pandit A 2006), pressure therapy in the form of compression garments, and hydrotherapy are widely used mainly for hypertrophic burn scars. Laser- and light-based therapies are in use along with surgery and physical therapy (Waibel JS and Rudnick A 2015, reviewed by Brewin MP and Lister TS. 2014).

Cryotherapy tends to be limited to treating very small scars because of side-effects of pigmentation changes, skin atrophy, and pain. It has been used to shrink keloid scars (Har-Shai Y et al., 2011, Gauglitz GG, 2013). Radiotherapy, in combination with surgery, is an effective treatment of keloids. Brachytherapy, X-ray, and electron beam forms of radiotherapy have all been employed and usually adjunct therapy or secondary treatment. Ionizing radiation works by inhibiting proliferating fibroblasts, therefore decreasing the pathologic deposition of collagen. Radiotherapy is an effective treatment of keloids but is limited due to the risk of carcinogenesis (Al-Attar A et al., 2006, Block Let al., 2015).

Other anti-scarring therapies include injecting BTXA (Botulinum toxin type A) has been used in the treatment of hypertrophic scar (Zhang DZ et al., 2016, Scala J et al., 2019). Anti-inflammatory cytokine TSG-6 inhibited hypertrophic scar formation in a rabbit ear model where intradermal administration TSG-6 resulted in fibroblast apoptosis (Wang H et al., 2015). Anti-angiogenesis therapy is effective in Hypertrophic scar tissues that contain more microvessels. Anti-vascular endothelial growth factor (VEGF) monoclonal antibody effectively inhibited angiogenesis in scar tissues and ECM production (Kwak DH et al., 2016, Wang P et al., 2016, Shirakami E et al., 2020). Lipofilling or lipografting, where the therapeutic effect is brought by Adipose tissue Derived Stem Cells (ADSC) is another promising approach to treat fibrotic scars (Spiekman M et al., 2017). Other physical therapies include massage, ultrasound, medical tattooing/camouflage, static electricity, and pulsed electrical stimulation. These are yet to be proven by randomized controlled trials (Baker R et al., 2010).

The therapies mentioned above are in clinical practice with moderate outcomes, or some have evidence based on only animal models. Therefore, it is vital to understand wound healing and scar development mechanisms to develop effective molecular level therapies for treating aberrant scars.

1.6 Gene delivery tools for skin

Developing molecular therapies requires efficient and robust methods to manipulate genes to study genes' function in a disease setting. Most methods used are Non-Viral based or Viral based methods.

1.6.1 Non-Viral based: Methods such as electroporation using an electric pulse, Lipofection, a lipid-mediated DNA-transfection process. These methods are well established for 2D cultures and cell lines.

1.6.2 Viral-based: Here, gene delivery uses a virus's ability to inject its DNA inside a host cell. A gene that is intended for delivery is packaged into a replication-deficient viral particle. Viruses used to date include Retrovirus, Lentivirus, Adenovirus, Adeno-Associated Virus (AAV), and Herpes Simplex Virus. AAV offers many advantages over other commonly used viruses such as adenovirus and lentiviral approaches.

Adeno-associated viruses (AAVs)

Adeno-associated viruses are naturally occurring replication-incompetent parvoviruses. They were earlier found as contagions in stocks of simian adenovirus and humans (Blacklow NR et al., 1967). AAVs are known to be an efficient tool for gene delivery for some time now. As the wild-type AAV genome can persist in tissues for a long term, the use of recombinant AAV (rAAV) vectors for gene transfer has become famous (Muzyczka N et al., 1992, Zhong L et al., 2004, Jayandharan GR et al., 2012). Capsids of different serotypes can combine (package) recombinant viral genomes flanked by ITRs of serotype AAV2 to form `pseudotyped' vectors. These are developed for many gene delivery applications (Joshua C Grieger and R Jude Samulski, 2012). The AAV has a linear ssDNA (single-stranded DNA) genome with a non-enveloped small capsid (Muzyczka N.et al.,1992, Berns K I 1990). The genome is small, about 4.7 kb, and consists of rep and cap genes flanked by two 145 bp long inverted terminal repeat (ITR) sequences on both ends. With alternative splicing and two transcription initiation sites, the rep gene directs the expression of 4 different Rep proteins that are important for the life cycle of AAV (Naso MF et al., 2017). AAVs have minimal toxicity, low pathogenicity, sustained viral persistence targeting specific cell and tissue types. Packaging a cell/tissue-specific promoter enables Tissue-specific targeting.

1.7 Wound healing and scar development in a dish

Biomedical research involves understanding the diseases' cellular and molecular basis to develop cell-type targeted diagnostics and therapies. Mouse models are commonly used vertebrates to achieve this on a laboratory scale. The use of animal models poses a challenge for high throughput studies and the need for animal protocol development and approvals. 3R principle of Reduce, Reuse, and Recycle of animal models encourage alternative ex-vivo disease models. On the other hand, 2D monolayer cell culture models and in-vitro 3D wound healing models such as 3D reconstructed human epidermis from keratinocytes (Smits JPH et al., 2017) or scratch assays (Liang CC et al., 2017) often have limitations as they are derived from single-cell types. These models are limited in mimicking in-vivo disease outcomes. Some of the other 2D models include co-culture of fibroblasts, endothelial cells, and keratinocytes from human keloid scars on a culture dish. These are cultured on plastic surfaces on a culture dish, which drastically changes

individual cell types' behavior and functional outcomes (Seo BF et al., 2013). A consolidated list of existing skin explant models currently available is summarized in Table 1.

In between in-vivo animal and 2D monolayer/3D, in-vitro models are the 3D ex-vivo tissue models—these possess both native structure and tissue architecture similar to in-vivo, providing throughput capability of an in-vitro model. 3D ex-vivo disease models enable co-culture of different cell populations to decipher the role of cell-cell, or cell-ECM interactions, cellular morphology, chemical and physical forces experienced by cells are in a more realistic microenvironment. 3D models recapitulate physiology and disease (Jackson EL and Lu H. 2016, Hoarau-Véchot et al., 2018), (Fig. 4).

3D ex-vivo disease models are amenable for high-throughput studies, including small molecule-based chemogenomics, monoclonal antibodies screening, functional assay development, mutation biology and associated diseases, imaging of cell-cell and cell-ECM interactions (Hoarau-Véchot et al., 2018). Moreover, recent advancements in live imaging of tissues with unprecedented depth and details enable 3D disease models to be widely used for understanding underlying biological mechanisms and disease characteristics (Jiang D et al., 2020).

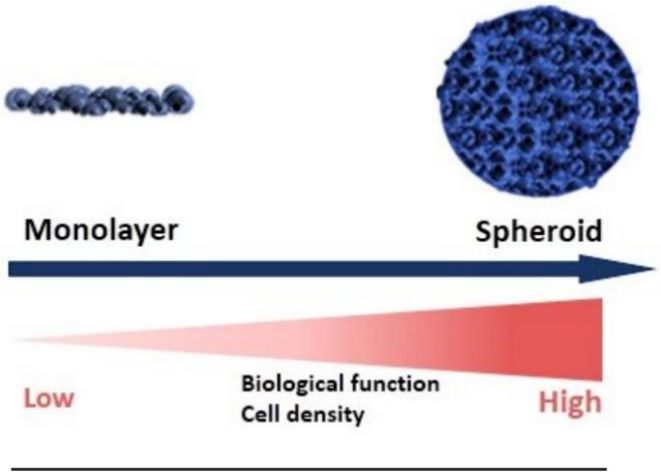

Figure 4: *Advantages of 3D models over 2D monolayer culture (adapted from* Hoarau-Véchot et al., 2018).

Reference	Species	Purpose of the assay	Name of the model	Transfectibilty	Neonatal or Adult
Mendoza-Garcia J et al., 2015	Human	Evaluation of Photodynamic therapy on wound healing	WHOC (Wound Healing Organ Culture)	No	Adult skin
Xu W et al., 2012	Human	Re-epithelialization	HESC (human ex-vivo skin culture)	No	Adult skin
Corzo-León DE., 2019	Human	To model skin fungal infections	Ex-vivo human skin model	No	Adult skin
Géniès C et al., 2018	Human, Porcine	Drug metablism and toxicity	Pig, human skin explant model	No	Adult skin
Alves DR., 2018	Porcine	Investigating burn wound infection	Ex-Vivo Burn Wound Model	No	Adult skin
Ng KW et al., 2010	Human	Intradermal vaccination, tissue integrity, Langehans cell behaviour	Ex-vivo human skin model	Yes, Microneedle facilitated DNA delivery	Adult skin
Syed F et al., 2013	Human	Evaluation of antifibrotic compounds in skin scarring	Keloid organ culture (OC) model	Yes, siRNA	Adult Keloid
Neil JE et al., 2020	Human	Pharmacodynamic use, Skin irritant studies	Human Explant Skin Culture (HESC)	No	Adult skin
Kendall AC et al., 2017	Human	Lipid functions in skin	Human skin organ culture model	No	Adult skin
Faway É et al., 2016	Human	Modeling dermatophytosis	Reconstructed human epidermis	No	Adult skin
Attia-Vigneau J et al., 2014	Human	To recapitulate aging-induced dermal changes	Skin explant model	No	Not stated
Maboni G et al., 2017	Human	Studying anaerobic bacterial infection	3D skin ex -vivo model	No	Adult skin
Burd DA et al., 1990	Sheep	To investigate fetal wound healing	In-vitro explant model	No	Sheep fetal skin

Table 1: *Summary of literature on ex-vivo skin models*.

Corzo-Leon DE et al., 2019 showed that their explant model can be used to evaluate responses from infections caused by fungus *Trichophyton rubrum*. They were able to evaluate the effects using a broad range of assays such as gene expression anlysis by qPCR and proteomic analysis. They employed imaging methods such as confocal and electron microscopy, to evaluate skin cell viability and fungal morphology. Géniès C et al., 2018 made a one on one comparison of a porcine and human explant model and showed that porcine skin is more competent metabolically. They proposed that procine skin explant model can used as tool for studying the effect of small molecule candidate before testing in human-derived tissues. Syed F et al., 2013 evaluated antifibrotic therapies and reported the first functional evidence for testing antifibrotic compounds in keloid disease. Kendall AC et al., 2017 using their model showed the effects of n-3 polyunsaturated fatty acids on cutaneous ceramides present the in skin. Neil JE et al., 2020 sheds light on the fact that vitro models can ease high-throughput and affordable evaluation of novel therapeutics, but ex-vivo systems can better forsee both beneficial and unfavourable in-vivo effects. Their model was stable over 9 days without any adverse physiological outcomes that were

related tissue integrity, barrier function and metabolic stability. However, none of these models showed mechanisms of scar developmet or molecular level manipulation of genes to study fuctional outcomes of a particular target gene.

2. Aim of the study

We aimed to develop an ex-vivo skin model to recapitulate scar development in a dish.

Features of an optimal ex-vivo scar model

1. Dermal tissue composition with native architecture consisting of different cell types will be an ideal set up.
2. Optimal culture conditions that include cell culture media, duration of culture must be closer to in-vivo scar formation timelines.
3. The model must be amenable for histological analysis such as biochemical and immuno fluorescence-based analysis of the tissue.
4. The model must be transfectable to identify and validate molecular targets of scar development.
5. The model must be amenable for imaging in great detail to understand fundamental biological processes.
6. The model should be easily adapted to high-throughput workflows such as small molecules, peptides, or antibody screening. This will potentially help in identifying lead molecules in treating scars.

3. Results

3.1 Overview of the 3D ex-vivo scar models

Hanging drop comprised of dermal aspirates. Dermal aspirates were prepared using the dorsal back skin of mice, which are >500μm (see methods for detailed protocol), thus comprising the skin's tissue composition. Droplets of dermal aspirates were cultured in a controlled environment using optimal fibroblast cell culture media, CO2, and O2 supply (Fernandes IR et al., 2016). This method provided a means to generate tissue-like dermal spheroids or cellular aggregates. The dermal aspirates are in direct contact with each other and extracellular matrix components. There was no requirement for a piece of specialized equipment. We termed the dermal aspirates or spheroids as "Dermastilla." Histological analysis was possible for molecular and biochemical analysis in this physiologically relevant model.

SCAD is an ex-vivo skin tissue explant, a 2mm biopsy punch excised from newborn mice's dorsal back skin. It consists of epidermis, dermis, DWAT (Dermal white adipose tissue), Panniculus Carnosus (P.C.) muscle, and subcutaneous fascia layers of the back skin, thus incorporating various skin cell types and cutaneous layers that we could use to study the multiple mechanisms of skin healing.

Most current explant techniques are tailored for studying epidermal healing and are not suitable for studying scar formation processes (Table 1). For example, most assays lack subcutaneous skin layers. Skin assays are also grown dermal side down, permitting scar-precursors to vacate the explant. Current assays do not model or answer how scars faithfully develop, why different skin locations react differently to injury, and how different fibroblast lineages behave, leading to scarring or regeneration. Advanced ex-situ skin assay that uniformly develops contraction and scars that could answer these critical questions remains to be developed and standardized.

Whole explants of skin tissue maintained were optimized culture conditions to get the best possible outcomes for recapitulating scar formation in a dish. Various methods were tried, including culturing explants as floating in complete media, culturing by placing on Matrigel as a support matrix, a sandwich of two explants that prevented bending of

explants, fixing the explants on to the culture dish with in-vivo glue, and culturing on a nylon membrane. Controlled cell culture conditions with optimal media and temperature were used in all methods and histologically assessed for scar development processes such as ECM deposition.

The ex-vivo skin explant is SCAD for "SCar-in-A-Dish," which overcomes the above limitations. Skin explants are all-inclusive of epidermal, dermal, and subcutaneous layers and are grown dermal-side up. Under these conditions, explants maintained the cellular complexity of native skin and developed scars with contraction within 5 days. We combine SCADs with live imaging to witness how scars develop from their authentic cells-of-origin for the first time (Jiang D et al., 2020).

3.2 Hanging drop model development

In the hanging methods, droplets of dermal cell aspirate are placed on top of the petri dish lid, and the lid is placed on the dish. The droplets are hanging on the lid of the dish. Sterile water was added to the dish to hydrate the chamber, preventing the drops from drying. The aspirates later aggregate to form spheroids when placed in the form of a hanging drop for over 5 days (Fig. 5 A and B). Dermal spheroids (Dermospheres), similar to organoids in general, were termed "Dermastilla." Dermastilla's were generated in multiple droplets and used for histological characterization.

Each Dermastilla was about ~200µm. Before cryosectioning for histological analysis, each Dermastilla was encapsulated in Matrigel for ease of handling. Haemotoxylin and Eosin staining showed the presence of multiple cells (nuclei) within the organoid. Immunofluorescence staining confirmed the presence of Fibronectin1 positive cells on day 5, suggesting that the majority of organoid has fibroblasts depositing matrix (Fig. 5 C). Dermastillas were further assessed for transfectability, and transfection carried out using eGFP plasmid DNA. Although the organoid itself exhibited strong autofluorescence, there were bright patchy spots of eGFP fluorescence in the transfected Dermastillas (Fig. 5 D).

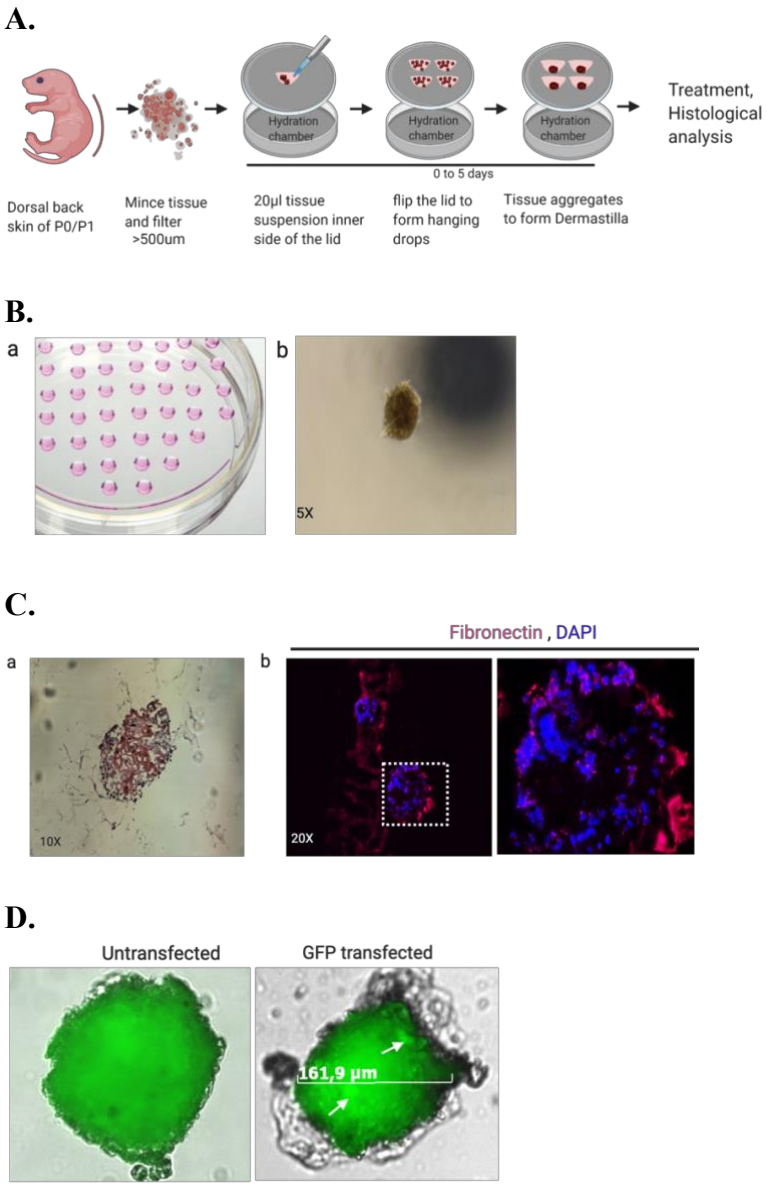

Figure 5: ***Development of Hanging drop model overview***. ***A.*** *Scheme of "Dermastilla" generation.* ***B.*** *(a) Photo showing Dermastilla hanging upside down on the lid of a Petri dish. Each drop contains 20µl of dermal aspirates suspended in complete culture media. (b) Representative bright-field image of a single Dermastilla.* ***C****. Histological assessment of Dermastilla. (a). H and E staining showing multiple cells (as seen by nuclei staining in blue) on the outer periphery of the Dermastilla. Each Dermastilla is surrounded by thin fibers of Matrigel that were used for encapsulation. (b) Immunofluorescence staining of dermastilla. 3D spheroidal structure of dermastilla with multiple cells positive for fibronectin.* ***D****. Dermastilla transfected using Lipofectamine 2000 and pMAX GFP plasmid DNA. Autofluorescence was observed in both untransfected and transfected samples. GFP transfection shows bright GFP spots marked by white arrows.*

3.3 'Scar in a dish' model development

Skin explants developed consistent and robust scars with characteristics and cellular complexity and developed uniform scars over 5 days (Fig. 6 A). The scars that developed ex-situ were morphologically similar to in-vivo scars in terms of architecture, extracellular matrix (ECM) composition, and cellular origins. Histologic sections revealed masses of fibroblasts that developed increasingly, creating a plug of collagen fibers. These plugs formed scars at the center of the skin when cultured for over 4 to 5 days. Re-epithelialization was seen when the epidermis gradually migrated over the skin circumference, and on day 5, had covered the scar (Fig. 6 B) entirely. On day 4 of the explant assay, immunolabelling of fibrillar matrix proteins fibronectin, collagen I, and collagen III was found aligning in the scar region. Pdgfr positive cells were also found populating in the scar center. These observations were consistent in both (culture by floating and culture on Matrigel) the methods of culturing SCADs. (Fig. 6 C).

Histological analysis of explants cultured on Matrigel showed that these explants retained small amounts of Matrigel, which interfered during the examination of extracellular matrix components. Hence, the floating method of explant was used for all further experiments, bypassing the need for Matrigel. The cultured explants generated scars that resembled scars that develop in native physiologic skin wounds using the floating method. As these explants served as a promising model to study scarring phenomena in a dish, they were termed `Scar in a dish' or SCAD.

We further characterized the explants by 3D imaging of whole-mount SCADs in unprecedented detail. Multi-photon microscopy allowed tissue imaging up to 500µm and enabled imaging of fixed whole-mount explants with a detailed overview of the cellular architecture. Explants were immunostained for common ECM proteins, and we observed enrichment of matrix proteins such as fibronectin, collagen1, and elastin in day 5 SCADs. Fibrillar matrix proteins like fibronectins and collagen1 were abundant but with no elastin protein, just like we see in animals' scar tissue. The second harmonic signal from multi-photon also enhances fibrillar collagens in the scar center (Fig 6. D). These SCAD features allowed us to study various scar formation processes, thus recapitulating specific processes of scar formation in a dish.

A.

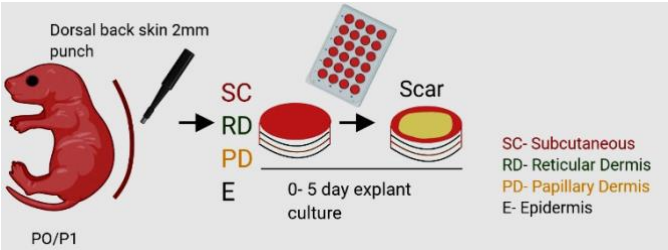
Dorsal back skin 2mm punch
SC
RD
PD
E
Scar
0- 5 day explant culture
SC- Subcutaneous
RD- Reticular Dermis
PD- Papillary Dermis
E- Epidermis
PO/P1

B.

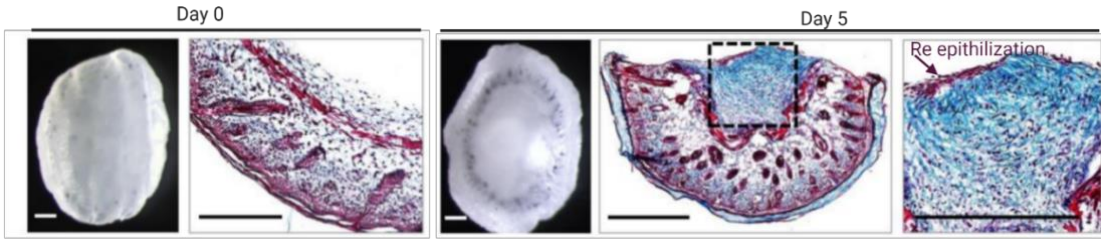
Day 0
Day 5
Re epithilization

C.

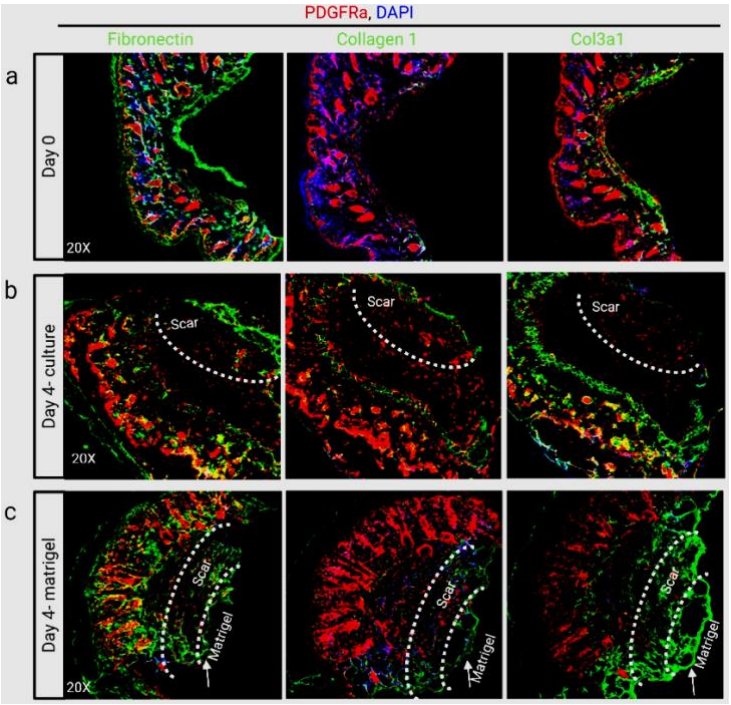
PDGFRa, DAPI
Fibronectin
Collagen 1
Col3a1
a
Day 0
20X
b
Day 4- culture
Scar
20X
c
Day 4- matrigel
Scar
Matrigel
20X

D.

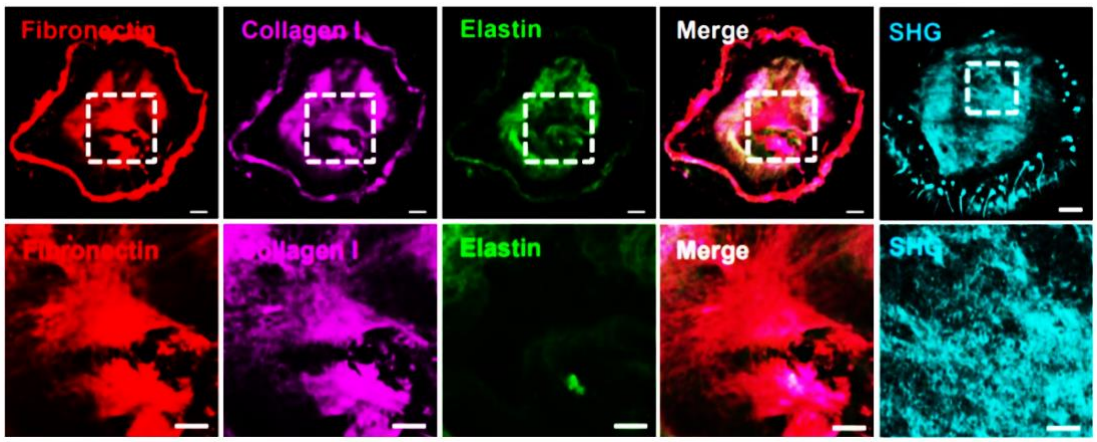
Fibronectin
Collagen I
Elastin
Merge
SHG

Figure 6. Overview of SCAD model and histological characterization: ***A.*** *Scheme of SCar in A Dish (SCAD) assay.* ***B.*** *whole-mount bright-field images and Masson's trichrome staining with collagen blue of fresh SCAD (day 0) and after 5 days in culture (day 5). Day 5 SCAD shows increased cell proliferation along with deposited collagen fibers and re-epithelialization in the scar center. Day 5 shows a further increase in cells in the scar center.* ***C****. Immunostaining of SCAD cryosections using fibroblast marker PDGFRa and extracellular matrix proteins Fibronectin 1, Collagen 1, and Col3a1.* ***D****. 3D Multiphoton images obtained post-whole-mount immunostaining of fibronectin (red), collagen I (magenta), and elastin (green) in SCADs at low (upper panel) and high (lower panel) magnification. Fibrillary collagens represented by second harmonic generation (SHG, cyan) signal in SCADs at low (upper) and low (lower) magnification. Scale bars: Scale bar: B=500µm, D=100µm upper panel, and lower panel=30µm.*

3.3.1 Molecular manipulation of SCAD

Next, to study gene function in a dish setting, we tested the SCAD's ability to be transfectable. Skin is one of the most challenging organs to be transfected. We employed non-viral methods such as 1. Lipofection – Lipid mediated transfer, 2. Electroporation uses electric pulses to create pores on the cell membrane, which in turn allows DNA transfer into the cell. 3. Viral-based gene delivery methods such as the use of an AAV.

Lipofection transfected Whole-mount SCADs along with the use of pMAX GFP plasmid DNA. Post transfection, SCADs were cultured for 72 to 96 hours, and GFP transfection coverage was assessed by confocal imaging. Next, whole-mount SCADs were transfected by electroporation and pMAX GFP plasmid DNA. SCADs were cultured for 72 hours, and GFP transfection coverage was assessed by confocal imaging (see methods section for protocol). These two approaches showed low transfection coverage, as seen by confocal microscopy (Fig. 7. A).

To efficiently transfect SCAD, we next used Viral based AAV. AAVs can be produced in an S1 laboratory (See attached document for guidelines from the German central commission (ZKBS) for biological safety about the classification). We needed to choose

the serotype with efficient skin tissue tropism among 12 commonly known serotypes of AAV viruses for transduction across multiple tissues. Hence, we first optimized the entire workflow of production and purification of AAV particles using AAVpro HEK293T producer cell line and reagents from Takara bio (Fig. 7 B and C, see methods for a detailed protocol for generating high titer AAV). We tested three serotypes, AAV serotype 5, 6, and 8, for skin tissue tropism (Carmela Zincarelli et al., 2008). Histological analysis of transduced SCADs confirmed AAV serotype 6 to have better transduction efficiencies. We observed nearly 80% of the cells in the SCAR region were transfected (Fig. 7 D). Low epidermal transduction was seen. Whole-mount SCAD transduction followed by 3D deep tissue imaging using 2-photon microscopy further confirmed higher transduction coverage of SCAD using AAV serotype 6 (Fig. 7 E).

A.

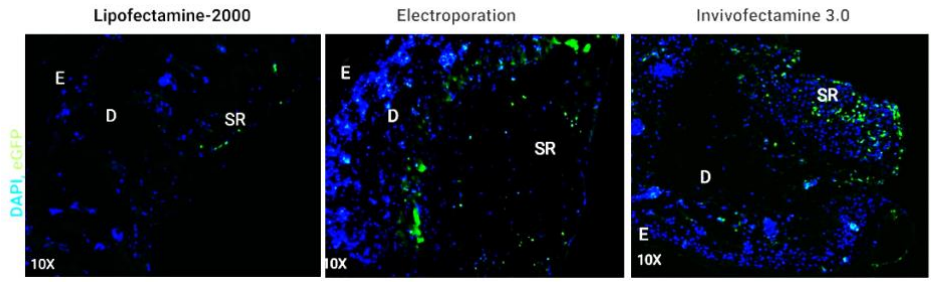

B.

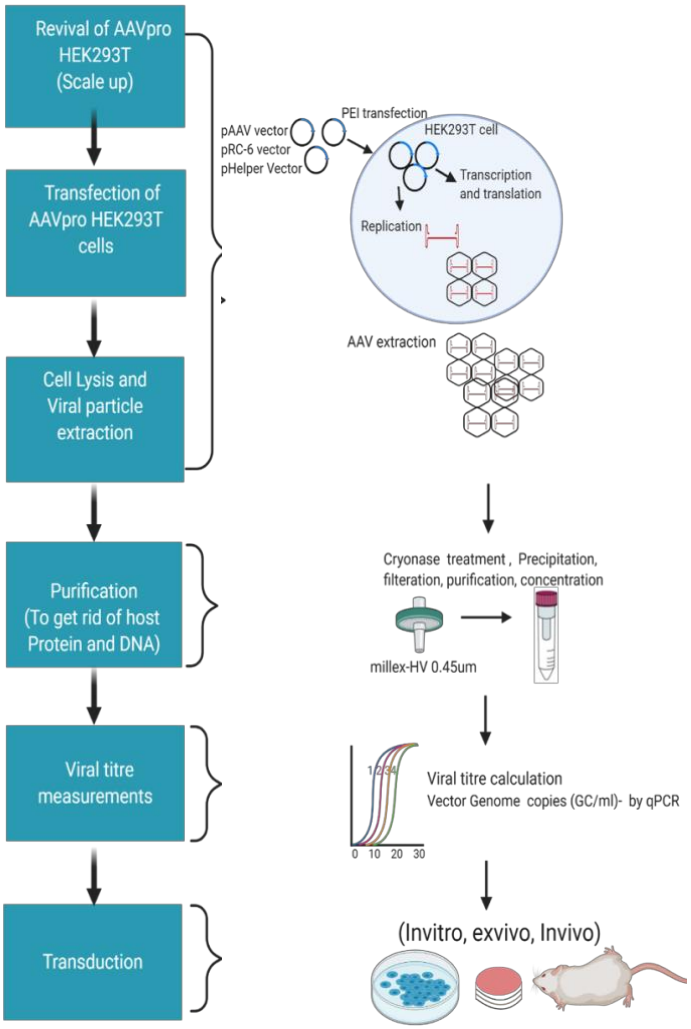
Revival of AAVpro HEK293T (Scale up)
Transfection of AAVpro HEK293T cells
Cell Lysis and Viral particle extraction
Purification (To get rid of host Protein and DNA)
Viral titre measurements
Transduction

C.

pAAV vector
pRC-6 vector
pHelper Vector
PEI transfection
HEK293T cell
Transcription and translation
Replication
AAV extraction
Cryonase treatment , Precipitation, filteration, purification, concentration
millex-HV 0.45um
Viral titre calculation
Vector Genome copies (GC/ml)- by qPCR
0 10 20 30
(Invitro, exvivo, Invivo)

D.

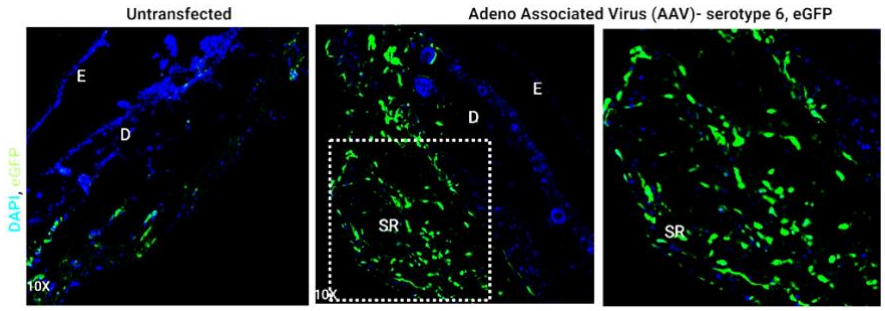
Untransfected
Adeno Associated Virus (AAV)- serotype 6, eGFP
DAPI, eGFP
E
D
SR
10X

E.

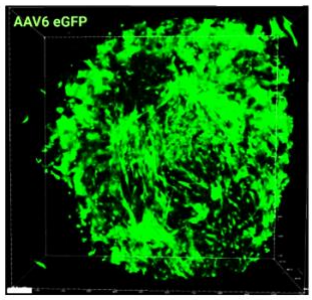
AAV6 eGFP

Figure 7. SCAD Transfection approaches A. *Cryosections of SCAD showing low transfection efficiency in conventional methods such as Lipofection, Electroporation, and use of an alternative Lipofection based reagent called. Invivofectamine 3.0.* ***B.*** *Overview of AVV generation and purification workflow.* ***C.*** *Scheme of AAV production, purification, and downstream quality control processes.* ***D.*** *Transduction of SCADs with the AAV6 eGFP virus. Good transfection efficiency is seen in the center of the SCAD, where the scar forms.* ***E.*** *The whole-mount image of AAV6 eGFP transduced SCAD Whole-mount image taken using Multiphoton microscope, showing eGFP transduced cells in SCAD. E- Epidermis, D-Dermis, SR-Scar Region. Scale bar:100µm,*

3.3.2 Molecular manipulation of SCAD by AAV and CRISPR -Cas9

Next, we combined both AAV and CRISPR-Cas9 approaches, enabling functional validation of the target gene such as N-cadherin (Jiang.D et al., 2020). Engrailed positive fibroblasts (EPFs) contribute to scar formation in adults (Rinkevich et al., 2015; Jiang D et al., 2018). Upon live imaging of SCADs from Engrailed1(En1+) Cre positive mice, we observed swarming and aggregation of fibroblasts during movement to the scar center (Jiang et al., 2020). Fibroblast aggregation requires cell-cell adhesion. To determine which adhesion molecule specifically was involved in swarming, we tested a panel of candidates for co-localization with EPFs in the scar area. Interestingly a one-to-one co-localization of N-cadherin was found (Fig. 8 A). Among other adhesion molecules, such as integrins, failed to co-localize. How- ever, the downstream effector of N-cadherin, α-catenin, did co-localize with fascia EPFs and N-cadherin in the scar area, consistent with a potential role for this molecule in swarming and scarring. Full-thickness wounds were generated to test if our findings from SCADs occur in animals. We found that N-cadherin's upregulation in in-vivo wounds mimics the N-cadherin expression found in SCADs (Jiang D et al., 2020).

We combined the Adeno associated viral approach and CRISPR cas9 gene-editing technology to efficiently knock out the N-Cadherin gene in En1 positive scar-forming fibroblasts. Multiple guide RNAs were designed against exon 1 of the murine N-cadherin gene. We generated high titers of the AAV6-eGFP-NCadherin-gRNA virus and AAV6-

eGFP control virus to knock out N-cadherin in SCADs. See methods for a detailed protocol for producing and purifying high titer AAV for ex-vivo and in-vivo application.

SCADs were made from full-body Cas9 mice to knock out N-cadherin ex-vivo. Transduction was carried out using AAV6-gRNA GFP virus and AAV6-GFP control viral particles (see methods for transduction protocols). We observed a significant reduction in N-cadherin expression in the gRNA transduced SCAD (Fig. 8 B) compared to control SCAD.

A.

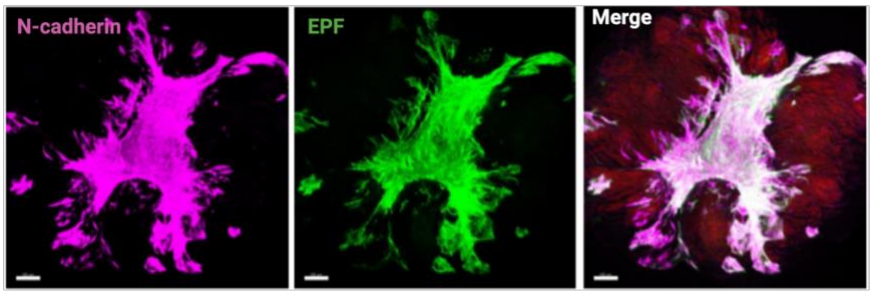

B.

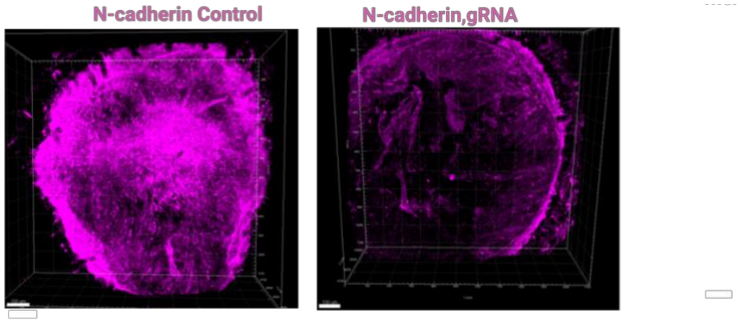

Figure 8. N-Cadherin knockdown ex-vivo and in-vivo by combining Adeno associated viral approaches and CRISPR- cas9 gene editing reduced scar formation. *N-cadherin was locally knocked out around wounds on Ncad $^{fl/fl}$ mice by injection of Cre expressing the AAV6-Cre-GFP virus. AAV6-GFP virus served as control. (**A**) whole-mount 3D immunolabeling of N-cadherin (magenta) in En1 Cre positive SCADs. EPFs co-localize with N-cadherin. (**B**) Whole-mount immunostaining against N-cadherin in control, as well as AAV6-N-Cad-gRNA, transduced SCAD. A. and B. Scale bar:100µm.*

To knock out N-Cadherin in-vivo, we injected AAV6 viral particles expressing Cre recombinase into the fascia surrounding wounds in N-cadherin floxed mice (Ncadfl/fl), which contains loxP sites flanking exon 1 of the N-cadherin gene. Upon histological

analysis, the transduced Cre-expressing fascia fibroblasts around wounds showed loss of N-cadherin expression. Cre- expressing virus resulted in a 65% reduction of N-cadherin expression in the scar region when compared to control (Fig. 8 C, D and E). Quantitative analysis revealed reduced scar area and width evidenced by whole-mount macroscopic (Fig. 8 F and H) and histologic analyses compared to the control virus (Fig. 8 G and I). More notably, in the histologic sections, transverse views of scars demonstrated the centripetal pattern of collagen fibers in the scar's center and were disrupted by the N-cadherin knockout (Fig. 8 H).

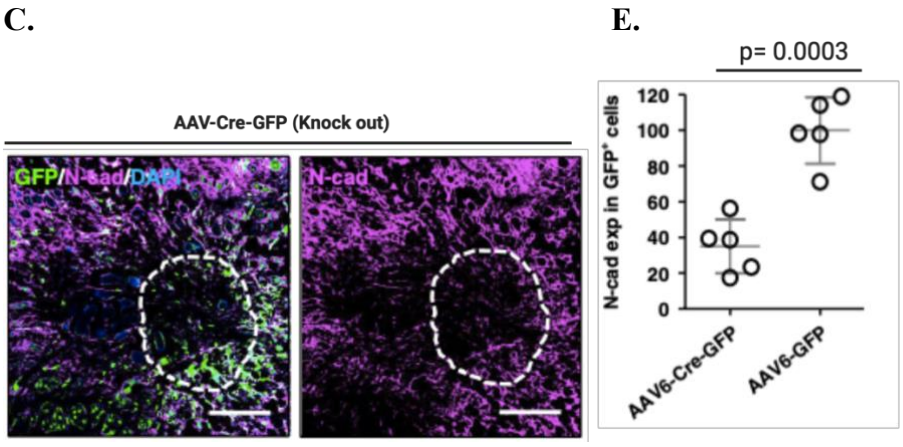

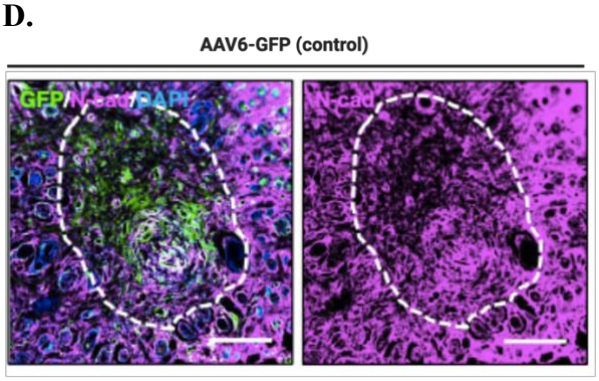

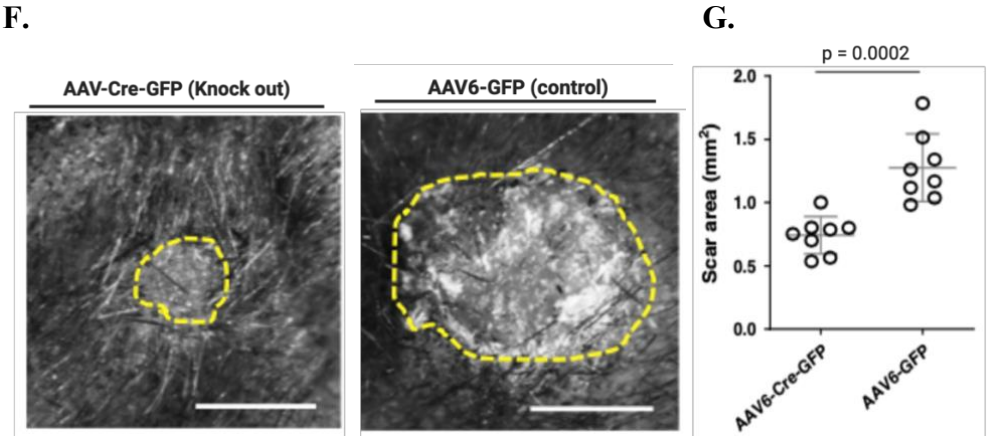

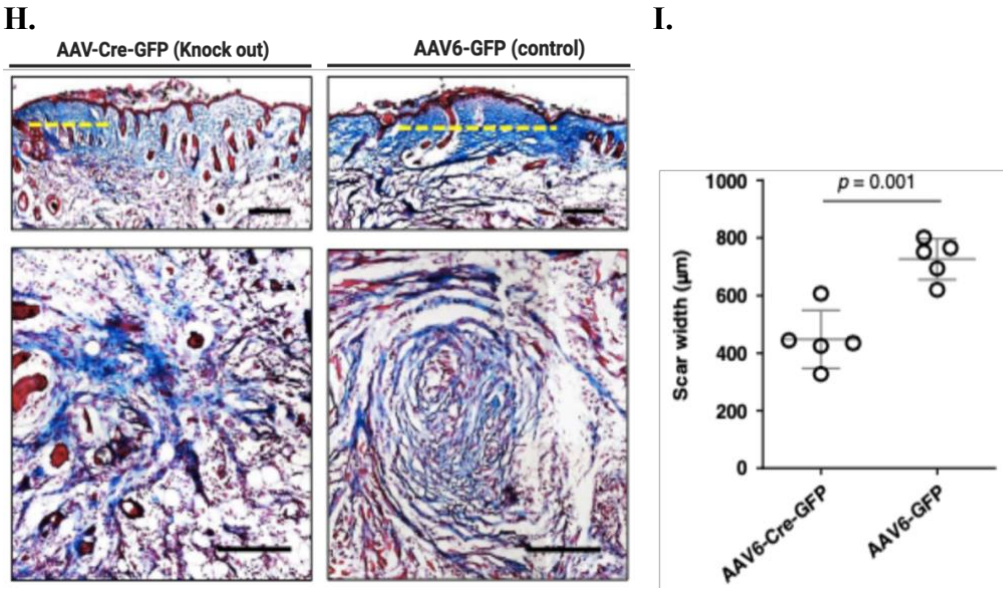

Figure 8. (C-I): N-cadherin knockdown ex-vivo and in-vivo by combining Adeno associated viral approaches and CRISPR- cas9 gene editing reduced scar formation. *(**C** and **D**) In-vivo data with N-cadherin's immunolabeling on transverse cross-sections of harvested scars on AAV6-Cre-GFP (knock out) and AAV6-GFP (control) treated scars, 14-dpi. GFP indicates transduced cells. Dash lines outline the scar edges. **E**. Quantification of N-Cadherin expression in GFP+ cells. **F.** stereomicroscopic images of AAV6- Cre-GFP and AAV6-GFP treated scars at 14-dpi. The yellow dash lines indicate the scar edge. **G.** Quantitative analysis of scar area (Mean ± S.D., n = 8, p = 0.0002, unpaired two-tailed t-test and area . **H.** Masson's trichrome stained vertical (upper panel) and transverse (lower panel) sections from AAV6-Cre-GFP and AAV6-GFP treated scars. The dash lines indicate scar width. **I.** Quantitative analysis of scar width (Mean ± SD, n = 5, p = 0.001, unpaired two-tailed t-test) n=4 animals, 2 wounds per animal. scale bars: C, D, F, H =500µm.*

To further confirm N-cadherin's essential role in collective migration, leading to scarring, we used an independent strategy to locally knockout N-cadherin using CRISPR-Cas9. To do this, we used a constitutively expressing cas9 mice, called full-body cas9. AAV6 viral particles expressing guide RNA targeting murine N-cadherin in exon one or control GFP virus were injected into wounds of full-body Cas9-expressing mice. We did not observe any potential side effects after injecting AAV6 N-Cadherin gRNA GFP or AAV6 GFP control virus. Immunofluorescence analysis showed N-cadherin downregulation

substantially (Fig. 9 A) compared to control animals that received the AAV6-GFP virus. We also observed a reduced scar size in animals, as shown macroscopically and histologically (Fig. 9 B). Quantification from multiple experiments further displayed a reduction in scar width and area to confirm N-Cadherin's role in scar formation (Fig. 9 C and D).

A.

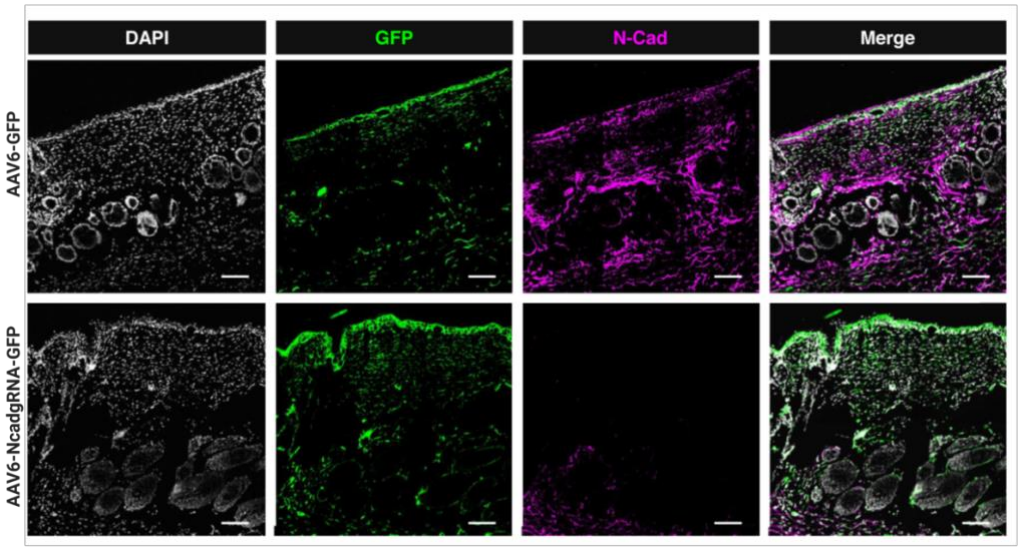

B.

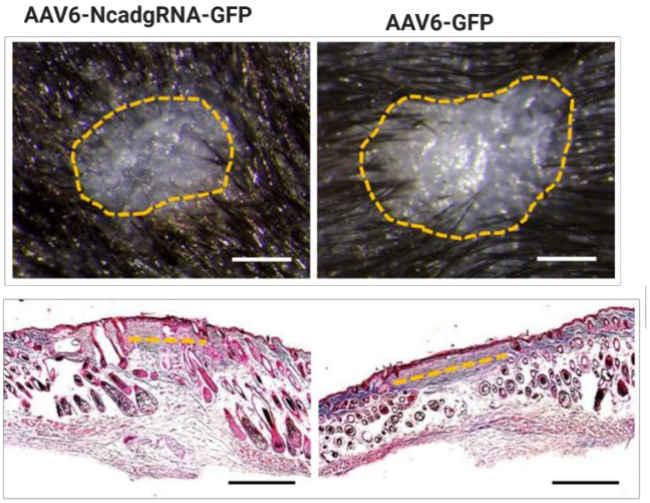

C. **D.**

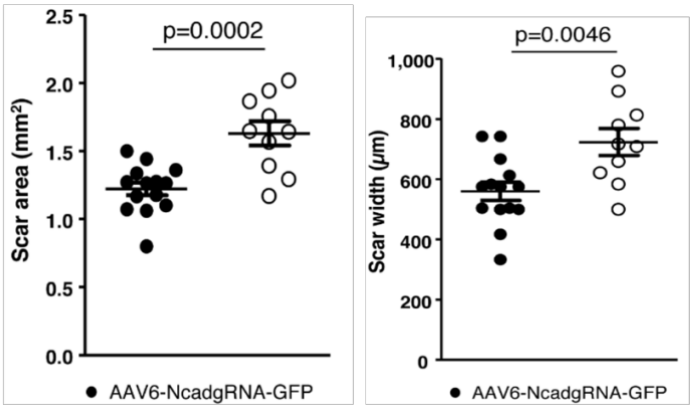

Figure 9: Local knockout of N-cadherin in wounds on full-body Cas9 (R26Cas9) mice by AAV6 viral particle expressing guide RNA specific to mouse N-cadherin (AAV6-NcadgRNA-GFP). ***A***. *AAV6-GFP transduced wounds served as controls. Immunofluorescence images of scars transduced with AAV6-GFP control virus (upper panel) or with AAV6-NcadgRNA GFP virus (lower panel), harvested 14-dpi.* ***B.*** *Representative stereomicroscopic images of AAV6-Ncad-gRNA-GFP and AAV6-GFP treated scars at 14-dpi. The yellow dotted lines indicate the scar edges. Lower panel shows, Masson's trichrome staining of AAV6-Ncadg-RNA-GFP and AAV6-GFP treated scars. The orange dotted lines indicate scar width.* ***C.*** *Quantitative analysis of scar area. Mean ± SEM, p = 0.0002, unpaired two-tailed t-test.* ***D.*** *Quantitative analysis of scar width. Mean ± SEM, p = 0.0046, unpaired two-tailed t-test. n=6 animals for gRNA treatment, n=5 animals for control. 2 wounds per animal. Scale bars: A=100μm; B, C=500μm.*

4. Discussion

Several ex-vivo skin models have been developed to study human wound healing (Table 1). A reliable skin model, which recapitulates human wound repair features, is essential for the clinical and mechanical investigation of human cutaneous wound healing. Full-thickness skin ex-vivo models have been used in wound healing studies. However, most of these models focus on keratinocyte growth, migration, proliferation, and re-epithelialization (Moll I et al., 1998, Forsber S and Rollman O 2010, Stoll SW et al., 2003, Lu H and Rollman O 2004, Mazzalupo S et al., 2002, Frade MA et al., 2015, Peramo A and Marcela CL 2013). All of these models and existing exvivo models summarized in table 1, focus on wound healing and do not go deeper into studying mecanisms of to scar development. Here, we developed two independent ex-vivo models for recapitulating processes from wound healing to scar formation. The hanging drop method that gave rise to "Dermastilla" was not characterized for scar development processes and hence not pursued in further studies. The resultant organoid "Dermastilla" did not perform on par with the SCAD model in maintaining dermal tissue architecture and cellular interactions. The tissue explant model termed SCAD "SCar-in-A-Dish" maintained dermal tissue composition and architecture that a native skin would possess.

Most of the existing wound healing models (see table 1) currently lack transfectability. Work by Syed F et al., 2013 and Ng K.W. et al., 2010 involved transfection with siRNA and microneedle based DNA delivery into human skin, respectively. Fewer studies report electroporation for gene delivery into the skin (Gothelf A and Gehl J 2012, and 2014, Amanthe DH et al., 2015, Broderick KE et al., 2012). Our efforts on electroporation did not show good transfection efficiency, and the viability of the tissue was compromised. However, on the other hand, SCAD was amenable for Adeno associated virus-mediated gene delivery and was successfully transduced. We were also able to modify and alter the function of the target gene at a desired location. We combined the AAV transduction and CRISPR Cas 9 based gene knockdown strategy, that no other model offers at the moment. Based on the ex-vivo and in-vivo findings, we show that N-Cadherin expressed on scar-forming fibroblasts is crucial for scar formation and efficiently knocking down its expression reduced scar width and area.

Existing models are mostly full-thickness skin samples derived from abdominoplasty or breast reduction procedures where the sample can be limited to carry out high throughput studies. SCAD model offers advantages and is amenable for high throughput screening of small molecules, antibodies, target identification, and validation studies. SCAD assays will be invaluable for screening and testing drugs. Using our innovative ex-vivo model for scarring, a drug discovery pipeline will deepen the investigation of interactions where scarring could be inhibited directly on the mouse or human skin.

The SCAD model also proved advantageous that enabled live imaging from mice with genetically traceable cell lineages. En1+ fibroblasts (EPFs) are the scar-forming cell types; along with them are many different cell types in the skin contributing from wound healing to scar formation. The current model explains wound healing in mammals through cross-talk between fibroblasts and the wound granulation tissue. This model shows that fibroblasts contract wounds via their differentiation into myofibroblasts within the granulation tissue that is formed. Granulation tissue from myofibroblasts pulls the matrix fibers internally to provide a contractile force that facilitates wound healing (Gabbiani et al., 1971, Hinz B et al., 2012). Our analysis also shows that scarring cells are not locally transformed into scar-prone cells but rather belong to a pre-committed cell lineage (En1 lineage). These cells are selectively relocated into the formative scar by swarming behaviors (Jiang et al., 2020). Further, our analysis shows that fibroblasts transform into contractile cells by increasing their intracellular contacts via N-Cadherin, and not by their association with granulation tissue, as was previously proposed (Rinkevich Y et al., 2015).

Our findings also carry potential clinical significance. Strategies that inhibit the collective migration of fibroblasts, such as with the N-cadherin knockdown using CRISPR-Cas9 or N Cadherin blocking peptide (Jiang D et al., 2020), could lead to new therapeutics for preventing or reducing scar formation and contractures in human skin wounds. Using the SCAD model and other experimental approaches like single-cell transcriptomics, time-lapse imaging, migration behaviors, and functional studies, we uncovered the extent of cellular plasticity of dermal white adipocytes and En1+ fibroblasts response to injury in the next chapter.

5. List of publications

Findings from this study have been employed in multiple projects and have been published or due for submission. Below is the list of publications and their current status.

1. Jiang D et al., 2020: Injury triggers fascia fibroblast collective cell migration to drive scar formation through N-cadherin. Jiang D, Christ S, Correa-Gallegos D, Ramesh P, **Kalgudde Gopal S**, Wannemacher J, Mayr CH, Lupperger V, Yu Q, Ye H, Mück-Häusl M, Rajendran V, Wan L, Liu J, Mirastschijski U, Volz T, Marr C, Schiller HB, Rinkevich Y. **Nat Commun.** 2020 Nov 6;11(1):5653. PMID: 33159076.

   Remarks: (Fig. 7, 8, and 9 have been adapted from the manuscript published by Jiang D et al., 2020).

2. Correa-Gallegos D et al., 2019: Patch repair of deep wounds by mobilized fascia. Donovan Correa-Gallegos, Dongsheng Jiang, Simon Christ, Pushkar Ramesh, Haifeng Ye, Juliane Wannemacher, **Shruthi Kalgudde Gopal,** Qing Yu, Michaela Aichler, Axel Walch, Ursula Mirastschijski, Thomas Volz & Yuval Rinkevich **Nature** (volume 576, pages 287–292(2019).

3. Rajendran V, Ramesh P, **Kalgudde Gopal S**, Ye H, Rinkevich Y.' Ctnnd1 Knockdown by AAV-delivered CRISPR-Cas9 prevents Scar Formation in Mice. **(Manuscript in preparation)**

4. Qing Yu et al., 2021: "Fibrotic mechanism revealed by chemical screening combined with fascia explant assay." Qing Yu, Pushkar Ramesh, Donovan Correa-Gallegos, Dongsheng Jiang, Simon Christ, Li Wan, **Shruthi Kalgudde Gopal**, Haifeng Ye, Juliane Wannemacher, Kenji Schorpp, Kamyar Hadian, Yuval Rinkevich (**Status: due for submission)**

II Chapter 2 : Fate restricted stromal fibroblasts and adipocytes demonstrate multi-modal responses to tissue injury.

This study is submitted to Nature cell biology under the manuscript ID- NCB-J45105.

Authors: **Shruthi Kalgudde Gopal**[1], Anna Maria Stefanska[1], Dongsheng Jiang[1], Meshal Ansari[1,2], Pushkar Ramesh[1], Johannes Bagnoli[3], Ilias Angledias[1], Donovan Correa Gallegos[1] , Simon Christ[1], Valerio Lupperger[2], Carsten Marr[2], Lindsay C. Davies[4], Wolfgang Enard[3], Herbert B. Schiller[1,5], Yuval Rinkevich[1,5,6]

[1] Helmholtz Zentrum München, Institute of Lung Biology and Disease, Munich, Germany

[2] Helmholtz Zentrum München, Institute of Computational Biology, Munich, Germany

[3] Anthropology and Human Genomics, Department Biology II, Ludwig-Maximilian University München, Germany.

[4] Department of Laboratory Medicine, Division of Biomolecular and Cellular Medicine, Karolinska Institute, Stockholm

[5] Member of the German Centre for Lung Research (DZL)

[6] Helmholtz Zentrum München, Institute of Regenerative Biology and Medicine, Munich, Germany

* Correspondence to: herbert.schiller@helmholtz-muenchen.de (H.B.S.) & yuval.rinkevich@helmholtz-muenchen.de (Y.R.)

1. Summary

Adult connective tissues rearrange themselves during injury, disease, and aging. This response is widely considered to involve cross-lineage conversion between two differentiated stromal cell types: fibroblasts and adipocytes. Here, we directly explore the potential plasticity of these cells after injury in the skin. Using genetic tracing, live imaging, and computational tracking of the two cell lineages in mice, we observe that injury induces a transient migratory cell state in adipocytes with vastly distinct cell migration patterns and behaviors from fibroblasts. Furthermore, migratory adipocytes do not contribute to scar formation. They remain non- fibrogenic both in-vitro, ex-vivo, and upon transplantation into wounds in animals. Using single-cell transcriptomics, we confirm that adipocyte and fibroblast lineages undergo separate differentiation pathways after injury, avoiding cross-lineage conversion. In summary, we have uncovered a transient migratory cell state in adipocytes that remains lineage-restricted and does not converge, overlap with, or reprogram into a fibrosing phenotype. These findings broadly impact basic and translational strategies in the regenerative medicine field, including clinical interventions for wound repair, diabetes, and fibrotic pathologies.

2. Introduction

Cells undergo a gradual stepwise restrictive specification during embryonic development, acquiring lineage-specific differentiation fates to become specialized adult cell types. This gradual segregation of cellular potential during development is thought to be restrictive and maintained into, and throughout, adulthood (Spickard EA et al., 2018). However, many studies have challenged this notion and called lineage-restriction into question by proposing that fully committed cells can respond to tissue challenges, such as injury, disease, or aging, by acquiring new fates. This phenotypic adaptability is termed plasticity.

The prototypical example of plasticity is the terminally differentiated stromal mesenchymal cell (Merrell AJ et al., 2016). Mesenchyme includes mature adipocytes and fibroblasts, which have been proposed to cross-convert between lineages in response to tissue challenges in the skin and internal organs of both mice and humans (table 2). The impact of lineage interplay between adipocytes and fibroblasts is evident clinically in numerous disorders. In diabetes, complications associated with the disease include chronic wound healing and fibrotic pathologies such as renal disease and diabetic retinopathy (Ban CR et al., 2008).

Lineage interplay between adipocytes and fibroblasts is also evident in fibrotic induction, irrespective of an organ. Loss of dermal adipose tissue and adipogenicity in favor of expanding stromal fibroblasts responsible for ECM deposition are consistent fibrosis features in both mice and men. This is exemplified in skin biopsies from patients with systemic sclerosis (Adigun R et al., 2020). Similar imbalances in the adipocyte: fibroblast stromal environment is seen in obese or diabetic patients undergoing fibro-inflammation in their adipose tissue, where adipocyte numbers decrease in favor of fibroblasts, a transition that is associated with fibrosis and scar formation within the connective tissues (Buras ED et al., 2019, Contreras O et al., 2019).

The relevance of changing cellular ratios and phenotypes of fibroblasts and adipocytes within organ systems extends far beyond diabetes and fibrotic disease. However, increased frailty and deterioration in organ function have been directly linked to changes

in adipose and fibroblast communities with age (Mahmoudi S et al., 2019, Tchkonia T et al., 2010). There is a clear need to delineate further each cell lineage's role in tissue homeostasis and repair.

Three main hypotheses have been proposed as to how cells may transition between lineages: de-differentiation (and re-differentiation), (direct) trans-differentiation, and heterotypic cell fusion (Jopling C et al., 2011). (i) De-differentiation is where a cell loses its lineage-specific differentiation state and reverses into a more immature cellular state, sometimes associated with a multi-lineage differentiation potential, as seen in adult stem/progenitor cells. (ii) Trans-differentiation is the transition from one lineage to another either directly or indirectly, i.e., de-differentiation followed by subsequent re-differentiation. (iii) The third conversion mechanism, heterotopic cell fusion, involves merging two terminally differentiated and functionally distinct cell types. This form of fusion results in forming a hybrid cell with the combined functions of both precursor cells and has been shown to occur in low frequency during injury (Johansson CB et al., 2008).

Most reported observations of interchangeability between fibroblasts and adipocytes had been based on one cell type acquiring markers associated with the other, e.g., fibroblasts expressing Perilipin-1 (Plin1) or adipocytes expressing alpha-smooth muscle actin (Acta2). However, these markers are insufficient to establish the identity categorically (Blasi A et al., 2011, Denu RA et al., 2016). Designating plasticity has equally relied on morphological changes, for example, between round and lipidated adipocytes to flat bipolar fibroblasts. However, the phenotype can also be deceptive, as mature adult adipocytes can shed their lipid content under certain metabolic conditions making them even harder to distinguish from fibroblasts. Such fluidity in the homeostatic properties of adipocytes means that a more in-depth characterization of the molecular and cytostructural changes involved in response to injury is needed to definitively demonstrate cellular plasticity. Cellular identity is not just a construct of markers and morphology. Formal proof of physiological plasticity requires observing a defined mature cell losing its cellular identity and functions and metamorphosing into a distinctly different cellular identity with new 4 functions. Such changes are, in the main, inherently achieved through transcriptional regulation, characterized by the loss of mature differentiation markers (as for de-differentiation), the expression of immature cell markers, and acquisition of a new transcriptional landscape (as for trans-differentiation),

supporting the attainment of these new functional properties (Wagers AJ and Weissman IL. 2004).

Reference	Adipose tissue location	Plasticity feature			Experimental evidence	Claim(s)
		Adipogenicity	Fibrogenicity	Migration/ Morphology (Time lapse imaging)		
Shook et al., 2020	DWAT	yes	no	ns	Trancriptional profile of FACS sorted CD26+ Myofibroblasts displayed aSMA and Extracellular matrix profiles similar to that of AdipoQ traced cells.	Wound associated adipocyte-to-Myofibroblast conversion
Z. Zhang and M. Shao et al., 2019	DWAT	yes	yes	ns	AdipoChaser mTmG lineage tracing showed: 1. Newly generated adipocytes that were Pdgfra+ (Adipocyte precursor marker) and 2. Bleomycin treatment of these mice, later showed a population of newly formed adipocytes that had aSMA+ expression.	1. Adipocyte dedifferentiation; and 2. transdifferentiation into Myofibroblasts
Plikus M et al., 2017	DWAT	yes	yes	ns	Myofibroblast reprogramming by neogenic hair follicles and BMP signalling, led to activation of adipocyte transcription factors. Denovo adipocytes regenerated from 1. Sm22 (Tagln) and 2. Acta2 (αSMA) positive myofibroblasts.	Regeneration of fat from Myofibroblasts
Marangoni et al., 2015	DWAT and ScWAT	yes	yes	na	1. Mice with Bleomycin induced fibrosis had loss of DWAT, loss of adipocyte markers and gain of fibrotic marker gene expression. 2. Human adipose derived progenitor cells induced with TGFβ showed Col1a1 and αSMA expression. 3. Bleomycin induced AdipoP transgenic mice showed co expression of αSMA and Plin1.	Adipocyte-to-myofibroblast tansition(AMT)
Vivek D. Desai et al., 2014	Adipose derived stem cells	yes	yes	in-vitro	In-vitro stimulations with TGFβ or bFGF of adipose derived stem cells showed αSMA and ECM protein expression	Adipocyte-to-fibroblast conversion
Schmidt B A and Horsley V, 2013	DWAT	yes	yes	ns	1. Lipoatrophic fatless mice showed defect in fibroblast recrucitment in to wounds. 2. Inhibition of PPARγ and adipogenesis decreased AP (Adipocyte precursor) number and αSMA+ Myofibroblasts	Dermal adipocytes activate fibroblast production in skin wounds
Antonio Giordano et al., 2014	ScWAT	yes	na	ns	Mammary gland alveolar cells gave rise to pink adipocytes that were originally derived from transdiffrentiation of ScWAT	White -pink plasticity
Christian F. Guerrero-Juarez et al., 2019	DWAT	yes	yes	ns	Bone marrow tranplantation experiments showed. 1. Bone marrow derived Hematopoietic stem cells (HSCs) cells gave rise to Fabp4+ and Retn+ cells (Fabp4 and Retn are Adipocyte markers). 2. Sm22+ cells gave rise to Myofibroblasts with myeloid features	Hematopoetic-to-adipose lineage coversion
Shook et al., 2018	DWAT	yes	yes	ns	Skin wounds had multiple myofibroblast subsets, of which one subset predominantely showed Adipocyte progenitor (AP) profile. 1. APs were CD26 high. 2. CD301b+ macrophages promoted AP proliferation through PDGF-C and IGF)	Adipocyte progenitor (AP) to Myofibroblast conversion

ns- not shown, na- not applicable, DWAT- dermal white adipose tissue, scWAT- subcutaneous adipose tissue, FACS- fluorescence-activated cell sorting (FACS), BMP- bone mophogenic protein, aSMA- alpha smooth muscle actin, Tagln- transgelin, CD- cluster of differentiation, bFGF- basic fibroblast growth factor, Retn- resistin, Fabp4- fatty acid binding protein 4, PPARγ- peroxisome proliferator-activated receptor gamma, PDGF-C- platelet derived growth factor C, IGF-insulin- like growth factor.

Table 2: Status of adipocyte plasticity examined in previous studies

3. Aims of the study

We aimed to validate whether or not mature dermal adipocytes remain lineage-restricted or undergo de-differentiation into a precursor cell type or undergo transdifferentiation to a fibrogenic state in response to injury. Illustration (Fig. 10) and the points below summarizes the research questions.

1. To do a thorough molecular level characterization of dermal adipocytes and fibroblasts that proves or disproves cellular plasticity between the two cell types.
2. Spatially and temporally delineate the behaviors of dermal adipocytes in the ex-vivo 'SCar in A Dish' model in response to injury.
3. To find out the occurrence of any cell fusion events between adipocytes and fibroblasts.
4. Establish a comparative migration dynamics of adipocytes and fibroblasts in response to injury.
5. Validate the role of adipocytes in extracellular matrix deposition during scar development.

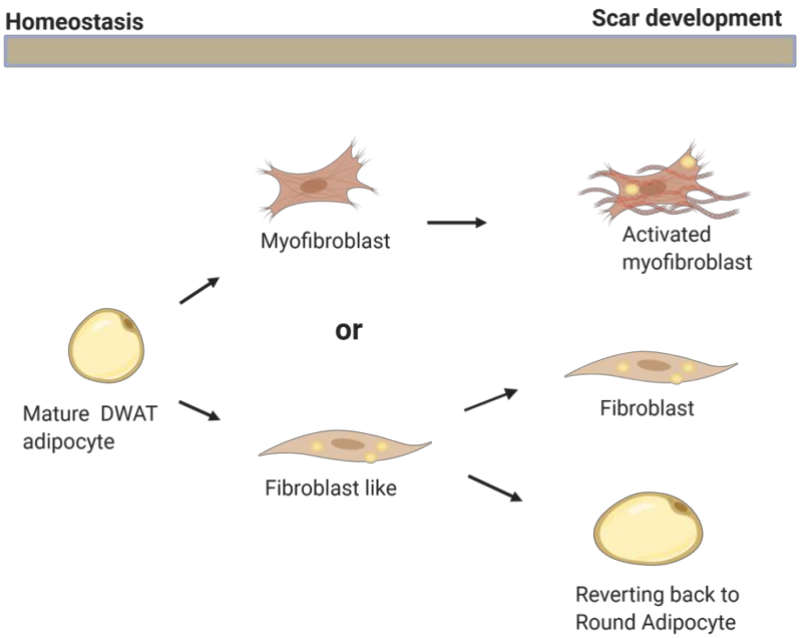

Figure 10. *Cartoon showing the two possible fates of mature adipocytes from homeostasis to scar formation. The research question was to address which of the two conversions of an adipocyte is likely to occur in response to an injury signal.*

4. Results

4.1 Fibroblasts and adipocytes retain their cell lineage identities after injury

To directly address a potential phenotypic convergence of adipocyte and fibroblast lineages, we performed single-cell RNA-seq experiments. To ensure analysis of fully differentiated fibroblasts, we employed a fibroblast-lineage specific reporter ($En1^{Cre}$), labeling a subpopulation of fibroblasts termed EPFs (Engrailed-lineage positive fibroblasts) that we have previously demonstrated to be the fibrogenic cell lineage responsible for scar formation in the back-skin (Correa-Gallegos D et al., 2019, Jiang D et al., 2018, Rinkevich Y et al., 2015). Mature adipocytes were tracked using an adiponectin lineage-specific reporter ($Adipoq^{Cre}$), a hormone involved in regulating glucose levels and fatty acid breakdown, and an essential biomolecule for anti-diabetic clinical interventions (Straub LG and Scherer PE, 2019). The two lineage-specific transgenic lines were individually crossed to a double-color fluorescent reporter ($R26^{mTmG}$), thereby marking mature adipocytes and fibrogenic cells with membrane-bound green fluorescent protein (GFP) in two separate transgenic reporter mice. Skin explants were harvested from both adipocyte ($Adipoq^{Cre}$; $R26^{mTmG}$) and fibroblast ($En1^{Cre}$; $R26^{mTmG}$) double- transgenic reporter mice, at various stages post-injury, followed by purification of adipocytes and fibroblasts for single-cell RNA-seq (scRNA-seq) (Fig. 10 A) (Bagnoli JW et al., 2018, Parekh S et al., 2018, Dobin A et al., 2012).

A.

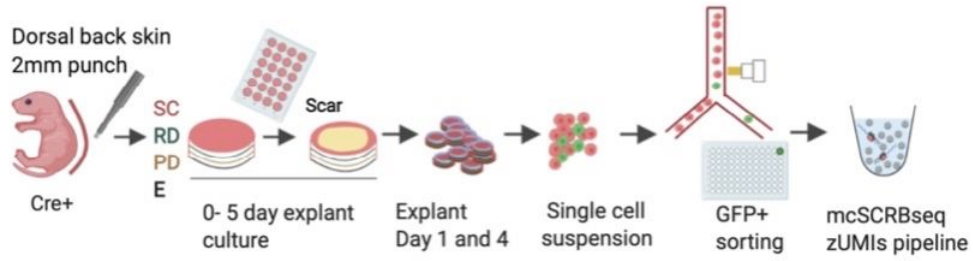

***Figure 11. A**. Schematic of ex-situ explant scar development assay using SCAD and molecular crowding single-cell RNA barcoding and sequencing workflow.*

In two-dimensional uniform manifold approximation and projection (UMAP) embeddings of the single-cell transcriptomes, the two lineages are largely separated but

with partial overlap (Fig. 11 B). The overlap was mainly observed on day 4 after initial wounding (Fig. 11 C). We used Louvain clustering analysis to characterize the heterogeneity of cell states within the two lineage-labeled populations of single cells. After removing one small cluster of cells within the $En1^{Cre}$ labeled lineage, which was clearly not fibroblastic (Fig. 11 D, E), we observed six distinct sub-clusters of cells in each of the $Adipoq^{Cre}$ and the $En1^{Cre}$ lineage (Fig. 11 F, G). All twelve cluster identities have highly distinct marker genes and distinct enriched gene categories (Fig. 11 H).

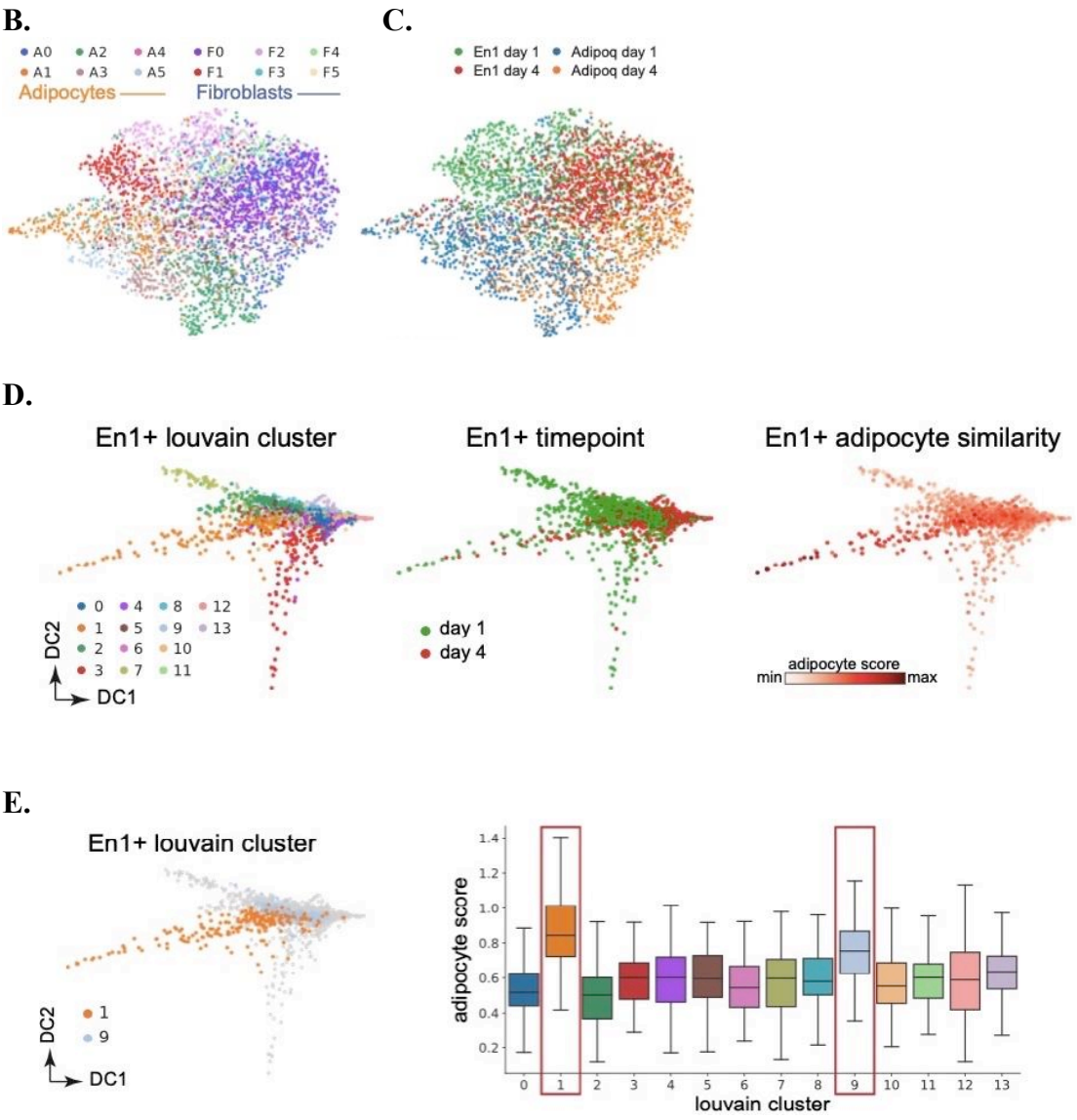

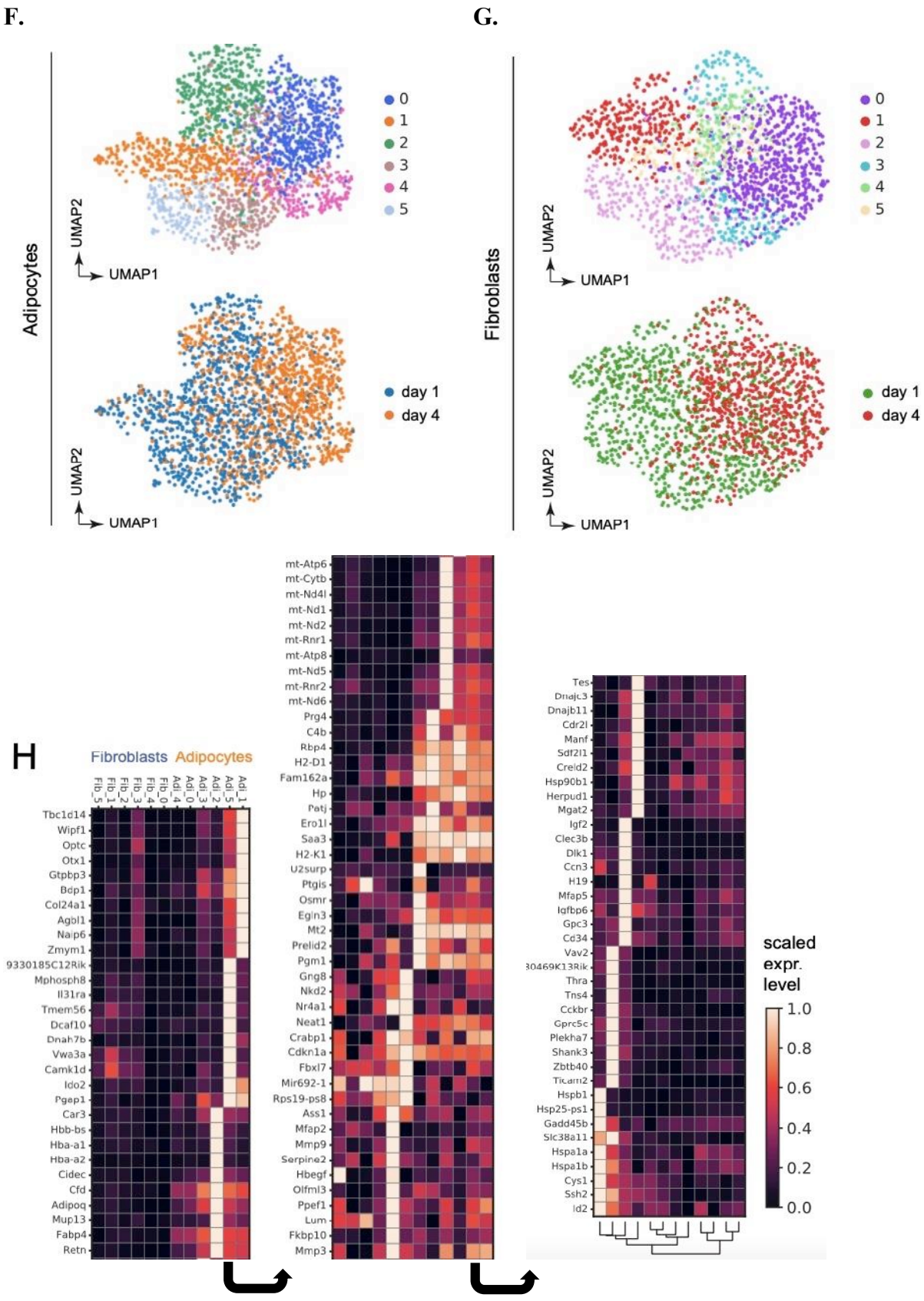

Figure 11. (B-H)

B. *Dimension-reduced single-cell transcriptomic data is visualized through Uniform Manifold Approximation and Projection (UMAP), colored by Louvain cluster and* ***C.*** *time*

point of extraction. ***D and E****. Removal of adipocyte population from whole En1+ populations. Neonatal skin adipocyte gene expression data from Mouse Cell Atlas (MCA)(Han X et al., 2018) was scored against En1+ data set.* ***D****. En1 grouping on day 1 and day 4 of scar explant assay: scoring of an adipocyte gene signature from MCA neonatal skin on En1 data; Louvain clustering was used to identify adipocyte-enriched clusters.* ***E****. En1 Louvain clustering with adipocyte expression on cluster 1 and 9; adjacent is a box plot displaying adipocyte score in a specific cluster.* ***F****. Six distinct sub-clusters of cells in Adipoq^{Cre} lineage across day 1 and day 4.* ***G****. Six distinct sub-clusters of cells in En1^{Cre} lineage across day 1 and day 4.* ***H****. Heatmap showing top 10 marker genes in each of the 12 cell clusters across fibroblast and adipocyte lineages.*

Next, we used Pearson's correlation co-efficiency and measured the magnitude of relationships between the twelve clusters (Fig. 11 I). This analysis indicated that the twelve clusters did not overlap or converge and remained separate. Despite signature variability within lineages, the two lineages stayed distinct and clustered apart under all experimental conditions.

I.

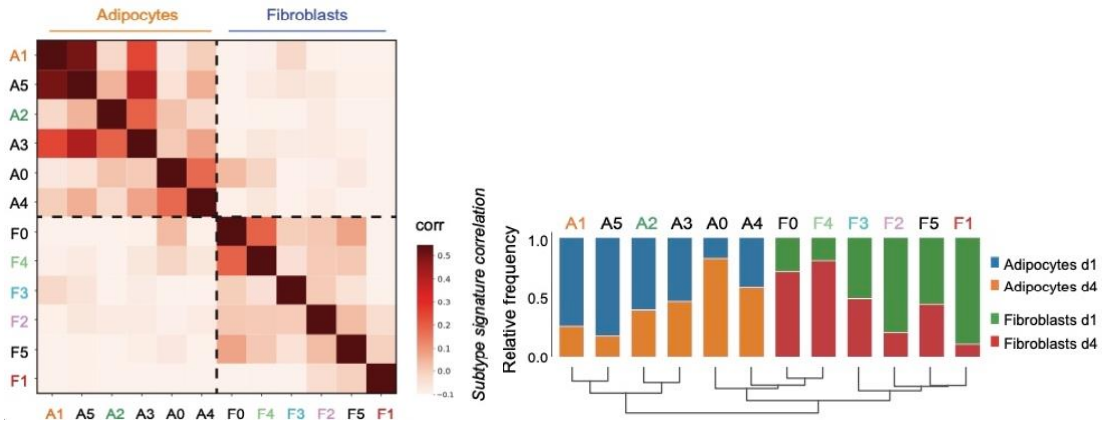

Figure 11. I*. Similarities of marker gene signatures for the 12 cell states (6 states per lineage) along with the relative frequency of each cell state per time point. Color indicates Pearson correlation coefficients for each pairwise comparison across 12 transcriptional cell states in adipocyte and fibroblast lineages.*

These data indicated that adipocyte and fibroblast lineage signatures are not lost in the injury setting. We identified a core set of 88 definitive adipocyte genes and 198 definitive

fibroblast genes that remained specific to both lineages in the injury setting (Fig. 11 J). Gene ontology (GO) gene set enrichment analysis confirmed that the core set of adipocyte genes was significantly enriched for terms such as “fat cell differentiation” and “lipid metabolism” (Fig. 11 K). In contrast, the fibroblast core gene set was significantly enriched for extracellular matrix genes (Fig. 11 L). Further, we compared GO terms of adipocytes enriched for adipogenic processes with fibroblasts and compared GO terms of fibroblasts enriched for fibrogenic processes with adipocytes. As expected, both cell types showed restricted enrichment (Fig, 11 M and N)

The adipocyte core signature contained genes such as Pyruvate dehydrogenase lipoamide kinase isozyme 4 (Pdk4), a gene involved in reactive oxygen species (ROS) production, which has a vital role acting as a second messenger recruiting immune cells, as well as defensive against invading bacteria at the site of injury (auf dem Keller U et al., 2006, Townsend LK et al., 2019). Core adipocyte markers also included Orosomucoid 1 (Orm1), known to be immunomodulatory, Stearoyl CoA desaturase 1 (Scd1), which is involved in fatty acid biogenesis and Serum amyloid A 3 (Saa3), which is responsible for acute phase response and is induced by pro-inflammatory stimuli (Fan Y et al., 2019).

Fibroblast core signature genes included Bone morphogenetic protein 7 (Bmp7), which is likely involved in ECM degradation, Insulin-like growth factor binding protein 5 (Igfbp5) involved in ECM production promoting fibrosis (Nguyen XX et al., 2018), and Nerve growth factor (Ngf), known to promote myofibroblast differentiation (Liu Z et al., 2019, Palazzo E et al., 2012). This indicated that definitive adipogenic and fibrogenic lineage markers are not lost during injury (as assumed in de-differentiation), nor are they re-acquired in alternative lineages (as assumed in trans-differentiation).

To further address this lineage restriction at the pathway level, we scored transcriptomic signatures of both adipocytes and fibroblasts against a selected set of pathway gene lists taken from the RT2 profiler PCR array (n=84). We found that fibroblast signatures were enriched for fibrogenically active pathways like ECM and adhesion molecules, fibrosis, wound healing, focal adhesions, etc. In contrast, adipocytes were enriched for adipogenic pathways such as fatty acid metabolism, Lipoprotein signaling and cholesterol metabolism (Lscm), Peroxisome proliferator-activated receptor gamma (PparɣV) targets,

etc. Furthermore, adipocytes were enriched in defense related antiviral, antibacterial, and anti-fungal pathways (Fig. 11 O).

J.

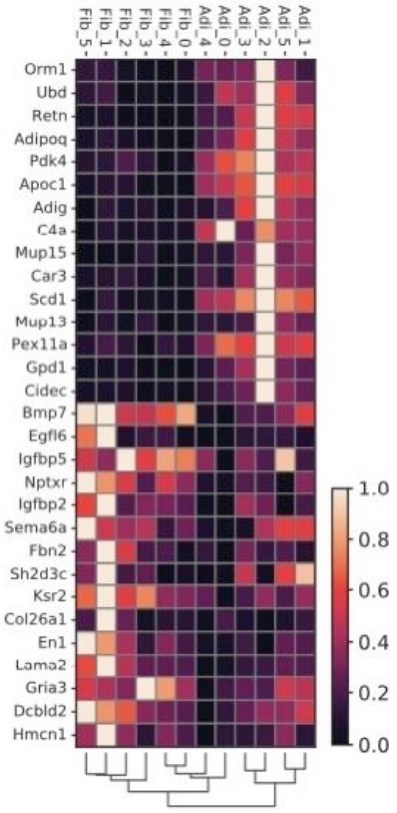

K.

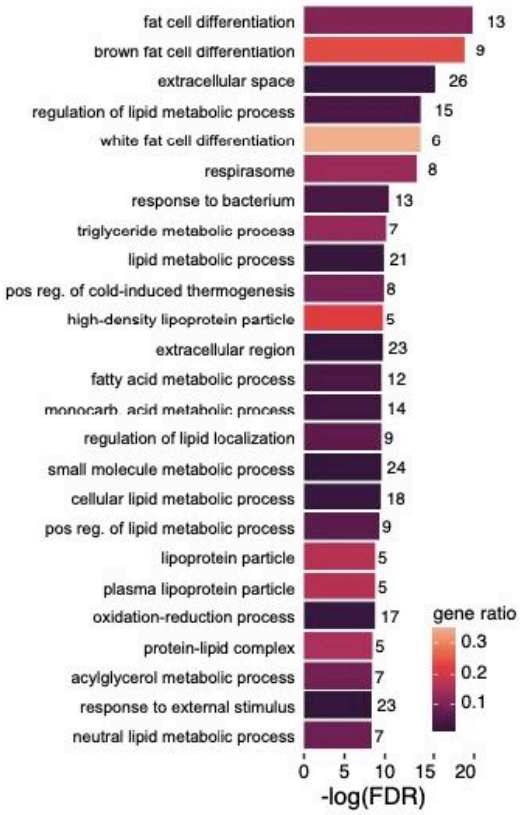

L.

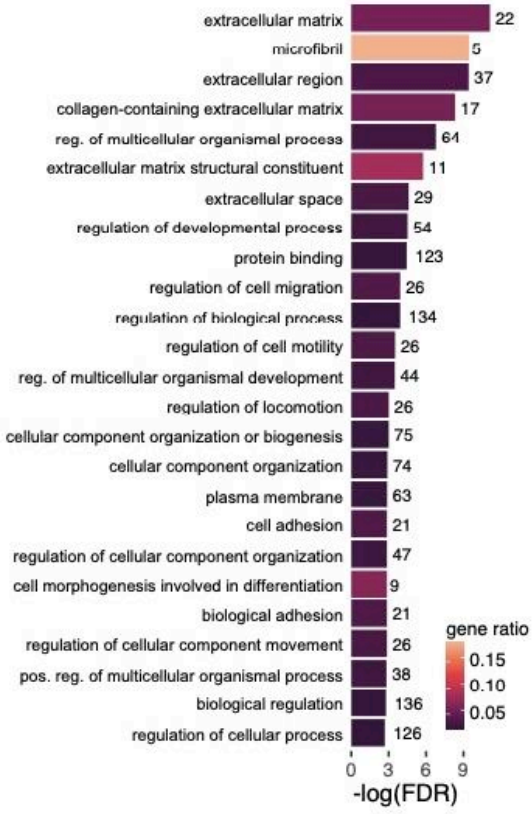

M.

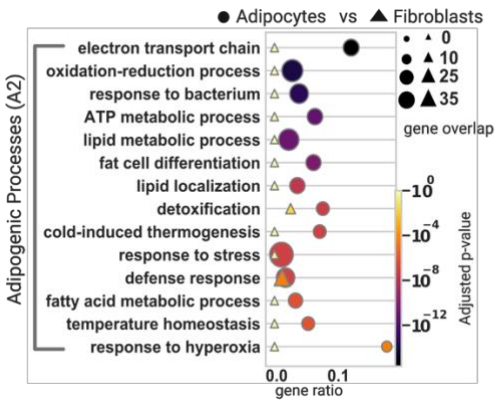

N.

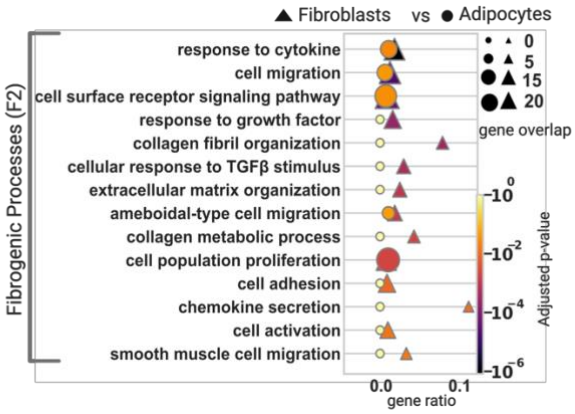

O.

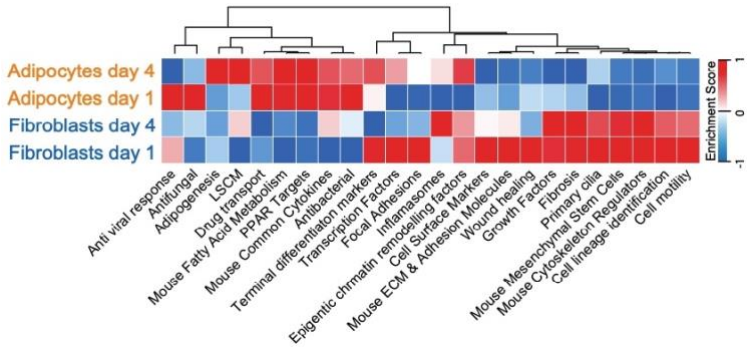

Figure 11. (J-O). ***J****. The heatmap shows the relative expression of the indicated genes across cell states and lineages and core signature genes distinguishing adipocytes from fibroblasts.* ***K****. Gene set enrichment results in an adipocyte core signature gene list (88 genes).* ***L****.Gene set enrichment results in a fibroblast core signature gene list (198 genes).* ***M****. Comparison of gene ontology terms from cluster A2 (enriched for Adipogenic processes) with Fibroblasts.* ***N.*** *Comparison of gene ontology terms from cluster F2 (enriched for Fibrogenic processes) with adipocytes.* ***O.*** *Pathway analysis of adipocytes and fibroblasts on day 1 and day 4.*

Next, we focused on the individually clustering injury-response differentiation trajectories of adipocytes and fibroblasts. Mature adipocytes (cluster A2) were characterized by high metabolic activity and lipid biogenesis, i.e., by expressing the Complement factor d (Cfd), Adiponectin (Adipoq), Perilipin1 (Plin1), and Resistin (Retn) genes (Fig. 11 H). Interestingly, adipocyte cluster A1 was enriched for a gene signature consistent with a migratory phenotype, embellished with active cytoskeletal remodeling, including increased expression of Was/Wasl interacting protein family member 1

(Wipf1), Tripartite motif containing 44 (Trim44), Opticin (Optc), and NLR family apoptosis inhibitory protein 6 (Naip6). It was this adipogenic cluster that appeared transcriptionally closest to fibroblasts (Fig. 11 N). Still, migratory adipocytes (cluster A1) could be consistently distinguished from fibroblast subpopulations based on their expression of adipogenic markers such as Cfd (Fig. 11 P), an adipokine involved in cell signaling and insulin secretion, and Cidec (Fig. 11 Q), a gene encoding cell death activator CIDE-3 and involved in lipid droplet enlargement. Together, these data indicated that mature adipocytes might undergo rearrangement and active remodeling of cytoskeletal actin filaments during injury, reminiscent of a migratory mesenchymal cell, while still retaining the definitive adipogenic-lineage markers and not acquiring the definitive fibrogenic-cell markers.

Analysis of cell states within the fibroblast lineage identified enrichment for several different biological processes (Fig. 11 O). Fibroblast cluster F1 was enriched for cell migration associated genes such as Vav guanine nucleotide exchange factor 2 (Vav2), Slingshot protein phosphatase 2 (Ssh2), Myosin light chain kinase (Mylk), Unc-51 like kinase 4 (Ulk4), IQ motif containing GTPase activating protein 1 (Iqgap1). It was transcriptionally the closest fibroblast cluster to the migratory adipocyte cluster. We identified a state consistent with fibrogenic gene expression (cluster F2), including Collagen type 1 alpha 1 chain (Col1a1), Collagen type 3 alpha 1 chain (Col3a1), Fibronectin (Fn1), Periostin (Postn), Decorin (Dcn), Microfibril associated protein 5 (Mfap5). Cluster F3 demonstrated a genotypic profile central to endoplasmic reticulum (ER) stress processes with the expression of Mesencephalic astrocyte derived neurotrophic factor (Manf), Cysteine-rich with EGF like domains 2 (Creld2), Heat shock protein 90 beta family member 1 (Hsp90b1). Cluster F4 however, was enriched for ECM remodeling genes and processes, expressing Matrix metallopeptidases 9 and 13 (Mmp9, Mmp13), Cathepsin h (Ctsh), Tenascin C (Tnc), Lumican (Lum), Argininosuccinate synthase 1 (Ass1).

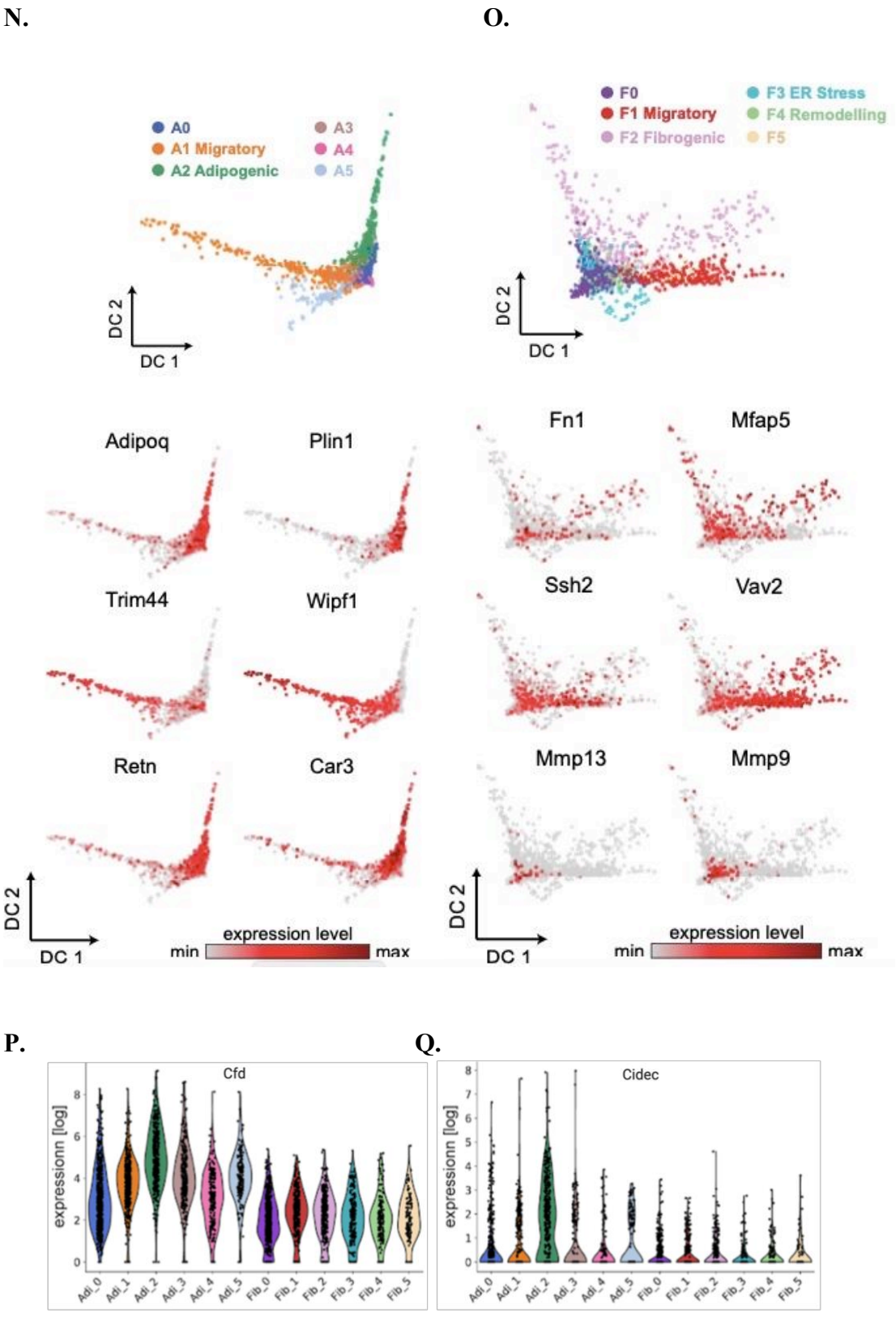

Figure 11. (N-Q). *N. Diffusion maps show adipocyte cell states colored by Louvain cluster assignments and the gene expression levels of the indicated genes.* ***O****. Diffusion maps show fibroblast cell states colored by Louvain cluster assignments and gene*

expression levels of the indicated genes. ***P*** *and* ***Q*** *Expression of mature adipocyte genes Cfd and Cidec with comparable expression in migratory and mature adipocytes, with marginal expression across all fibroblast clusters.*

In conclusion, our data provide compelling evidence that fibroblasts and adipocytes refrain from cross-converting between lineages or de-differentiating in response to skin injury and remain genetically bound to their original fibroblast or adipocyte identity.

4.2 Terminally differentiated adipocytes mobilize and reposition during injury

To study the behavior of mature, terminally differentiated adipocytes and fibroblasts in response to injury, we employed whole-skin explants, allowing visualization and tracking of resident cells, in unprecedented detail over five days post-injury, thereby overcoming restrictions associated with short imaging durations in-vivo (Jiang D et al., 2020). This experiment's principal aim was to evaluate how adipocytes and fibroblasts inherently modulate their activities in response to injury. Ex-vivo models, such as this, allow delineation of the phenotypic and behavioral responses of stromal cells after tissue damage. Briefly, whole-skin explants were isolated from the back-skin of both lineage reporter mouse strains and grown in a specialized incubation chamber that maintains constant O2/CO2, humidity, and temperature. We also modified the incubation chamber with specialized silicone rings to allow multi-photon microscopy objectives to record GFP+ adipocytes and fibroblasts within the skin, in high resolution, without compromising environmental conditions. Using this system, explants remained viable and underwent wound-repair with dermal contraction, scar formation, and re-epithelialization.

With this set-up, directly after wounding, we obtained remarkable videos of clusters of mature, round, lipid-filled adipocyte bundles in both the deep subcutaneous fascia and in the papillary dermis where the bundles wrapped around individual hair follicles (Fig. 12 A, Video S1). Adipocytes remained stationary initially, with the first signs of morphologic change visible at around twenty minutes, including the appearance of small filaments or protrusions extending from the cell membrane (Fig. 12 B, C). At twenty-

four hours, explants had adipocyte clusters that continued the morphologic transformation, with multiple round adipocytes acquiring oval and spindle-shaped morphologies (n=110 cells, n=3 explants). Two days after wounding, 36% of all adipocytes in papillary and fascia deposits gained filopodial extensions (Fig. 12 B) that elongated to >100µm (length of an individual cell). Videos S2 and S3 illustrate two stages of this morphologic change. Video S2 (and Fig. 12 C) shows oval adipocytes extending small membrane filaments with membrane ruffling, indicating active cytoskeletal reorganization seen in motile cells. Video S3 shows a back and forth change of round-to-elongated morphology during movement. Explants on day 2 and day 3 illustrate further filopodia-like extensions, with cells acquiring sleek and slender cell bodies resembling motile cells. Morphologically transformed adipocytes were interspersed with individual adipocytes adopting a fibroblast-like bipolar morphology, stretching to about 50-200µm, whereas rounded adipocytes were much smaller, between 10-30µm. As suggested by our transcriptomics data, adipocytes acquired mobility, moving away from their original fat deposit towards the formative scar region. For example, a single illustrative cell repositioned 380µm away from its original location (Video S4). During their movement, elongated adipocytes underwent active cell division (Fig. 12 C). Furthermore, elongated adipocytes originated from multiple niches, including fat deposits within the papillary dermis surrounding hair follicles and from within the subcutaneous fascia. On day 4, motile adipocytes had reached the center of the scar region but still retained their elongated morphology (Fig. 12 A). Video S5 (and Fig. 12 C) shows an adipocyte acquiring a bipolar elongated morphology with extending filopodia (11.11 hrs), with a gradually protruding cell body (14.23 hrs).

A succession of snap-shot images of whole-skin explants indicated that adipocytes constantly revert back-and-forth between stationary and migratory states, accompanying dynamic remodeling of cellular morphology between rounded and elongated/spindle-shapes (Fig. 12 B, Video S3). Those migrating adipocytes that had relocated on day 5 moved into the center of the wound, where they reverted to their original, lipid-filled, round morphology (Fig. 12 A, Video S6, Fig. 13 A). Quantification of adipocyte morphologies revealed a gradual decrease of rounded cells from day 0 to day 2 and an increase of oval, spindle-shaped and elongated morphologies. A reversal of this phenotype was seen back to a strictly rounded morphology between day 3 and 5 (Fig. 12

B). All forms of adipocytes, including migratory adipocytes, retained Plin1 expression (Fig 12. D).

A.

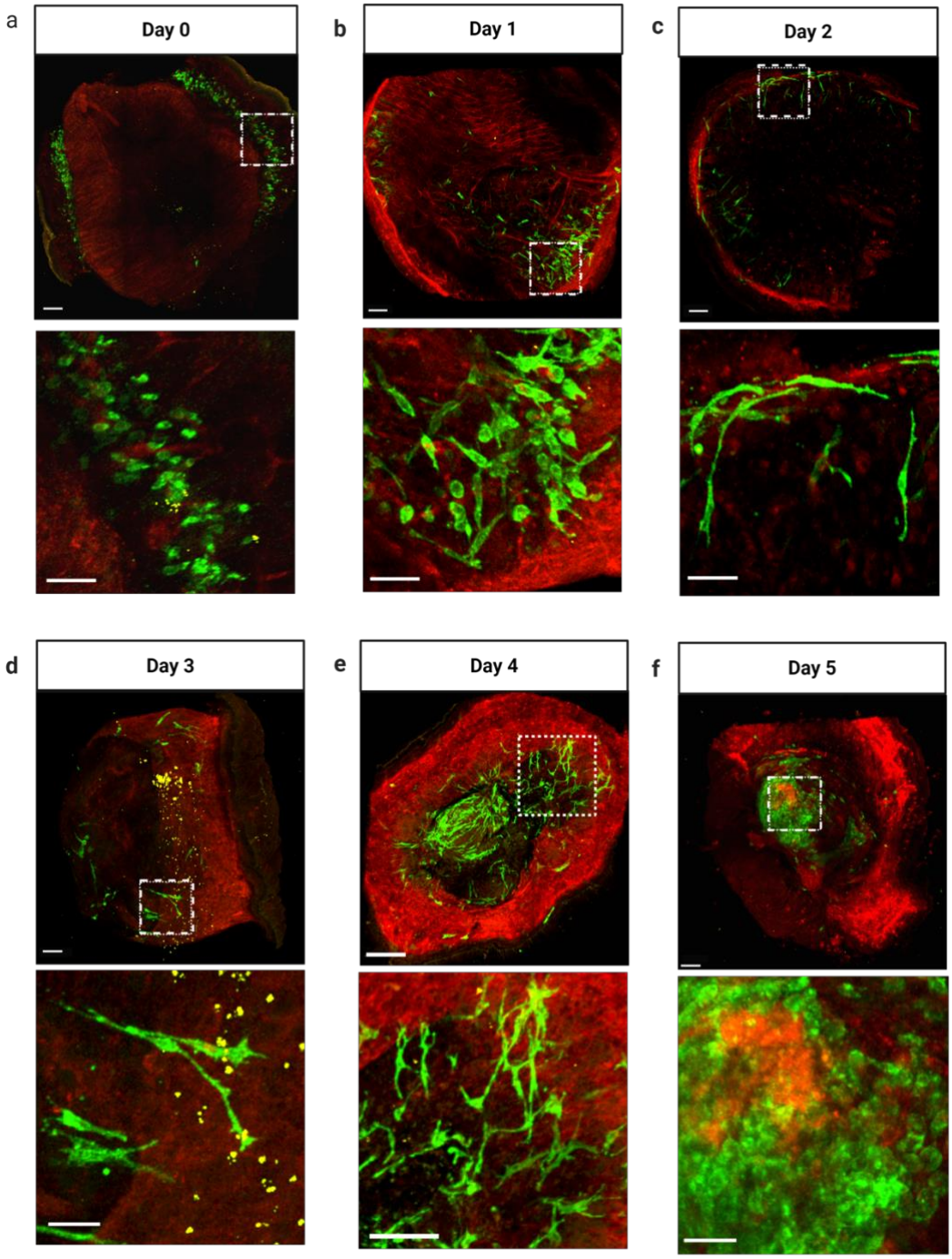

B.

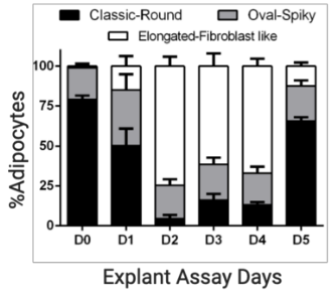

C.

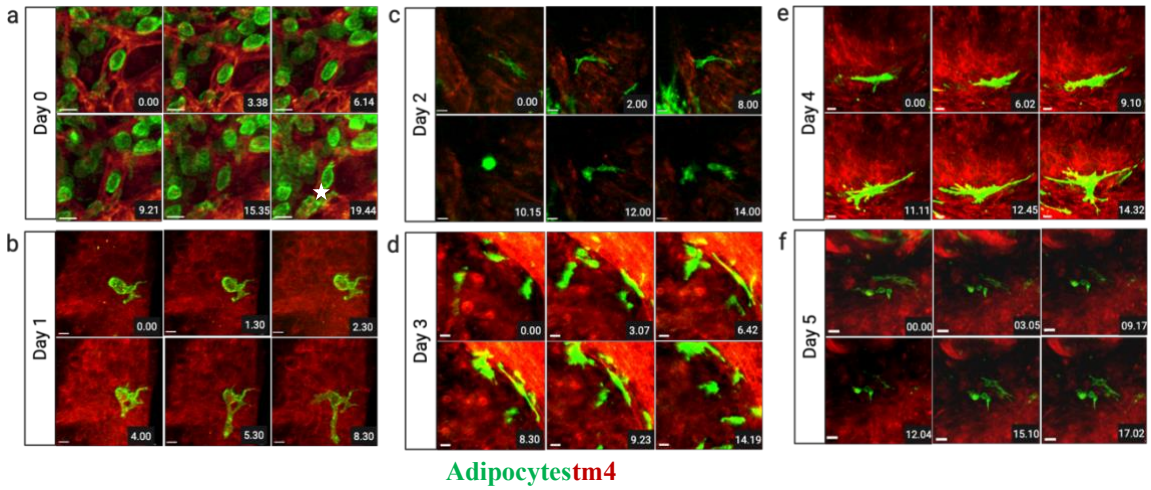

D.

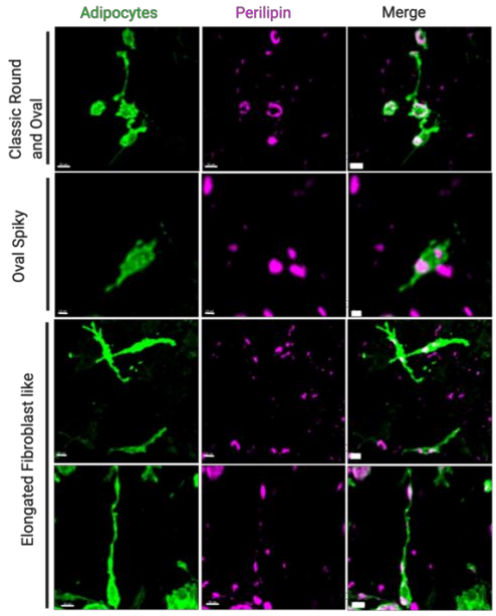

E.

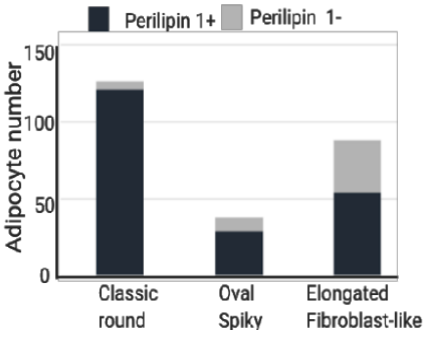

Figure 12. Spatio-temporal characterization of migratory adipocytes.

A. *Changes of adipocytes morphologies in ex-vivo skin explants from day 0 to day 5 at low (upper panel, scale bar:200 µm) and high (lower panel, scale bar:50µm)*

magnification. a. day 0: no movement observed. b. day 1: the appearance of spindles and small protrusions. c. day 2: change of morphology. d. day 3: elongated fibroblast-like morphology. e. day 4: elongated migratory adipocytes in the scar region. f. day 5: adipocytes are reverting to round morphology and migrate on top of scar tissue. ***B****. Quantification of adipocyte morphologies throughout 5- day explant assay, n=3 explants per timepoint.* ***C****. Morphology dynamics of adipocytes. Snapshots of single representative cells from each day (a. to f. are from live explants imaged from day 0 to day 5 respectively) showing the transition from characteristic mature round to migratory states of adipocytes. Time format-hour: min. Scale bar: 20µm.* ***D****. Three migratory morphologies of adipocytes are positive for Perilipin1 by immunolabelling. Scale bar: Classic round 20µm, Oval spliky:10µm, and Elongated fibroblast-like morphologies: upper panel 20µm, lower panel 30µm,* ***E****. Quantification of Perilipin1-positive and -negative cells in explants.*

We looked at three-dimensional whole mount SCAD images and found a block of scar type of tissue that was entirely covered by adipocytes. When we zoomed into the scar region, we found that elongated cells were found to revert back into round cells. (Fig. 13 A). Looking into greater depth and zooming into individual adipocytes in the scad tissue revealed diverse morphologies of adipocytes that resemble fibroblasts (Fig. 13 B). These adipocytes' length was found to vary from 10 to 160μm^2 (Fig. 13 C).

Intracellular accumulation of neutral lipids is often triggered by changes that affect the metabolism of fatty acids and/or neutral lipids such as stress stimuli (Gubern A et ., 2008, Cabodevilla AG et al., 2013, Boren J and Brindle KM 2012, hypoxia (Bensaad K et al., 2014), nitrogen deprivation (Yang ZK et al., 2013). We wanted to see whether EPFs possessed the ability to accumulate lipids. To do this, we took advantage of Lipid tox, a neutral lipid dye, whose uptake can be detected using fluorescence microscopy. Lipid tox has an extremely high affinity for neutral lipid droplets. We stained SCADSs generated from the $En1^{Cre}$ mouse and found that EPFs did not uptake lipids, but in contrast, we saw group of cells mostly likely adipocytes accumulated on top of the SCAD in the scar region (Fig. 13 D).

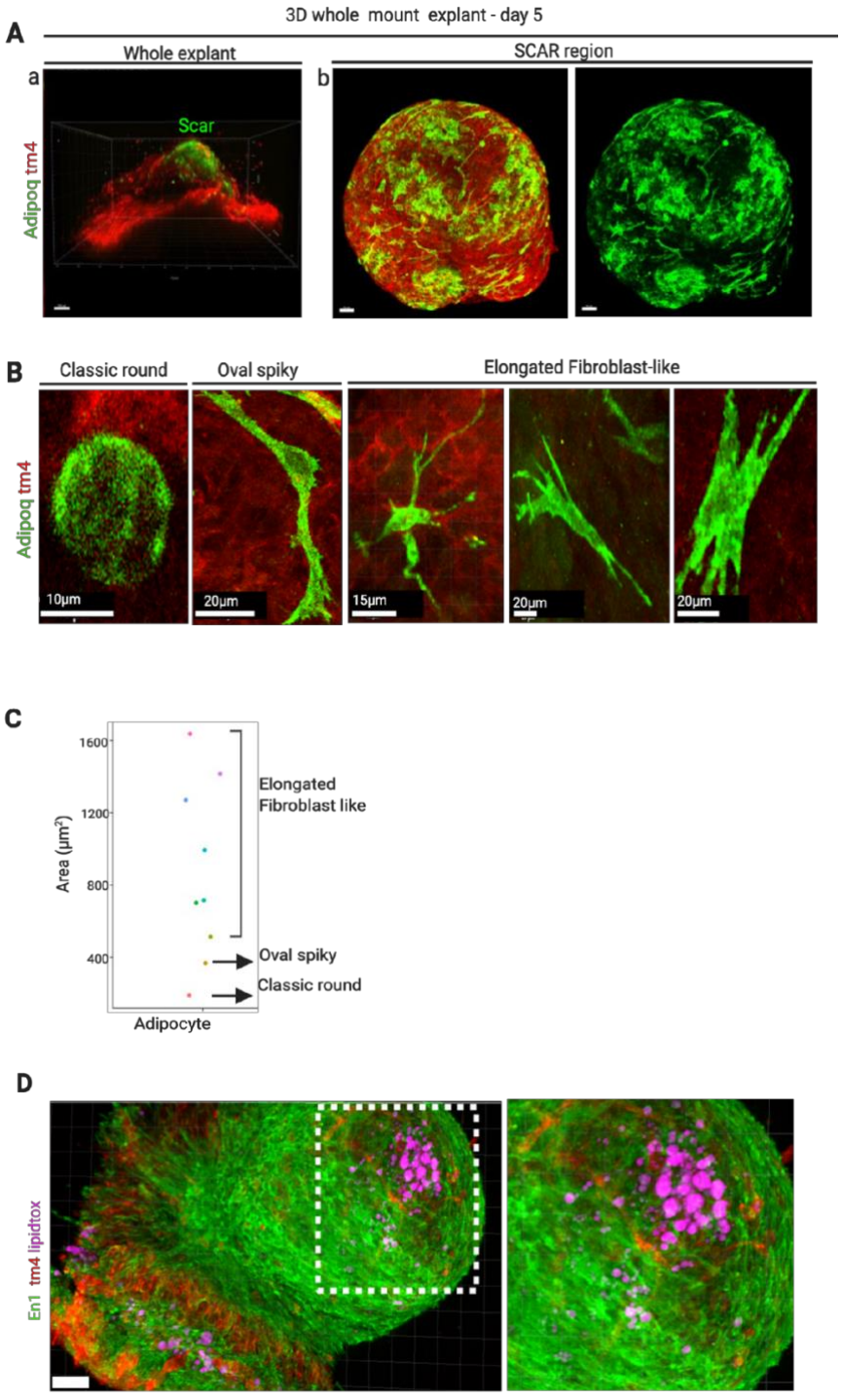

Figure 13: Adipocytes attain diverse morphologies and revert to rounded cells that remain adipogenic during the transition to scar region. A. a. *3D view of whole skin explant showing adipocytes that migrated and formed a scar tissue plug. Scale bar: 100µm.* ***b.*** *Representative images of only the scar region. Merged (left) and Adipoq+GFP+ (right). Scale bar: 50µm.* ***B.*** *Diverse adipocyte morphologies are seen in ex-vivo explant scar assay. Representative examples only shown for each type of*

morphology. ***C****. Size quantification of varying adipocytes morphologies.* ***D.*** *Lipid tox staining showing mature round lipid-filled adipocytes on top of scar tissue in a day 5 explant from a En1^{cre+} neonatal mice. GFP+ fibroblasts appearing in green are negative for lipid tox.*

Next, we investigated if mature adipocytes migrated and repositioned in tissues, in the same way as in the ex-vivo explant model, in in-vivo splinted wounds on the dorsal backs of Adipoq^{Cre}; R26^{mTmG} adult mice. Confocal imaging of wounds on day 7 revealed adipocytes clearly acquire fibroblast-like morphologies and translocate from their initial location within dermal white adipose tissue into the wound bed. On day 21, multiple elongated adipocytes aggregated near the scar region, whereas adjacent non-wounded skin adipocytes retained the classical round morphology associated with dermal white adipose tissue (Fig. 13 E). These findings confirm that transcriptional changes associated with motility and phenotypic shifts are functionally relevant, with adipocytes transitionally switching morphology and actively migrating while retaining adipocyte-committed identity.

E.

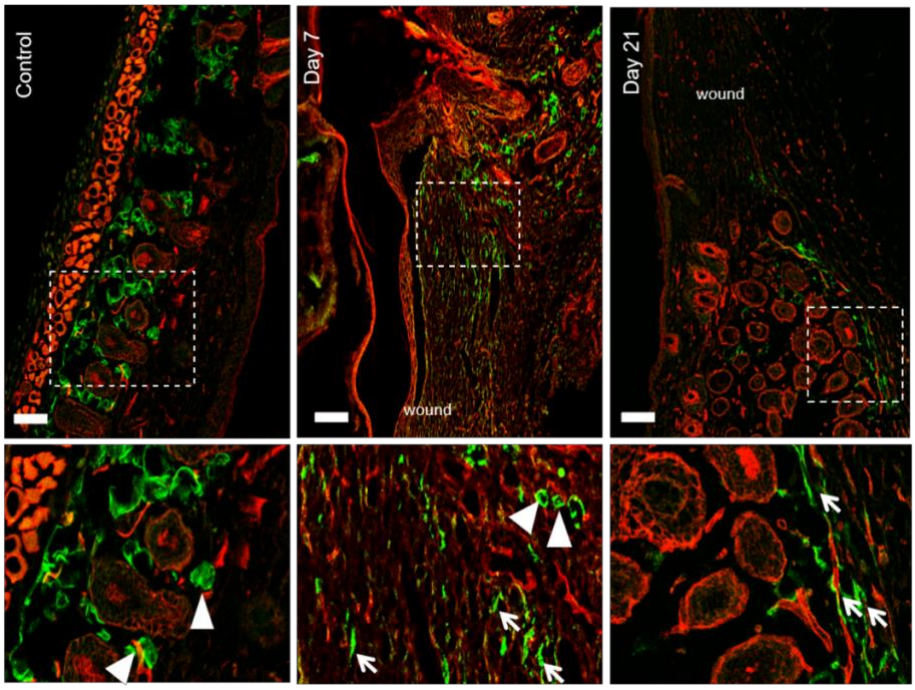

Figure 13. ***E****. Adipocytes superficially resemble fibroblasts after wounding in live mice: Control back skin of adipoqTM4 mice, GFP+ adipocytes are round, located around hair*

follicles. Following the wound healing experiment on day 7, adipoq+ GFP+ cells seen at the wound periphery have a fibroblast-like elongated morphology. On day 21, after injury, activated adipocytes still have a fibroblastic shape as the skin tissue is undergoing remodeling. Arrowheads indicate round adipocytes, and arrows indicate elongated, activated fibroblast-like cells. n=2 mice, 2 splinted wounds per mice. Scale bar: 50µm.

4.3 Absence of cell fusion events between mature adipocytes and fibroblasts

Having found mature adipocytes switching morphology and migrating both in-vitro and in-vivo, we wanted to formally exclude all possibility of lineage crossover. Therefore we examined the possibility of cell fusion between adipocytes and fibroblasts. Cell fusion includes cytoplasmic intermixing, a phenomenon that can be observed and quantified using red and green lineage-specific fluorescence reporters. Cytoplasmic intermixing would be evidenced as co-labeling of green and red (yellow fluorescence) within migratory adipocytes and fibroblasts. To do this, we analyzed and quantified single cells from $Adipoq^{Cre}$; $R26^{mTmG}$ (n=122) and $En1^{Cre}$; $R26^{mTmG}$ lineages (n=135) in both tdTomato+ and GFP+ background at various stages (days) of the explant assay, as well as in-vivo in wounded animals. Lack of co-localization between green and red labels demonstrated that both cell populations, and wound myofibroblasts, shared no history of cell fusion (Fig. 14 A, B). Collectively, our findings prove that during skin injury, adipocytes and fibroblasts remain transcriptionally, behaviorally, and functionally distinct cells, with no inter-conversion or cell fusion between these two stromal lineages.

A.

a.

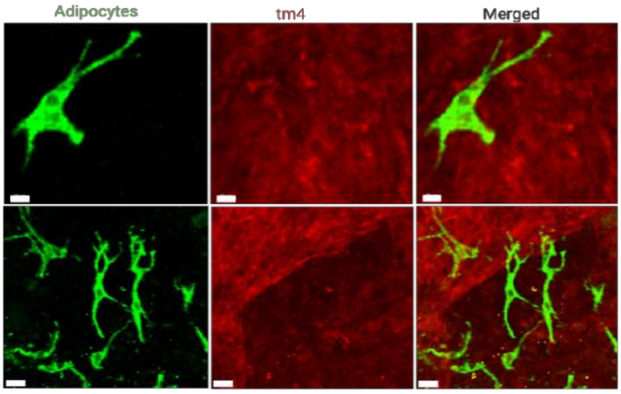

b.

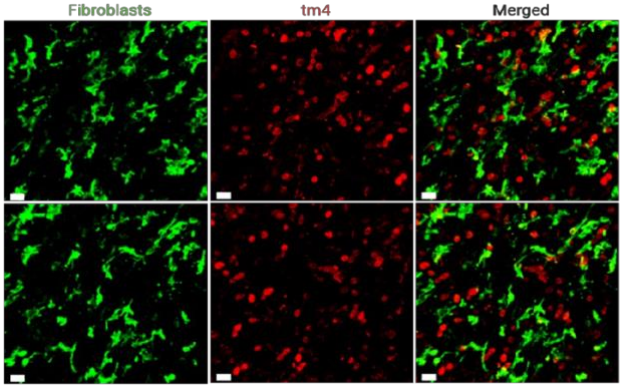

B.

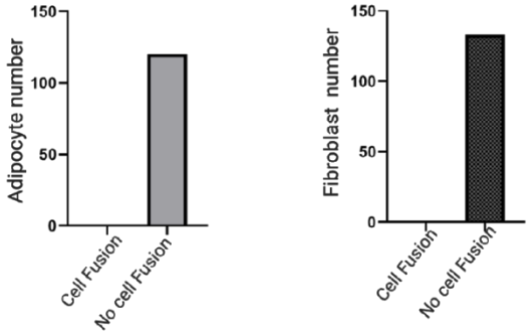

Figure 14: No fusion events detected. A. **a.** *GFP+ adipocytes were analyzed for cell fusion events at single-cell resolution in explants from Adipoq^{Cre}; R26^{mTmG} show no cell fusion with tdTomato+ fibroblasts,* ***b.*** *GFP+ fibroblasts single-cell resolution in explants En1^{Cre}; R26^{mTmG} show no cell fusion with tdTomato+ cells and other lineage negative cells. Scale bar: 50µM.* ***B****. Quantification of cell fusion events in Adipoq^{Cre}; R26^{mTmG} and En1^{Cre}; R26^{mTmG} explants at single-cell resolution. Images were obtained by multi-photon microscopy and processed in Imaris for better resolution. n=3 scads per lineage.*

4.4 Distinct migratory behaviors in adipocytes and fibroblasts

Live imaging data indicated that migratory adipocytes share morphological features with fibroblasts despite there being no cross-lineage plasticity or fusion. To visualize and analyze these distinct motility features and determine whether adipocytes and fibroblasts share migratory behaviors, we crossed both adipocyte and fibroblast mouse lines with a nuclear mCherry reporter ($R26^{LSL\text{-}H2B\text{-}mCherry}$), allowing tracking of individual cellular nuclei across whole skin. Furthermore, this technique allowed us to compare migratory patterns and features such as velocity, distance traveled, directionality, and collectivity between migrating fibroblasts and adipocytes. Back-skin explants were harvested from $Adipoq^{Cre}$; $R26^{LSL\text{-}H2B\text{-}mCherry}$ and $En1^{Cre}$; $R26^{LSL\text{-}H2B\text{-}mCherry}$ double-transgenic mice and cell migration videos recorded in 3D.

Adipocytes initiate their migration from their fat deposits within hours of injury (Fig. 15 A, Video S7). On day 1, manual tracking of cells in the scar region revealed that 53% of all evaluated adipocytes move away from their original position. Yet, only 20% directionally moved towards the formative scar region (defined by a minimal movement of 5μm) on day 1 (Fig. 15 B, C). Fibroblasts, by comparison, responded to damage signals by rapidly relocating to the wound. On day 1 of wound repair, around 70% of fibroblasts had moved towards the formative scar region, with only 22% of the fibrogenic cell lineage moving in other directions (Fig. 15 A, B, and Video S8). On day 4, both adipocytes and fibroblasts remained motile but with widely different patterns of migration. Adipocyte migration was stochastic at a population level, with individual cells generating migration tracks that were non-coordinated (Fig. 15 D, and Video S9). In contrast, groups of hundreds of fibroblasts migrated collectively towards the formative scar region in a uniform and coordinated manner (Fig. 15 D, Video S10). This indicates that most of the fibrogenic lineage cells respond by directional cell movement and migrating into wounds, whereas adipocytes appear to respond and migrate less purposefully after injury.

A.

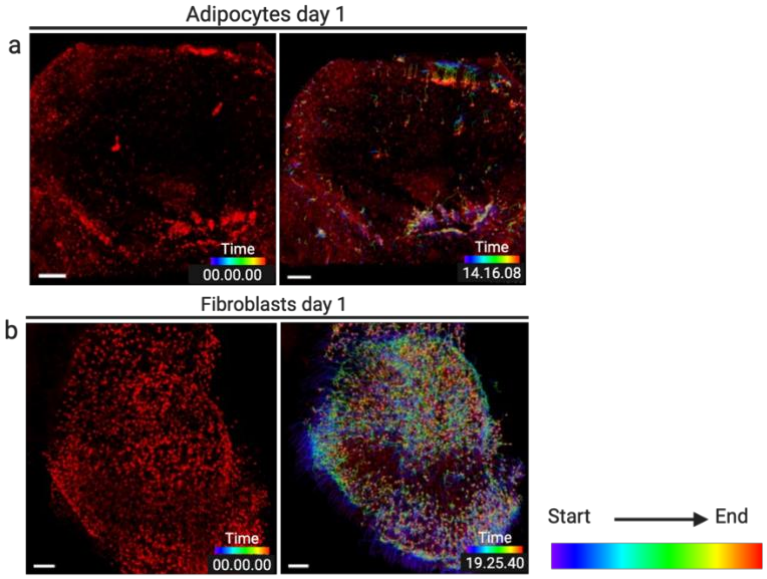
Adipocytes day 1
a
Time
00.00.00
Time
14.16.08
Fibroblasts day 1
b
Time
00.00.00
Time
19.25.40
Start
End

B.

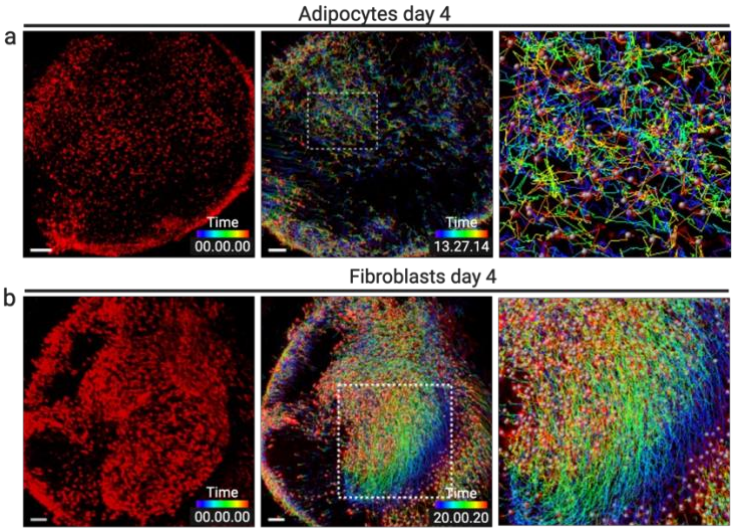
Adipocytes day 4
a
Time
00.00.00
Time
13.27.14
Fibroblasts day 4
b
Time
00.00.00
Time
20.00.20

C.

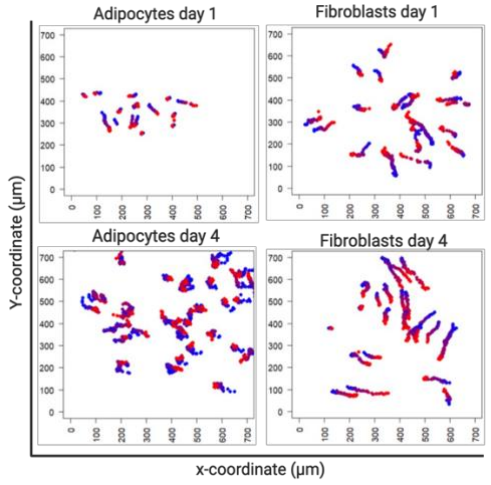
Adipocytes day 1
Fibroblasts day 1
Adipocytes day 4
Fibroblasts day 4
Y-coordinate (µm)
x-coordinate (µm)

D.

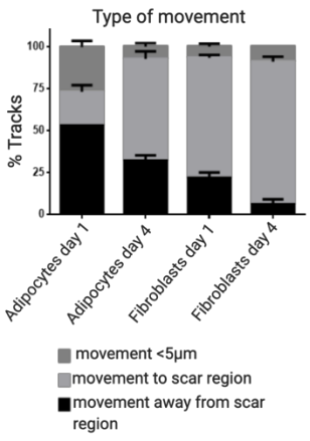
Type of movement
% Tracks
Adipocytes day 1
Adipocytes day 4
Fibroblasts day 1
Fibroblasts day 4
movement <5µm
movement to scar region
movement away from scar region

Figure 15: Migration dynamics of adipocytes and fibroblasts: 3D whole mount time-lapse imaging snap-shots of single-cell tracks from skin explants generated from Adipoq^{cre} and En1^{Cre} crossed to R26$^{LSL-H2B-mCherry}$ reporter mice. ***A****. Snap-shots of* ***a****. adipocytes and* ***b****. fibroblasts migration tracks on day 1,* ***B****.* ***a****. adipocytes, and* ***b****. fibroblasts tracks on day 4, generated by automated cell tracking using Imaris version 9.2.1 (Bitplane).* ***C.*** *Manual tracks of adipocytes and fibroblasts in the scar region of explant at day 1 and day 4. The plot shows the difference in migration distance and type of movement in the scar region of both adipocytes fibroblasts. n=2 videos per time point. Scar region cropped (700µm X 700µm) from whole explant and cells manually tracked. Blue indicates starting, and red indicates ending timepoint.* ***D****. 3 main types of movement quantified using manual single-cell tracks present in* ***C****. Scale bar:A and B =100µm.*

Migration dynamics were further quantified using automated cell tracking in the whole explant. On day 1, adipocytes moved approximately half as fast as fibroblasts and with much more variability throughout all time points, whereas fibroblast velocities remained consistent. By day 4, adipocyte velocities varied from 0.01 to 0.30µm/min, whereas fibroblasts had a consistent velocity of 0.05µm/min (Fig. 15 E, F). Furthermore, movement similarity analysis confirmed that adipocytes move randomly, in contrast to fibroblasts (Fig. 15 G). This suggests that fibroblasts act collectively, whereas adipocytes behave individually. Indeed, directional analysis of adipocytes and fibroblasts further confirmed the collective migration path of fibroblasts, in contrast to adipocytes (Fig. 15 H). These findings indicate that migratory adipocytes and fibroblasts respond in a vastly different manner to tissue wounding in terms of velocity, directionality, and collectivity. It further indicates that collective cell migration is a defining characteristic of migratory fibroblasts, but not adipocytes.

E.

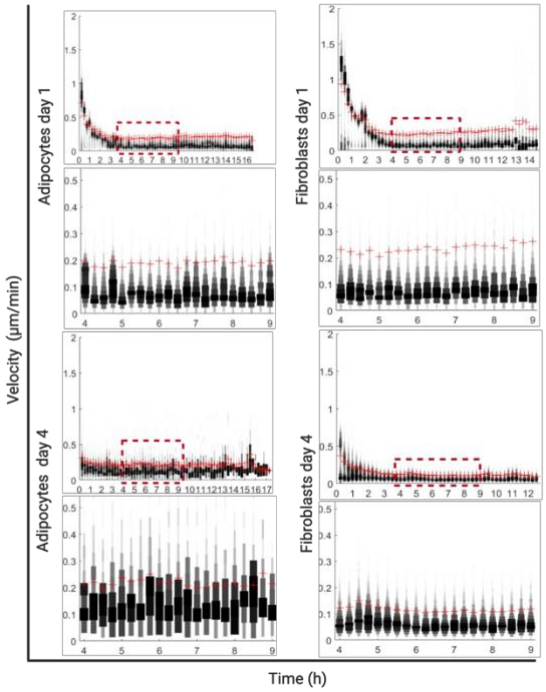

F.

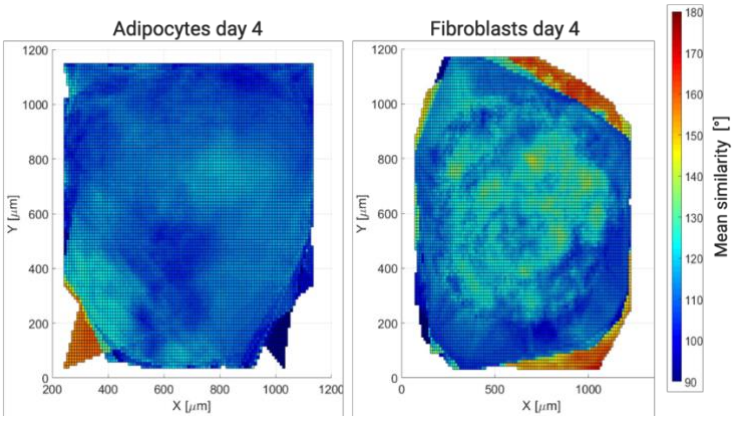

G.

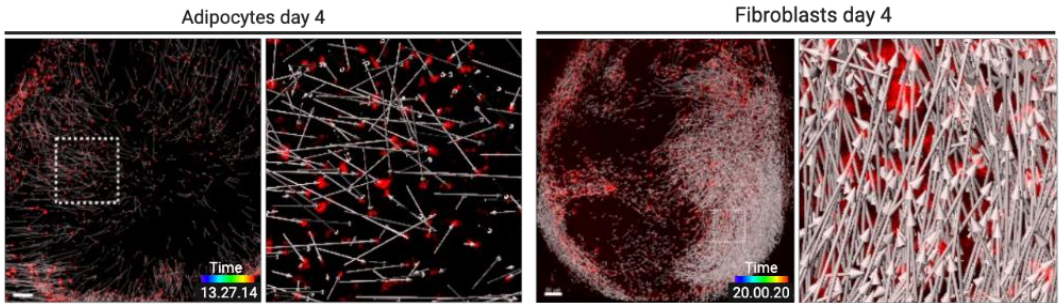

Figure 15. (E to G). E. *Velocity of migrating adipocytes and fibroblasts calculated using time-lapse videos and automated single-cell tracks. Velocity variation and amplitude*

difference from time point 4 -9 hours across all samples are shown in higher magnification (lower panel). ***F.*** *Neighbor similarity analysis of day 4 explants using automated single-cell tracks generated from 3D time-lapse videos. The color bar represents the angles 90° (blue, random movement) to 180° (red, coordinated movement) described as a mean similarity. Fibroblast migrations are coordinated and collective, whereas adipocyte migrations are random and individual.* ***G.*** *Directed and non-directed movement of fibroblasts and adipocytes on day 4. Displacement showed is a representative snap shot area from whole mount SCAD. n= > 1000 cell spots tracked per time point. Scale bar:G=100µm.*

4.5 Adipocytes do not contribute to scar formation

Accretion of extracellular connective tissue matrix is another defining characteristic of fibrogenic cells(Xue M et al., 2015). We previously demonstrated that the fibroblasts that go on to have the ability to form scars (by depositing ECM and accumulating dense fibrous tissue) express the Engrailed gene temporarily during embryogenesis (Rinkevich Y et al., 2015). We thus compared the scar-competent 'Engrailed Past Fibroblasts' (EPFs) with adipocytes for their ability to express and secrete ECM proteins in skin explants; mature adipocytes were colored green with GFP from $Adipoq^{Cre}$; $R26^{mTmG}$ mice, and the scar-forming fibroblasts, EPFs, were colored red with tdTomato.

Expression of the myofibroblast marker αSMA (Gabbiani G et al., 1971, Nagamoto T et al., 2000) was assessed by immunohistochemical localization at day 0 after mimicking wounding through explantation. Here expression patterns correlated with a perivascular niche environment in the absence of established scar tissue. On day 4, parallel fibrils of αSMA were evident within the scar region, and the fibroblasts started to retract from the developing fibrotic tissue. At this time, the adipocytes were distant from the scar developing region, suggesting a less active deposition role. Furthermore, in day 4 explants, the ECM protein Fibronectin was deposited by GFP- tdTomato+ fibroblasts and not by GFP+ adipocytes (Fig. 16 A). Migratory adipocytes did not express fibroblast proteins Fibroblast Specific Protein 1 (FSP1), Transcription Factor 21 (TCF21), or Col3a1 (Fig. 16 C-F). Myofibroblast and fibrogenic markers, such as Ddr2, Lrrc17 (Hao H et al., 2016, Hsia LT et al., 2016), and ECM markers Col1a1 and Col3a1, were upregulated across all fibroblast subsets, but not within adipocytes (Fig. 16 B, F).

A.

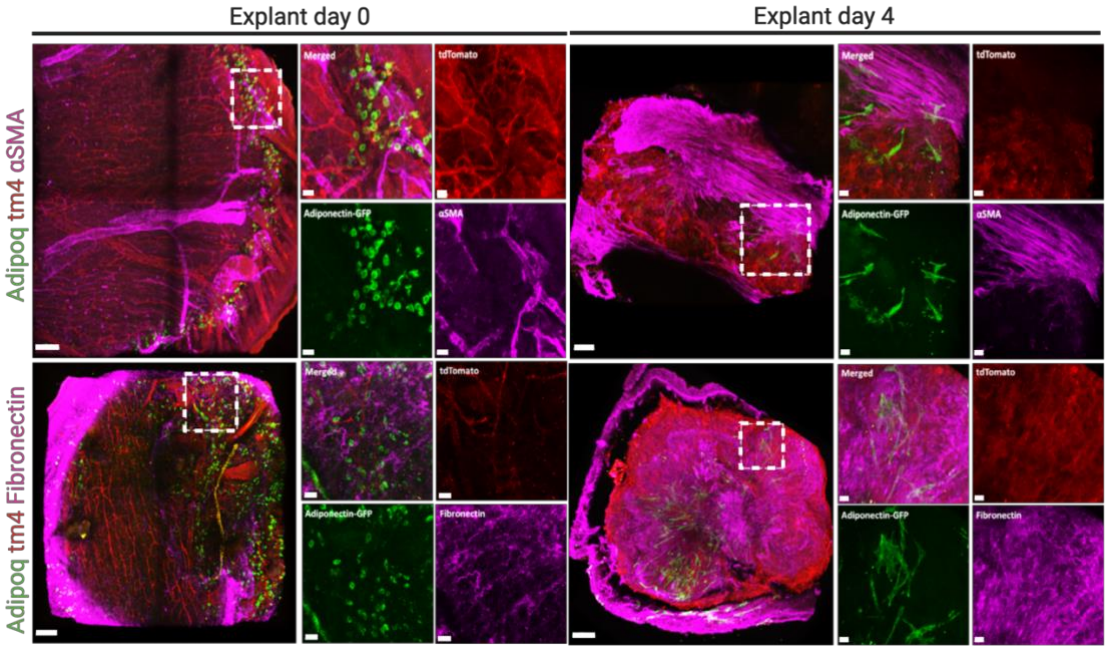
Explant day 0
Explant day 4
Adipoq tm4 αSMA
Adipoq tm4 Fibronectin
Merged
tdTomato
Adiponectin-GFP
αSMA
Fibronectin

B.

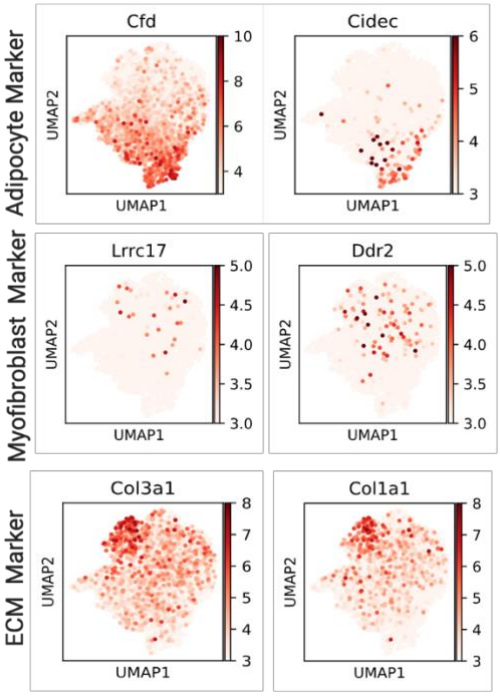
Adipocyte Marker
Myofibroblast Marker
ECM Marker
Cfd
Cidec
Lrrc17
Ddr2
Col3a1
Col1a1
UMAP1
UMAP2

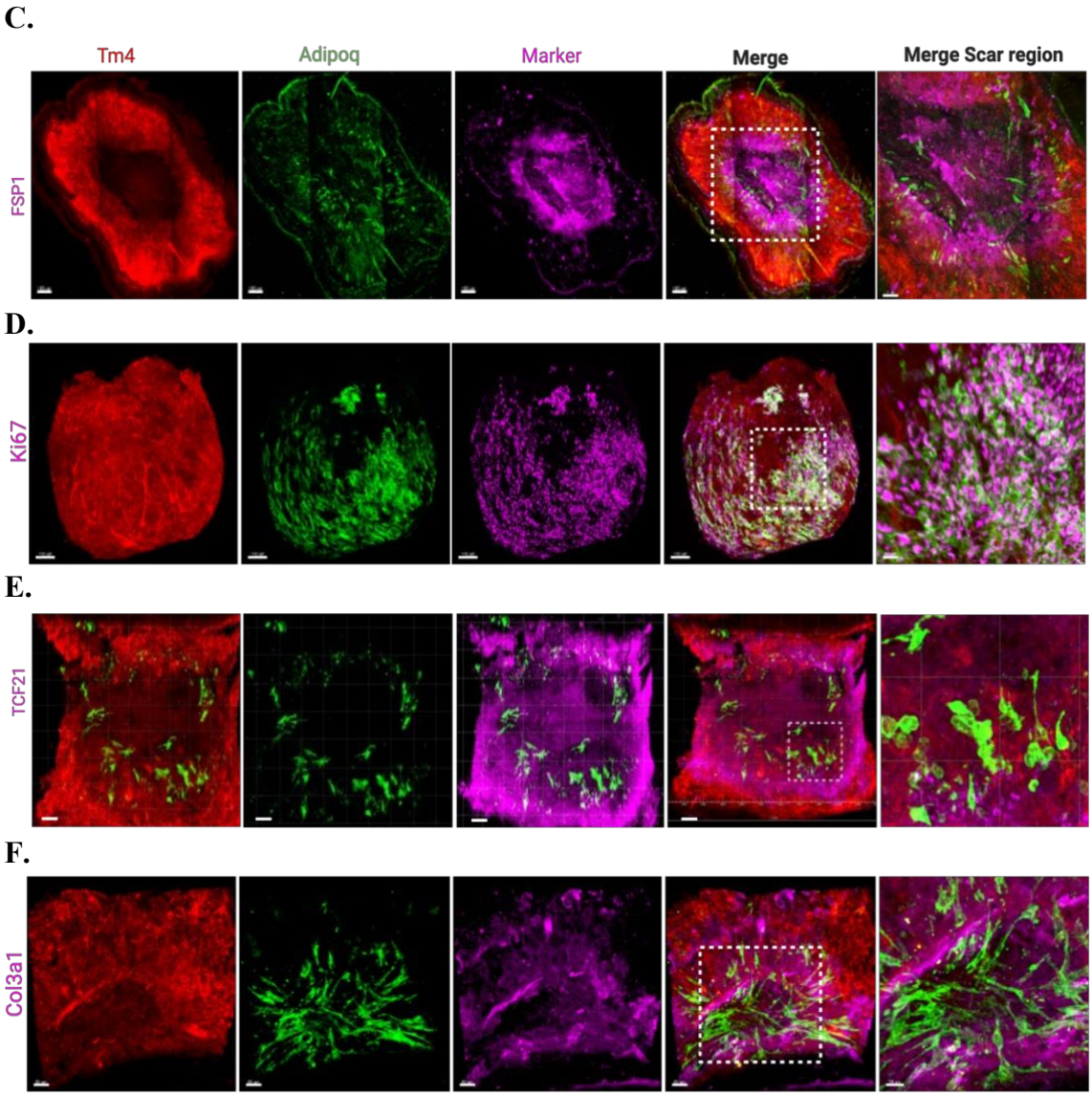

Figure 16: Adipocytes are non-fibrogenic. Ex-vivo dermal Adipoq^{+} cells decrease lipid content but do not convert to myofibroblasts and do not deposit extracellular matrix during scarring. ***A.*** *Immunostainings of Adipoq^{cre+} explants at day 0 and day 4. Adipocytes in Green, tdtomato in Red, and marker in Magenta. Merged channel image of the whole explant (left), magnified area of individual channels (right). Markers- Myofibroblast marker - αSMA (top), and extracellular matrix marker -Fibronectin 1(bottom).* ***B****. Feature plots generated from combined analysis of mcSCRBseq showing adipocyte, myofibroblast, and extracellular matrix specific enrichment in cell type-specific clusters.*

(C-F). *3D Immunostainings were performed on Adipoq^{Cre+} ex-vivo explant tissue on day 4 or day 5. Adipocytes in Green, tdtomato in Red, and marker in Magenta. Merged channel image (right), magnified area of the merged channel (extreme right). Migratory adipocytes* ***C.*** *do not express the fibroblast marker, fibroblast specific protein 1 (FSP1),* ***D****. express Proliferation marker, Ki67,* ***E.*** *and* ***F.*** *do not express the fibroblast markers such as extracellular matrix Col3a1, and lipofibroblast marker TCF21. Scale bar: Whole mount 3D SCAD =100µm, magnified images:20µm,* ***C-F****= 100µm.*

To evaluate directly whether adipocytes produce and deposit ECM proteins, we performed 3D immuno-labeling of deposited ECM proteins (Fig. 17 A). Adipocytes did not secrete Fibronectin or Type-I Collagen, irrespective of their morphology or motility status (Fig. 17 B). As a control, baseline matrix production was compared to that induced by transforming growth factor-beta 1 (TGFβ1) stimulation, a known pro-fibrotic cytokine upregulated during the early stages of the wound healing response (G. C. Blobe et al., 2000). Fibroblasts deposited significant amounts of Fibronectin and Type-I Collagen. In contrast, adipocytes did not deposit these matrix proteins (Fig. 17 B-D). Stimulation with recombinant (rTGFβ1) significantly increased Fibronectin and Type-I Collagen in fibroblast, but not in adipocyte, matrix (Fig. 17 B-D). Interestingly, TGFβ1 altered adipocyte contour to the same fibroblast-like morphology seen in migratory adipocytes in-vitro (Fig. 17 E). Despite their morphologic conversion, we have seen that adipocytes are not fibrogenic, and they do not contribute to the ECM, which is exclusively deposited by fibroblasts.

A.

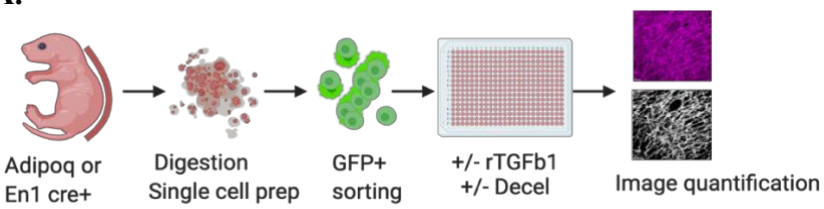

B.

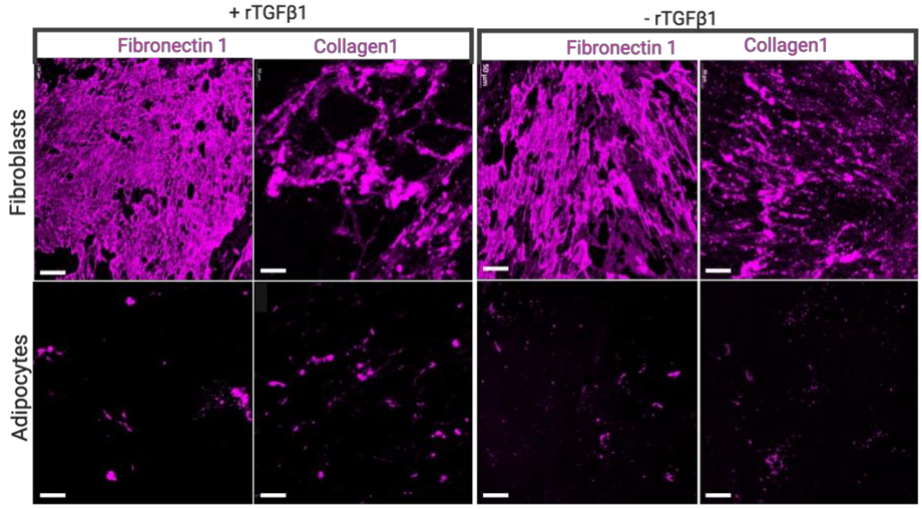
+ rTGFβ1
- rTGFβ1
Fibronectin 1
Collagen1
Fibronectin 1
Collagen1
Fibroblasts
Adipocytes

C.

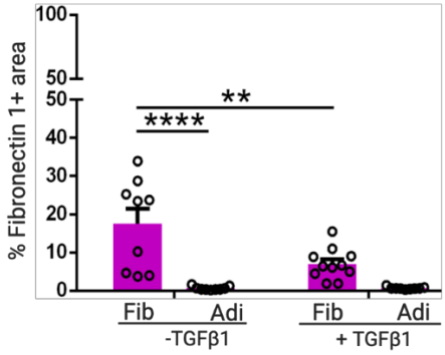
% Fibronectin 1+ area
100
50
50
40
30
20
10
0
**
****
Fib
Adi
Fib
Adi
-TGFβ1
+ TGFβ1

D.

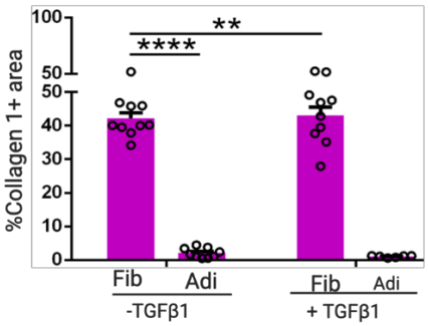
%Collagen 1+ area
100
50
50
40
30
20
10
0
**
****
Fib
Adi
Fib
Adi
-TGFβ1
+ TGFβ1

E.

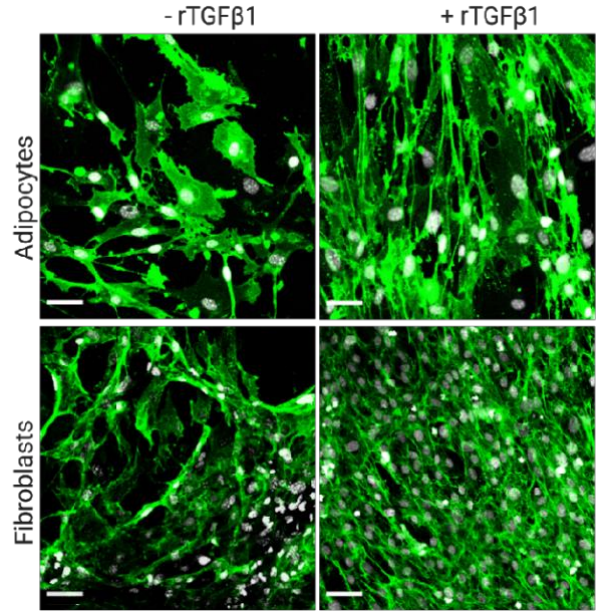
- rTGFβ1
+ rTGFβ1
Adipocytes
Fibroblasts

Figure 17. (A - E) ***Adipocytes deposit much less matrix proteins than fibroblasts under scarring conditions***. ***A***. *Schematic of in-vitro matrix deposition assay and quantification using Image J.* ***B***. *FAC-sorted adipocytes and fibroblasts were cultured in-vitro, with and without rTGFβ1 stimulation for 72hrs. Followed by decellularization and immunolabelling of deposited matrix Collagen 1 and Fibronectin 1.* ***C. and D***. *Quantification of percent fluorescence of deposited matrix showing a higher percentage of the deposited matrix when compared to adipocytes, n=3 biological replicates, n=12 images.* ***E***. *Morphological changes observed in both adipocytes and fibroblasts after rTGFβ1 stimulation. Scale bars: B, E= 50µm*

In-vivo wounds on both day 7 and late day 21 wound stages contained migratory non-lipid filled adipocytes that were SMA negative (Fig. 17 F, G) and therefore separate from fibrogenic cells. To evaluate the relevance of these observations further in-vivo, we transplanted 2.5×10^5 individual cells of each lineage into full-thickness dorsal wounds of immuno-deficient Rag2-/- mice. Wounds were harvested 7 days post-transplantation, and ECM proteins, Fibronectin, and Type-I Collagen were quantified by immunofluorescence within the transplanted regions compared to adjacent non-transplanted areas (Fig. 17 H). Transplanted fibrogenic lineage cells generated ectopic scar ECM architectures, whereas transplanted purified adipocytes had negligible effects on scar formation and connective tissue architecture (Fig. 17 I).

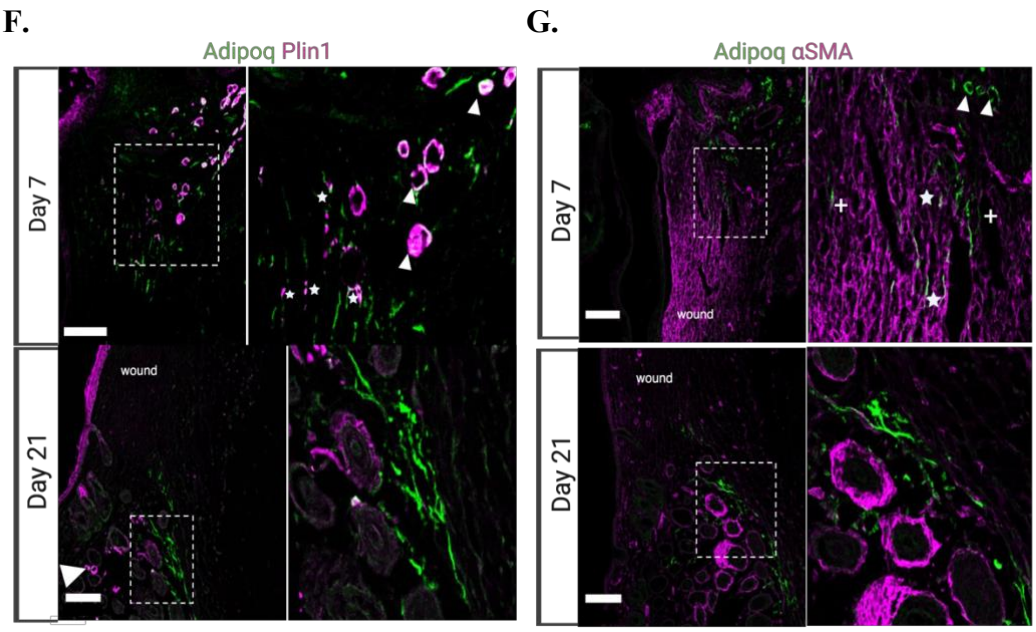

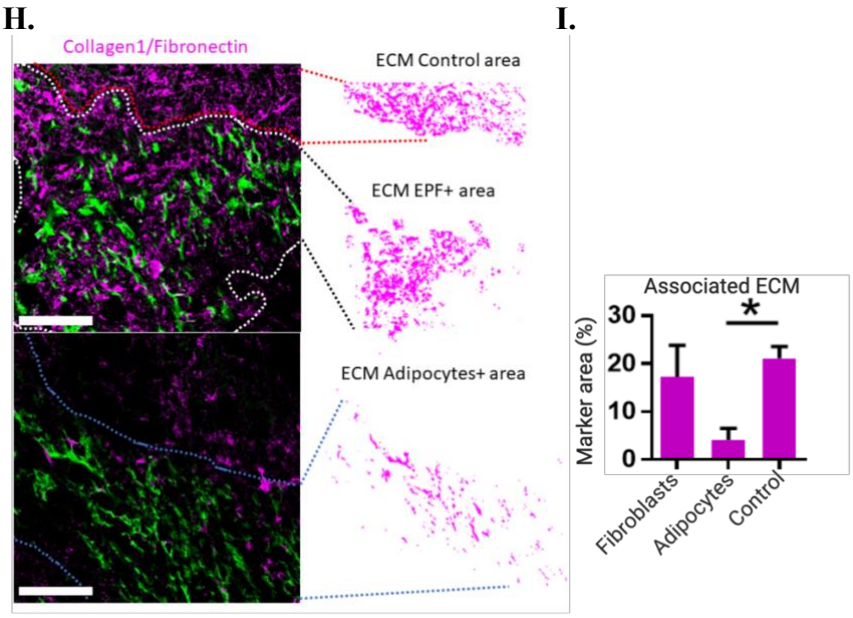

Figure 17. (F- I) F*. Immunolabeling of splinted wounds in mice. Co-staining with anti-perilipin antibody shows activated elongated GFP+ cells (*) and rounded cells (arrowhead) are positive for Perilipin1 on day 7.* ***G****. Co-staining with anti-αSMA antibody shows a mixture of elongated GFP+ cells negative (+) and positive (*) for αSMA. Rounded adipocytes (arrowhead) are negative for myofibroblast marker. Day 7 shows widespread αSMA staining in the center of the wound. In contrast, day 21 shows only physiological αSMA presence in the dermal papilla..* ***H****. Transplantation of FAC-sorted Adipocytes or Fibroblasts cells from P1 newborn mice into adult Rag2$^{-/-}$ immunodeficient mouse back skin following the excisional wound model. Immunolabelling with anti Collagen1 or Fibronectin 1 and quantification of associated extracellular matrix in the transplanted regions.* ***I.*** *Quantification of Adipocyte and fibroblasts associated ECM in the transplanted regions. n=2 mice. Scale bar:* ***F, G****= 200µm,* ***H****=100µm.*

5. Discussion

In this paper, we demonstrate the irreversible nature of adipocyte and fibroblast differentiation. The widespread changes in cellular composition between fibroblasts and adipocytes that occur during skin injury do not involve crossing over of their identities, as had been previously assumed (table 2).

Dramatic behavioral modulations of both adipocyte and fibroblast cell lineages in injured tissues were observed. Still, there was no evidence for adipogenic origins of fibrosing cells during injury or evidence of any cross-lineage conversion or cell fusion between adipocytes and fibroblasts by assessment of transcriptomic, behavioral, or functional criteria. In light of our data presented here, we propose that previous reports exemplifying plasticity between adipocytes and fibroblasts (summarized in table 2) rather involve extreme morphological changes that are associated with the migratory adipocyte cell state we have uncovered here or the use of a select few marker changes such as Plin1 and Acta2. We believe that this migratory and morphologic behavior of adult adipocytes nurtured the hypothesis that adipocytes and fibroblasts cross convert.

Clinical observations indicate widespread cellular composition changes between fibroblasts and adipocytes during injury, disease, obesity, cancer, or even with age (Pellegrinelli V et al., 2016, Seale P et al., 2011, Rosenwald M et al., 2013, Bochet L et al., 2013). For example, Loss of dermal adipose tissue and adipogenicity are consistent fibrosis features in both patients and mice. This is consistently observed in skin biopsy specimens from patients with systemic sclerosis and in sclerodermatous graft-versus-host disease (Marangoni RG et al., 2017, Simonacci F et al., 2017). Fat grafting is another example where soft tissue implantation sometimes results in loss of fat volume that appears histologically as replacement of mature adipocytes with a fibroblast-like infiltrate (Krastev TK et al., 2020, Tabit CJ et al., 2011). Many obese or diabetic patients undergo fibro-inflammation in their fatty tissue, where adipocyte numbers decrease in favor of fibroblasts, a transition that is associated with fibrosis and scar formation within the connective tissues (Pellegrinelli V et al., 2016). This again appears to support the idea of plasticity and interchangeable fates between adipocytes and fibroblasts (Contreras O et al., 2019, Driskell RR et al., 2013).

Our findings that differentiated adipocytes and fibroblasts remain committed to their lineages during the healing process directly impact our understanding of homeostasis and repair of stromal tissues, impacting both basic and clinical paradigms for wound repair, regeneration, and various cell transplantation strategies for regenerative medicine. Clinically, today's standard of care for skin grafts and scaffold constructs provide closure of a wound area but leave patients with disfiguring and debilitating scars (Krastev TK et al., 2020). Current pre-clinical and clinical studies employ tissue equivalents composed of epidermal and stromal fibroblast populations embedded in various matrices. Incorporating a dermal component into skin equivalents provides mechanical stability and supports a functional repair tissue by preventing stricture and scar formation. Clinically approved grafts, such as Apligraf®, have already received Food and Drug Administration (FDA) approval for usage in venous leg ulcers and diabetic foot ulcers. Clear delineation of stromal subsets, and understanding of their tissue-specific roles and responsiveness to the environmental milieu, is crucial in the development of novel skin substitutes that enable superior 'scarless' regenerative outcomes in the treatment of severe skin defects, burns, accidents, congenital diseases, tumors, or chronic wounds.

Our findings here add to the changes in cell lineage composition by revealing that adult adipocytes are motile responders and undergo morphologic change associated with their repositioning within the challenging environment. We believe that this migratory and morphologic behavior of adult adipocytes nurtured the hypothesis that adipocytes and fibroblasts may cross-convert. This is an essential distinction of equivalent relevance in understanding the origins of fibrosing cells and physiological processes within a wounded or diseased environment. Harnessing adult adipocyte migration and cross-navigation, potentially through TGFβ signaling, would enable innovative interventions for improving fat grafting, soft tissue implantation, and healing, as well as provide new strategies to circumvent or reverse type II diabetes.

Previous studies on adipocyte plasticity fail to address adipocyte migration morphological changes in response to injury (table 2). Our study emphasizes that mature adipocytes are activated upon injury and attain only a migratory fibroblast-like morphology. Still, they do not transition into a myofibroblastic state. We see, <10% of the adipocytes in day 7 wounds are αSMA+, this can be because adipocytes are simply motile cells. In skeletal muscle fibrosis, it is shown that αSMA is not ideal for marking fibrogenic cell activity

(Sun KH et al., 2016). It is also reported that myofibroblasts are a cell state rather than a cell type (Bielczyk-Maczynska E, 2019, Wynn TA 2008, Carthy JM, 2018). DWAT adipocytes are gaining importance in the field of skin scarring. Apart from being involved in thermoregulation, energy storage, defense responses, these cell types can be explored for their therapeutic potential. Lineage restricted adipocytes may potentially decrease ECM rigidity and stiffness, therefore, contributing to less severe scars. This area of research needs to be explored in the future.

Our findings are based on the SCAD model, which originates from Neonatal mice. Further work from an adult mouse SCAD or human ex-vivo skin scar model is needed to fully understand adipocytes' exact role in scar development. However, our study delineates multi-modality in lineage-restricted adipocytes and stromal fibroblasts in their response to tissue injury. Understanding the limitations of lineage interplay between stromal cells provides key knowledge to tissue repair responses central to multiple organ systems. This study also supports translational knowledge for developing novel tissue engineering and stromal cell-based therapeutics for impaired healing, fibrotic disorders, and abnormal scarring.

6. Concluding remarks

Our data suggest that dermal adipocytes and fibroblasts operate as distinct cell types from homeostasis to scar development. Transcriptomic profiles of mature adipocytes and scar-forming fibroblasts isolated from a well-characterized scar development model SCAD shows no interconversion between cell states. Adipocytes remain adipogenic, and fibroblasts remain fibrogenic throughout. During an injury, both adipocytes and fibroblasts are migratory, but adipocytes attain fibroblast-like morphology but remain mature adipocytes. The migratory cells remain lineage-restricted throughout the process of scar development. No instance of cell fusion events in both adipocytes and fibroblasts occurred (Fig. 18 A).

A.

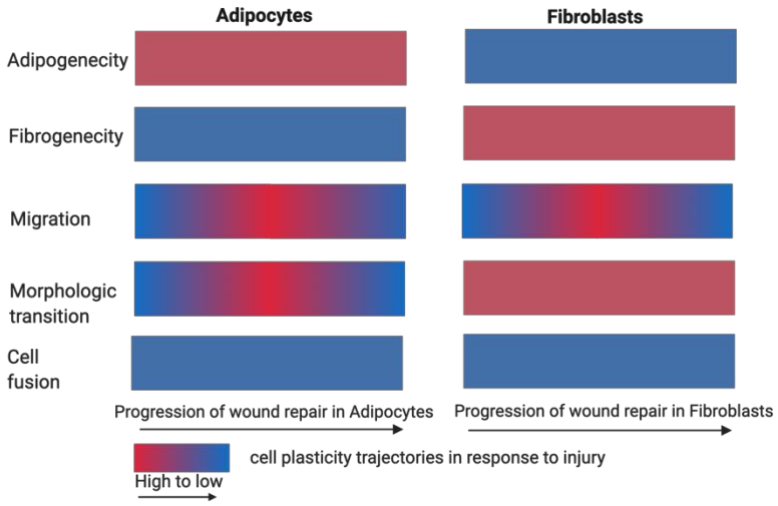

Our study proves the fate of dermal adipocytes and scar-forming fibroblasts during scar formation. A mature adipocyte or fibroblast does not dedifferentiate to precursor cell types or transdifferentiate into completely new cell type. Both cell types instead remain as terminally differentiated cell types and carry out specific biological processes. The possible fate of adipocytes and fibroblasts in response to an injury is summarized in (Fig. 18. B).

B.

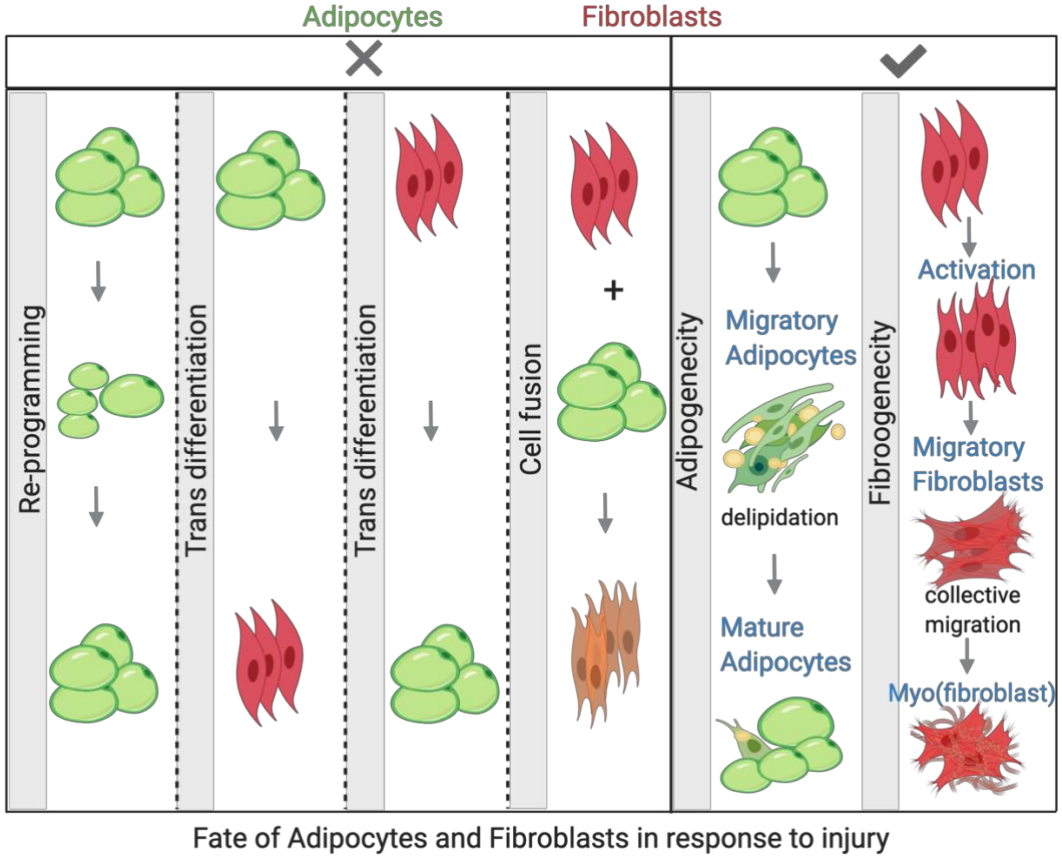

*Figure **18.** **A.** Key plasticity features observed in adipocytes and fibroblasts and their trajectories from homeostasis to scar formation are shown. **B**. The fate of mature dermal adipocytes and fibroblast during scar development.*

The recruitment of adipocytes into wounds has enormous clinical significance. More work is needed to decipher the functional role of adipocytes in wound healing and scar development. Strategies that inhibit fibroblast adhesions and activate adipocytes could help develop anti-scaring therapeutics and regenerative and scarless wound healing.

7. Auxilliary data

A.

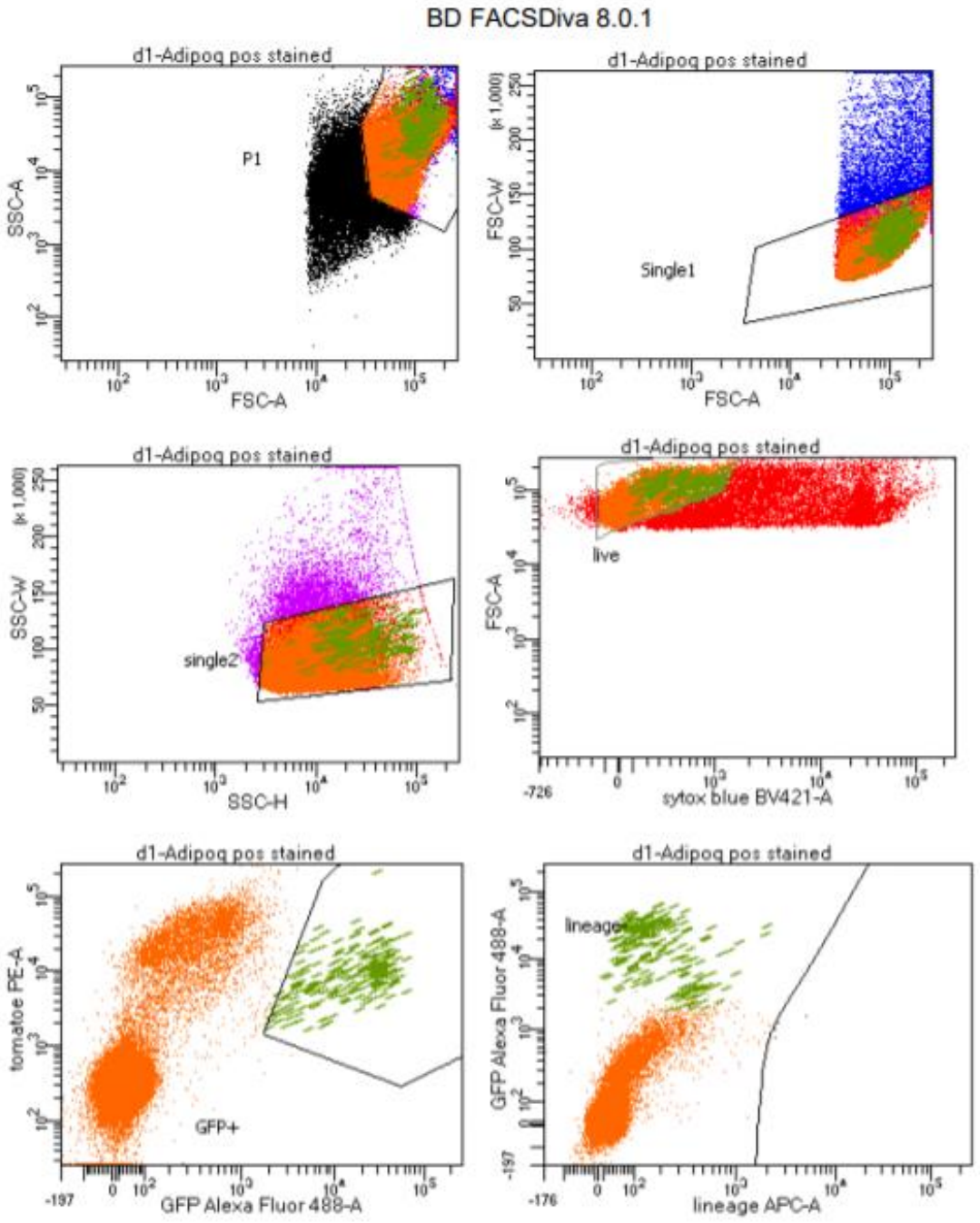

Tube: Adipoq pos stained

Population	#Events	%Parent	%Total
All Events	138,986	####	100.0
P1	95,484	68.7	68.7
Single1	89,249	93.5	64.2
single2	84,611	94.8	60.9
live	69,272	81.9	49.8
lineage-	69,268	100.0	49.8
GFP+	218	0.3	0.2

B.

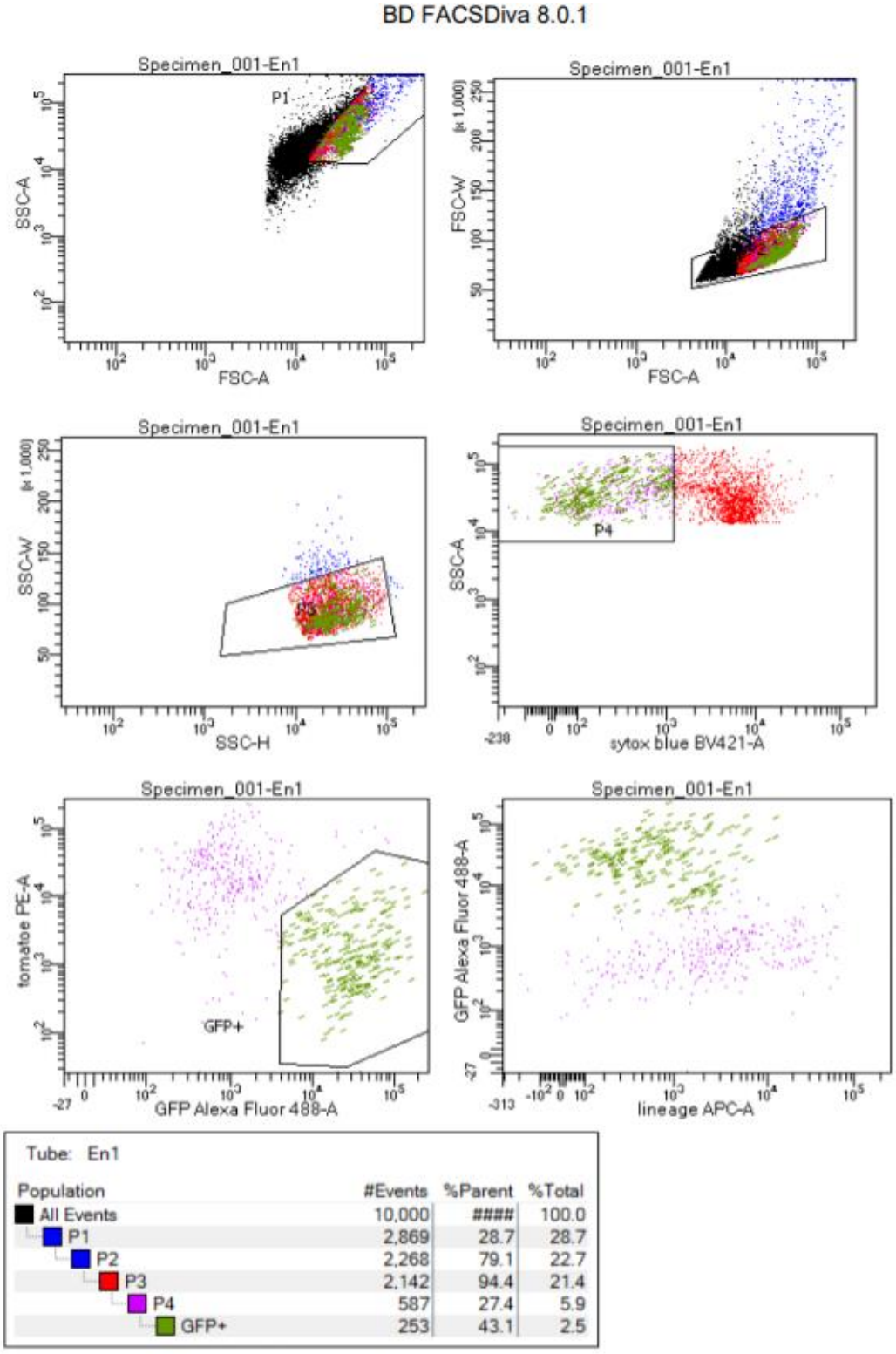

Supplemental Figure S4: Gating strategy for isolating GFP+ adipocytes (A) and GFP+ En1+ fibroblasts (B).

8. Acknowledgments

We thank S. Ussar and F.Ruiz, Institute of Obesity and Diabetes (IDO), Helmholtz Zentrum Muenchen for Adipoq^{cre} mouse, S. Dietzel, Bio-imaging, Core Facility at BMC of Ludwig-Maximilians-Universität München for providing multi-photon system. L.Richter, Core Facility Flow Cytometry (CF FlowCyt) at the Biomedical Center (BMC), Ludwig-Maximilians-Universität for providing support with FACS sorting. Figures were made using Biorender.

9. Author contributions

Y.R. outlined and supervised the research narrative and experimental design. H.B.S. supervised the single cell transcriptomic experiments and analysis. S.K.G. and A.M.S. performed experiments and analysis. D.J. performed FACS sorting and transplantation experiment. J.B. and W.E. performed mcSCRB seq. M.A., I.A. and H.B.S. analyzed mcSCRBseq data. P.R. and S.C. performed 3D imaging, live imaging, and manual cell tracking analysis. D.C.-G. analyzed transplantation experiments. J.W. wrote the animal experimentation protocols. V.L. and C.M. performed the velocity calculations and similarity analysis. Y.R., H.B.S. and S.K.G. wrote the manuscript

.

III Material Methods:

1. Antibodies

The following antibodies were used: Collagen I (procured from Rockland, cat.no. 600-401-103-0.1), Collagen III (Abcam ab7778), N-cadherin (clone GC4, Sigma-Aldrich C3865), Fibronectin (Abcam ab23750), a-SMA (Abcam ab5694), Plin1 (Abcam, ab3526), FSP1 (Abcam, ab58597), PDGFRa (R&D Systems AF1062), Ki67 (Abcam, ab15580), TCF21 (Abcam,ab32981). Fluorophore-conjugated secondary antibodies were procured from Thermo Fisher Scientific.

2. Tissue fixation and cryosections

Skin samples were fixed overnight in 2% PFA at 4C or 4% PFA at RT (room temperature). After removing PFA, samples were washed in PBS 3 times for 5 minutes each. Samples were embedded in OCT and preserved in -80 C., Followed by cryosectioning at 7µm thickness.

3. Immuno fluorescence staining

Cryo-sections were fixed again for 4 minutes in acetone (ice-cold), followed by washing in PBS, 3X times in 5 min incubations. Blocked for 1hr with PBS containing 1% BSA and 5 % of serum in which the secondary antibody was raised, followed by incubation with primary antibodies at 4°C overnight. The next day, after 3X PBS washes, sections were incubated with appropriate fluorophore-conjugated 2^{o} antibodies (Thermo Fisher Scientific) at RT for 1 hour. For double staining, incubation of sections was at RT with the second primary antibody for two hours and appropriate secondary antibody for one hour. Nuclei were counterstained with DAPI (1:5000 dilution in PBS) for 3 min. Mounting was done with Fluoromount-G (Thermo Fisher Scientific cat.no. 00- 4958-02). Photomicrographs were taken with a Zeiss AxioImager with AxioVision software (Carl Zeiss), or a Zeiss LSM 710 with Zen software (Carl Zeiss)

4. Masson's trichrome staining

Cryo-sections were fixed for 5 min in ice-cold acetone (-20°C) and incubated O/N in Bouin's solution (Sigma-Aldrich HT10132) at RT. After washing in cold tap water, the sections were stained with the working solution of Hematoxylin (Weigert's Iron Hematoxylin, Sigma-Aldrich HT1079) for 5 min. After that, the sections were treated with a Masson's trichrome stain kit (Sigma-Aldrich, cat no. HT15) by sequentially incubating at room temperature for 5 min in Biebrich scarlet-acid fuchsin reagent, the working concentration of Phosphomolybdic/ Phosphotungsticacid (5 min), followed by aniline blue solution (10 min), and later acetic acid (1%, 2 min). After dehydration, the sections were cleared with Roti-Histol and mounted with a Roti-Histokitt (Cat.no. Roth 6640 and 6638, respectively). Cell counting was performed with ImageJ. Briefly, trichrome images were converted to CMYK, and the black channel was used to count the iron hematoxylin stained nuclei. Regions of interest covering the scar area were delimited and processed using the functions of subtracting background (rolling ball = 50 px), enhance contrast (saturated = 0.1 normalized), Unsharp Mask (Radius;2 and Mask; 0.6), Median (radius;1) and the auto- threshold method "Minimum." The watershed function was used in the binary images, and the particles were counted (size threshold = 30-200 px2). For the quantification of scar areas, trichrome images were converted to CMYK, and the cyan channel was used to evaluate the collagens stained in blue.

5. Whole-mount bright-field imaging

SCAD tissues were fixed overnight with 2% PFA at temperature 4°C and washed 3X times using PBS. Bright-field images of whole SCADs were taken with a Leica M50 stereo-microscope (Leica) with a Leica DFC310 FX camera (Leica) and saved with Leica Application Suite (v4.8).

6. 3D imaging

6.1 Laser scanning microscopy with tissue-clearing

3 DISCO protocol was modified and later used in the study for staining and clearing. Briefly, fixed samples were pre-incubated in Dulbecco's Phosphate-Buffered Saline (Thermo Fisher Scientific, cat.no 14190169) containing gelatin (0.2% , Sigma, cat.no. G1393), Triton-X100 (0.5% , Sigma, cat.no. X100) and lastly Thimerosal (0.01% ,

Sigma, cat.no T8784). This solution was called PBS-GT, and samples were incubated for 24 hrs at RT with gentle shaking. Antibodies: anti elastin (Abcam, ab21610), anti-fibronectin (Abcam, cat.no. ab23750), and anti-collagen type I (procured from Rockland, cat.no. 600-401-103), were pre-labeled with Alexa Fluor 488, 594, and 647 dyes (Thermo Fisher Scientific, cat.no. A20181, A20184, A20186) according to the instructions provided by the company. The samples were later incubated, rotating, with the labeled antibodies in PBS GT (1:1000) for 24h at RT. After washing in PBS-GT, samples were 1st dehydrated in THF (Sigma, cat.no. 186562) series of (50% then 70%, next 80%, 3 times 100%; 30 minutes each), then dichloromethane was used for clearing (Sigma, cat.no. 270997) for 30 min and later placed in using benzyl ether (Sigma cat.no 108014). Post clearing, the tissue was placed on a 35 mm dish (ibidi cat. no. 81218), glass-bottom Zeiss LSM 710 microscope. Raw data was processed and optimized for visualization, adjusting brightness, and contrast with Imaris image analysis software (version 9.1.0, Bitplane, UK).

6.2 Multi-photon microscopy without clearing

Whole-mount SCADs were processed for immunostaining, followed by embedding NuSieve GTG agarose (2%, Lonza, cat.no. 859081) in a 35mm petridish (Falcon, cat.no. 351008), and imaging is done using Leica SP8 MP (Leica, Germany). Post this, the merging of tiles was done offline using the LAS X software (v4.8, Leica) using smooth overlap blending. Lastly, all data were visualized using Imaris image analysis software (versions 9.1.0 and 9.3.1 Bitplane, UK) using contrast and brightness adjustments.

7. Mouse lines

Wild type C57BL/6J mouse lines at the PO/P1 stage were used for generating Dermastillas and SCADs. The animal facility at Helmholtz center Muenchen housed all the mice used in the study. The rooms continuously received constant temperature and humidity. 12 h light cycle was followed, and animals were provided with food and water ad libitum. Every animal experiment conducted agreed (reviewal and approval) with the Government of Upper Bavaria. Registration was done with project ROB TVA number Gz. 55.2-1-54-2532-61-2016 and performed under strict national and international guidelines. The current study is docile with all necessary ethical requirements related to research using animals.

8. Generation of Dermastilla

The dorsal back skin of the PO/P1 stage of mice was harvested. Tissue was minced to generate small chunks of skin and filtered using a 500micron filter. The resulting tissue suspension was complete suspension media (DMEM/F12 -Cat no; 10%FBS- cat no; 1X pen strep, 1X Glutamax, 1X NEAA). 20ul of suspension was placed as a single drop on top of the lid of a Petri dish. The bottom plate was filled with water to hydrate the setup. Hanging drops were cultured for up to 5 days, and media replenished alternate day.

9. SCar in A Dish (SCAD) explant culture

Back-skin was collected from newborn (postnatal day 0 to day 1) C57BL/6J or two-color membrane reporter $En1^{Cre}$; $R26^{mTmG}$ / $Adipoq^{Cre}$; $R26^{mTmG}$ or nuclear reporter $En1^{Cre}$; $R26^{LSL\text{-}H2B\text{-}mCherry}$ / $Adipoq^{Cre}$; $R26^{LSL\text{-}H2B\text{-}mCherry}$ mice, and washed twice with cold DMEM/F-12 (Thermo Fisher Scientific 11320074) medium to remove contaminating blood, and then washed once with HBSS (Thermo Fisher Scientific, cat.no. 14175095). After careful removal of ventral non-skin tissue with a surgical scalpel, round skin pieces were cut out with a disposable Ø 2 mm biopsy punch (Stiefel, cat.no. 270130) down to bellow the panniculus carnosus muscle and cultured in 200 µl of DMEM/F-12 medium containing 10% FBS, 1x GlutaMAX (Thermo Fisher Scientific, 35050038), 1x Penicillin/streptomycin (Thermo Fisher Scientific, cat.no. 15140122), and 1x MEM non-essential amino acids (Thermo Fisher Scientific, cat.no. 11140035) in 96well plates, in a 5% CO2 and humidified in a 37°C incubator. (Note: the 2 mm skin pieces were cultured submerged in medium with the dermal side face up but not floating at the liquid-air interface). Fresh medium was supplied every other day, and the skin tissues were harvested at time points routinely from day 1 to day 5 after culture, with the fresh tissues serving as day 0 control and fixed O/N in 2% PFA at temperature 4° C. After thoroughly rinsing in PBS 3X times, the samples were embedded and frozen. The optimal cutting temperature was used, and 7µm cryo-sections were prepared with a cryostat.

10. Transfection of Dermastilla

Transfection of Dermastilla was using the transfection reagent lipofectamine 2000 (Thermo scientific, cat.no 11668027), and eGFP plasmid DNA produced in-house. Manufacturers instruction was followed for transfection

11. Transfection of SCAD by Lipofection

Transfection of SCAD was using the transfection regents lipofectamine 2000 (Thermo scientific, cat.no 11668027) or Invivofectamine 3.0 (Cat.no: IVF3001). eGFP plasmid DNA produced in-house. In both cases, the manufacturer's instructions were followed.

12. Transfection of SCAD by Electroporation

pMAX GFP plasmid resuspend in nuclease-free water was used. Various voltages between 10volts to 50volts were tried, with a number of pulses =3 and pulse length of 3ms. SCADs were held with the two electrodes' help during pulsing and later placed in sterile cell culture media until putting in a 37^{o} C incubator. The media was changed every alternate day up to 5 days.

13. Transduction of SCAD using Adeno associated virus

SCADs were placed in 96 well (1 SCAD per well with 200ul of complete media). The following day media was replaced by 180ul of OptiMEM (Thermo Scientific, cat.no. 31985062) plus 20µl of ~1X10^{11} Genome copies /ml of purified AAV6 particles. SCADs were incubated with viral particles overnight. The following day, media was replaced with complete media containing 10% FBS. Later, the media was changed every alternate day for up to 5 days.

14. Adeno associated virus production and purification

AAVpro 293 T cell line (Takara Bio, cat.no. 632273) was transfected with pAAV-CRE Recombinase vector (Takara Bio, cat. No. 6654), pRC6, pHelper plasmids obtained from AAVpro Helper Free System (Takara Bio, cat.no . 6651) and pAAV-U6-sgRNA-CMVGFP (Addgene, cat no. 8545142). Next followed the production of AAV6 _GFP virus and Cre recombinase virus. PEI was used as the transfection reagent, and the viral harvest was done 96 hours later. Extraction and purification were done using the AAVpro purification kit (Takara Bio, cat.no 6666). Titer measured using qRTPCR. Modifications to the manufacturers' protocol were made to achieve a high titer virus.

14.1 Revival and scale-up of AAVpro HEK293T producer cell line

AAVproHEK293T cells were quickly thawed in a 37°C water bath, 5ml of growth medium was added and centrifuged at 1000rpm for 5mins. Pellet was resuspended with 2ml of growth medium and plated in an appropriate cell culture dish. Growth Medium consisted of 90% DMEM containing high glucose (4.5 g/L), L-glutamine (4 mM), and Sodium Bicarbonate (Sigma-Aldrich, cat no. D5796); Fetal Bovine Serum (FBS, 10%); penicillin G sodium (100 units/mln); and Streptomycin Sulfate (100 µg/ml). Sodium Pyruvate at a concentration of 1 mM (Sigma-Aldrich, cat.no. S8636) was added to make complete growth media.

14.2 Transfection of AAVpro HEK293T cells

10 x 10^6 AAVpro 293T cells were plated per T225 flasks. Cultured overnight. The transfection reagent was Polyethyleneimine (PEI) and used at 1mg/ml concentration. DNA: PEI ratio was 1:4 for Capsid and expression plasmids (36µg: 144µl of PEI). DNA: PEI ratio was 2:4(72µg: 144µl of PEI) for pHelper plasmid. The complex was made in 5 ml of Opti-MEM® (Thermo Fischer, cat no. 31985062). Vortexed for 15 seconds vigorously for proper mixing, and the complex was incubated at RT for 15-20 mins. Later, the DNA: PEI complex was added dropwise to the flask and incubated at 37° C, O/N. Media was changed on the following day, with complete growth medium containing 2% FBS and cultured for 96 hrs at 37°C.

14.3 Harvest and cell lysis

AAV producing cells were detached by the addition of 1/80 volume of 0.5 M EDTA at pH 8.0 to each t225 flasks. Following this was, incubation at RT for 10 mins and later centrifuged for 10 min, at speed 2,000g, at 4℃. Centrifugation was repeated to remove any remaining supernatant. The cell pellet was then taken for the extraction of viral particles. AAV extraction kit from Takara bio was used.

14.4 Viral particle extraction

Pellet was loosened for no remnant of cell lump for efficient purification. The extraction was carried out using AAV extraction Solution A plus, followed by vigorous vortexing and incubation at room temperature for 5 minutes. Continuous vortexing was carried out

until there were no remaining cell clumps. Centrifugation was then carried out for 10 min, at 4,000 to 9,000g at 4℃. Next, supernatant, which contains AAV particles, was collected in a new sterile centrifuge tube using a pipet to avoid contamination. 1/10 volume of AAV extraction Solution B was added. After this step, samples could be stored at -80℃. Alternatively, we proceed to the next step. But significantly, we noted with every freeze-thaw, the efficiency of AAV goes down.

14.5 Purification and concentration of AAV particles

The swinging bucket rotor was used for purification steps. 1/100 volume of Cryonase cold active Nuclease was added to the viral particle solution from the previous step and followed by an incubator for 1hr in a 37^{o}C water bath. Protein precipitation was carried out by adding 1/10th Precipitator A and vortexing for 10 seconds. Later this was incubated at 37℃ for 30 min and vigorously vortexed again for 10 seconds. It was noted that Precipitator A would produce a white precipitate, but this does not affect the performance of the reagent. Next, 1/20 volume of precipitator B was added to the solution, vortexed again for 10 seconds, and centrifuged at 5,000 - 9,000g for 5 min at 4℃. Later, filtration of the supernatant was carried out using a Millex-HV 0.45μm filter.

The filtrate containing AAV vector was added to an Amicon Ultra-15,100 kDa filter, Centrifuged for 5 min, at 2,000g at 15℃ until the AAV solution in the filter is <1.5 ml. Note: We continued to centrifuge, if the volume of the solution was >1.5ml. After removing the filtrate, 5 ml of Suspension Buffer was added to the Amicon Ultra-15 filter unit cup. Mixed and centrifuged for 5 min, at 2,000g at 15℃, until AAV solution inside the filter was <1.5 ml.

Repeated the addition of 5ml into the filter unit (total five times) to obtain an appropriate solution volume. Note: If the volume of the solution was >1.5 ml, continue to centrifuge. The volume and time of centrifugation are critical in this step. After discarding the filtrate, we resuspended the solution inside of the cup of the Amicon Ultra-15 (100 kDa) filter unit by pipetting or vortexing for 30 seconds and transfer the solution to a new tube. 50-100μl aliquots of the virus were made and stored at -80C for long-term use. Separate aliquots for analysis (Titer measurement by qPCR- vector genome assay, western blot-purity, and biological titer measurement FACS) were made to avoid freeze-thaw.

14.6 Viral titer measurement: Vector genome Assay

Extraction of AAV Vector Genome. AAV particle solution was treated with DNase I and incubated at 37℃ for at least 15 minutes to digest free genomic DNA and plasmid DNA derived from host cells and followed by inactivation of DNase I by heat treatment at 95℃ for 10 minutes. An equal amount of Lysis Buffer (20 µl) was added, followed by incubation at 70℃ for 10 minutes. AAV vector genome solution was diluted at least 50-fold using EASY Dilution and used directly as a real-time PCR template.

14.7 Real-Time PCR

5 µl of the diluted AAV vector genome solution was the template for RT- PCR. At the same time, use the Positive Control to prepare the standard curve.

Step 1: Sample Preparation for Standard Curve. Dilute the Positive Control using EASY Dilution to obtain the samples for standard curve preparation. (Use 5 µl of each solution as a template for real-time PCR.) Start with 2 x 107 copies/µl (Positive Control solution), next 2 x 106 copies/µl (5 µl of Positive Control solution + 45 µl of EASY Dilution), next 2 x 105 copies/µl (5 µl of (2) + 45 µl of EASY Dilution) and so on up to at least 6 dilution to get the final dilution at 2 x 102 copies/µl (5 µl of (5) + 45 µl of EASY Dilution)

Step 2: 50X Primer mix was prepared before use. 5 µl of AAV Forward and reverse primer was diluted in TE or water to 25µl.

Step 3: Preparation of the qPCR Reaction mix for LC 480 Roche Reaction mixtures was prepared. SYBRPremix Ex Taq II (2X conc.) 12.5 µl, 50X Primer mix 0.5 µl, dH2O 7.0 µl, Template (5.0 µl), Final volume to 25.0 µl. Negative control with 5 µl of dH2O in a separate tube was also included. Finally, 5 µl of the template (the sample DNA solution from step 1 and the control vector for standards) was added to the reaction solutions

Step 4: Real-Time PCR Reaction was carried out as follows. Initial denaturation at 95℃ for 2 minutes, denaturation at 95℃ for 5 seconds, extension at 60℃ for 30 seconds. 35 cycles and SYBR Detection of Fluorescence was used.

Step 5: Quantification: Standard Curve is generated with Positive Control. Viral Titre is calculated after exporting the CP values of each of the samples.

15. Local N-cadherin knockout in full-body R26Cas9 or Ncad fl/fl wounds

A guide RNA (gRNA) targeting exon 1 of mouse N-cadherin was designed with the Benchling tool. The adeno associated virus serotype 6 (AAV6) expressing gRNA targeting murine N-cadherin (TCCGGCACATGGAGGCGGAG) was created by cloning gRNA into the SAP1 sites of pAAV- U6-sgRNA –CMV -GFP plasmid (Addgene Cat.no: #8545129 378). N-cadherin gRNA expressing AAV6 (AAV6- NcadgRNA- GFP) was prepared by transfecting AAVpro 293 T cell Line (Takara Bio, cat.no. 632273) with pAAV- U6- NcadgRNA- CMV- GFP plasmid, pRC6 plasmid dictated serotype 6 expressions, and pHelper plasmids from the AAVpro Helper Free System (Takara Bio, cat.no. 6651). Cre recombinase expressing AAV6 (AAV6-Cre-GFP) was purchased from Addgene (Addgene, cat.no. #6854430). Transfection was performed using a Polyethyleneimine transfection reagent, and viruses were harvested 96 hours post-transfection. AAV6-NcadgRNA-GFP or AAV6-Cre-GFP or control AAV6-GFP viruses were extracted and purified with an AAVpro purification kit of all serotypes (Takara Bio, cat.no. 6666). Two 2-mm excisional wounds were created (full-thickness) on the dorsal back of anesthetized mice. The age of mice was 13 days. Full-body Cas9-expressing R26Cas9 mice or CRISPR/Cas9-based local N-cadherin ablation was performed by subcutaneously injecting 20 µl of AAV6-gRNA-GFP virus at a viral titer of $1x10^{12}$ GC/ml at the area between the two wounds at day 0, day 5, and day10 post-wounding. The mice received a subcutaneous injection of the AAV6-GFP virus without gRNA as control. Similarly, two 2-mm excisional wounds were created (full-thickness) on the back of anesthetized 5 days old homozygous N-cadherin floxed Ncad fl/fl mice. These mice had loxP sites flanking exon 1 of the N-cadherin gene. Local N-cadherin ablation was performed by subcutaneously injecting 20 µl of AAV6-Cre-GFP virus at a viral titer of $2x10^{12}$ GC/ml at the area between the two wounds at day 0, 5, and 10 post-wounding. The mice received a subcutaneous injection of the AAV6-GFP virus as control. Scar tissues were harvested at day14 post-wounding. Scar images were documented with a Leica M50 stereo-microscope (Leica) at 4x magnification. Subsequently, the scar tissue was processed for cryo-sections for histology and immunofluorescence.

16. Transgenic & reporter mouse lines

En1^{Cre} (JAX stock No. 007916), ROSA26$^{LSL\text{-}H2B\text{-}mCherry}$ (R26$^{LSL\text{-}H2B\text{-}mCherry}$) (JAX stock No. 023139), Rag2–/– mice, and ROSA26 ^{mTmG} (R26^{mTmG}) reporter mice were from Stanford University (16). Adipoq^{Cre} (Jax stock No.028020) mice were from Helmholtz Center. En1^{Cre} or Adipoq^{Cre} transgenic mice were crossed with R26 ^{mTmG} or R26$^{LSL\text{-}H2B\text{-}mCherry}$ reporter mice for the described experiments. Animals were housed at the Helmholtz Center animal facility rooms maintained at constant temperature and humidity with a 12-h light cycle. Animals were given food and water ad libitum. All experiments were reviewed and approved by the Government of Upper Bavaria and registered under the projects 55.2-1-54-2532-61-2016 and 55.2-2532-02-19-23 and conducted under strict governmental and international guidelines. This study is compliant with all relevant ethical regulations regarding animal research.

17. Mouse genotyping

Cre^{+} animals from double-transgenic reporter mice were classified based on appropriate fluorescence present in the mice's dorsal back. A fluorescence microscope was used for the identification of Cre^{+} neonatal mice. For adult mice, genotyping was performed to detect a 200 basepair Cre band (fragment). Every time filter tips were used to prevent cross-contamination. Genomic DNA was extracted normally from ear clip tissue. Quick Extract (QE) DNA extraction solution (Biozym, 101094) was used. Extracted Genomic DNA solution- 1 µl, was added to each PCR reaction mix containing 24 µl. The PCR reaction mixture was prepared by using Taq PCR core kit (Qiagen, 201205) containing Coral buffer (1X concentration final), dNTPs (10mM each), Taq polymerase enzyme (0.625 units per reaction), 0.5µM of each forward primer (FP) 5′ ATT GCT GTC ACT TGG TCG TGG C-3' and reverse primer (RP) 5′ GGA AAA TGC TTC TGT CCG TTT GC-3′. PCR cycling temperature was set to 10 minutes at 94°C for initial denaturation, followed by amplification of 30 cycles, 30 seconds denaturation at 94°C, 30 seconds, annealing for 56°C, 30 seconds, elongation 72°C. Lastly, the final elongation at 72°C for 8 minutes and an infinite temperature of 10°C was maintained. Negative controls with no template and positive controls were included. The Eppendorf master cycler instrument was used, and samples were analyzed by agarose gel electrophoresis

18. Ex-vivo explant culture

Back-skin was collected from newborn (postnatal day 0 to day 1) two-color membrane reporter $En1^{Cre}$; $R26^{mTmG}$ or $Adipoq^{Cre}$; $R26^{mTmG}$ reporter or $En1^{Cre}$; $R26^{LSL\text{-}H2B\text{-}mCherry}$ mice or $Adipoq^{Cre}$; $R26^{LSL\text{-}H2B\text{-}mCherry}$ nuclear reporter mice, and washed twice with DMEM/F-12 (Thermo Fisher Scientific, 11320074) medium to remove contaminating blood, and then washed once with Hank's Balanced Salt Solution (HBSS, Thermo Fisher Scientific 14175095). Dorsal back skin was cut out, and explants were made using a disposable Ø 2 mm biopsy punch (Stiefel, 270130) down below the panniculus carnosus muscle and cultured in 2 ml of DMEM/F-12 medium containing 10% FBS, 1x GlutaMAX (Thermo Fisher Scientific, 35050038), 1x Penicillin/streptomycin (Thermo Fisher Scientific, 15140122), and 1x MEM non-essential amino acids (Thermo Fisher Scientific, 11140035) in 6 well plates, in a humidified 37°C, 5% CO2 incubator. Fresh medium was supplied every other day, and the skin tissues were harvested at the indicated time points (day 1 to day 5 after culture), with the fresh tissues serving as day 0 control. Post harvesting on designated days, explants were fixed in 2% paraformaldehyde (PFA) overnight at 4ºC for whole-mount imaging and Immuno-labeling or directly used for live imaging by multi-photon microscopy or mcSCRB-seq experiments.

19. Sorting of adipocytes and fibroblasts

Transgenic mouse lines ($En1^{Cre}$; R^{26mTmG} or $Adipoq^{Cre}$; $R26^{mTmG}$) were used for sorting at the P0 or P1 stage. Multiple skin explants for each day were pooled to maximize yield. Tissue was minced and digested using 0.5mg/ml Collagenase A (Sigma Aldrich, 10103586001) and 25u/ml of DNase 1 (Sigma, 10104159001) for 1hr at 37˚C with shaking. Cells were washed with complete media and filtered through cell strainers. Centrifugation was carried out for 5 min at 200g, and the cell pellet was resuspended in 1 ml of FACS buffer containing 2% FBS in PBS. Adipocyte and fibroblasts sorting were performed based on GFP^{+} fluorescence. $En1^{Cre+}$ fibroblasts were incubated with the following antibodies for lineage-negative gating. 1 µg of APC-conjugated anti-mouse PECAM-1 (CD31)(Biozol, BLD-102410), CD45 (Biozol, BLD-103112), Ter119 (Biozol, BLD-116212), Tie2 (CD202b) (BLD-124010) and EpCam (CD326), (Biozol, BLD-118214) antibodies and eFluor660 conjugated anti-mouse Lyve-1 (ALY7) (Thermo Fisher Scientific, 50-0443-82) in FACS buffer (2% [v/v] FBS in phosphate-buffered saline [PBS]), on ice for 30 min. Later washed with 5 ml FACS buffer, the antibody-

conjugated cell pellet was resuspended in 1 ml of FACS buffer (PBS +2% FBS). The cells were sorted using the instrument FACS Aria III sorter and 120µm nozzle. The lineage minus fibroblasts were sorted (Lin-TomatoRed^{-}GFP^{+}) and adipocytes (TomatoRed^{-}GFP^{+}) based on TomatoRed and GFP fluorescence.

20. Single-cell sorting of cells for mcSCRB-seq

mcSRCB-seq was performed with 1000 each adipocyte and fibroblasts sorted from day 1 and day 4 explants. Indexing parameter in Aria III was used, and cells were sorted directly into 96-well DNA LoBind plates (Eppendorf). Each well was aliquoted with 5 µl lysis buffer before sorting. Lysis buffer consisted of Guanidine Hydrochloride (5M concentration; Sigma Aldrich), β-Mercaptoethanol (1%, Sigma Aldrich), and Phusion High fidelity (HF) buffer (1:500 dilution, New England Biolabs: M0531L). Immediately post sorting, plates were spun down, placed on dry ice, and later frozen at -80° C.

21. cDNA synthesis step of mcSCRB-seq (pre-amplification step)

A complete step-by-step protocol for mcSCRB-seq is deposited in the protocols.io repository (Bagnoli et al., 2018). Before preparing libraries, SPRI beads (1: 2 ratio) were used to clean up each well. Beads were resuspended in 4 µl double distilled water along with a mix of reverse transcription master mix (5 µl) containing Maxima H- RT enzyme (20U, Thermo Fisher), Maxima H buffer 2x (Thermo Fisher), dNTPs at concentration 2 mM each (Thermo Fisher), template switching oligo (from IDT) 4µM and Polyethylene glycol (PEG) 8000 15% (Sigma-Aldrich). After the addition of 1µl of 2µM barcoded oligo-dT primer (E3V6NEXT, Integrated DNA technologies), cDNA was prepared according to the mcSCRBseq protocol. Template-switching and cDNA synthesis was performed at 42 ° C for 90 minutes. Barcoded cDNA was later pooled in 2 ml DNA LoBind tubes followed by clean-up using SPRI bead buffer. Purified cDNA was eluted in 17 µl and residual primers digested with enzyme Exonuclease I (from Thermo Fisher) at 37 ° C for 20 min. After heat-inactivation at 80 ° C for 10 min, 30 µl PCR master mix containing Terra direct polymerase, 1.25 Units (Clonetech), Terra direct buffer 1.66 X, and SINGV6 primer (IDT) 0.33 µM, was added. PCR cycling was done as follows: 98 ° C, 3 min for initial denaturation, 19 cycles of 15 seconds at 98 ° C, 65 ° C for 30 seconds, and at 68 ° C for 4 minutes. Lastly, the final elongation was performed at 72 ° C for 10 minutes.

22. scRNA-seq library preparation

All the samples were purified with SPRI beads (ratio 1: 0.8) following pre-amplification. The final elution was in 10 µL of H2O (Nuclease free water purchased from Invitrogen). Later cDNA was quantified using the Quant-iT PicoGreen double-stranded DNA Assay Kit (Thermo Fisher). A high Sensitivity DNA chip (Agilent Bioanalyzer) was used to check size distributions. Samples that passed the quality and quantity control parameter were taken for constructing Nextera XT libraries from 0.8 ng of pre-amplified cDNA. Later, 3' ends enriched with a custom made P5 primer (P5NEXTPT5, IDT) during PCR of the libraries. Following this, Libraries were subsequently pooled and selected based on their size using 2% E-Gel Agarose EX Gels (Life Technologies). A size range from 300 bp (base pair) to 800 bp was cut out extracted using the MinElute kit (Qiagen). All procedures were in accordance with the manufacturer's recommendations.

23. Sequencing of scRNA-seq libraries

Illumina HiSeq 1500 instrument was used to sequence libraries. Paired-end sequencing of libraries was done on high output flow cells. To generate molecular and cellular barcodes, 16 bases were sequenced with the 1st read, 50 bps sequenced in the 2nd read into the cDNA fragment, and 8 bases were read to obtain the i7 barcode.

24. mcSCRB data analysis

24.1 Primary data processing of RNA-seq data

Processing all raw FASTQ data was done using the zUMI pipeline and STAR to obtain expression profiles for barcoded UMI data (Bagnoli et al., 2018, Parek S et al., 2018). Mapping was done to the reference genome (mm10 / 09) concatenated with the ERCC and GFP reference. Gene annotations were obtained from Ensembl (GRCm38 / mm10 - GRCh38.84).

24.2 Processing of SCRB-seq single-cell data set

The raw count matrices output by the zUMI pipeline were analyzed using Scanpy (Wolf FA et al., 2018) (v.1.6.0). For barcode filtering, we excluded barcodes with less than 1000 detected genes. We assessed the number of unique molecular identifiers (UMIs) for each

sample using violin plots and retained cells with a number of UMIs below 250000. Genes were only considered if they were expressed in at least 3 cells in the data set.

Normalization was performed based on scran's approach (Lun AT et al., 2016), in which size factors are calculated and used to scale the counts in each cell. Log transformation was used via Scanpy's pp.log1p. The unsupervised clustering was performed separately on these two groups to improve the distinction across the Adipocyte and Fibroblast lineage. Day 1 and day 4 adipocytes were assigned to the first subset and day 1 and day 4 Fibroblasts to the second subset. For the first subset (adipocytes), the top variable genes were established with scanpy's pp.highly_variable_genes and flavor set to "cell_ranger." After excluding genes associated with the cell cycle, 319 genes remained. These highly variable genes were the basis for the Principal Component Analysis (PCA) and neighborhood graph construction via pp.pca and pp. neighbors (n_pcs = 15, n_neighbors = 5). For clustering, the Louvain algorithm was employed at resolution 0.5, resulting in 6 clusters within the adipocyte population. For the second subset (fibroblasts), the highly variable gene list was established likewise and led to 1586 genes. These were used for PCA and neighborhood construction with slightly altered parameters as more cells were in this subset (n_pcs = 20, n_neighbors = 10). As we anticipate a small fraction of contamination with adipocyte cells in the fibroblast labeled population, we cleared away such adipocyte cells. For that, we assessed the similarity to adipocytes for each cell in the fibroblast subset with scanpy's tl.score_genes function, using an adipocyte reference signature (adipocyte cell type from Mouse Cell Atlas, link: http://bis.zju.edu.cn/MCA/gallery.html?tissue=Neonatal-Skin,cluster3). Unsupervised Louvain clustering at resolution 1 revealed one cluster with particularly high scoring cells, which was then removed from the analysis. PCA and neighborhood graph was recalculated on this filtered fibroblast subset (n_pcs = 15, n_neighbors = 20), and Louvain clustering was performed at resolution 0.6, resulting in 6 clusters within the fibroblast population. For both subsets, the UMAPs and diffusion maps were generated using Scanpy's functions tl.umap and tl.diffmap.

For the comparison of both lineages, the two refined subsets were re-combined into one object, and the list of variable genes set to the union of the list established on the two subsets. The PCA was re-calculated and the neighborhood graph established for the

concatenated object (n_pcs = 15, n_neighbors = 20). Cell type marker genes for the 12 subclusters were established with tl.rank_genes_groups and method = "wilcoxon."

24.3 Differential gene expression across the two lineages

We performed differential expression analysis with diffxpy (v.0.7.4). In a first analysis, we compared the differences between adipocyte and fibroblast lineage using the Wald test. To circumvent the problem that specific genes are highly upregulated in only one of the 6 subclusters per lineage, we constrained the model to each subcluster by adding constraint_loc = {subcluster: lineage} to the model. Genes are labeled as differentially expressed if their Benjamini-Hochberg corrected p-value was less than 0.5, have a log2foldchange of greater than 1, and are expressed in at least 10% of cells in the relevant lineage. This resulted in a list of 88 genes for adipocytes and 198 genes for fibroblast. Gene Set Enrichment Analysis was performed using these differentially regulated genes as input for the python package GOATOOLS (Klopfenstein DV et al., 2018).

25. Whole-mount 3D imaging by multi-photon microscopy

Post fixation, explants were thoroughly washed in PBS 3X times, 1 hour each, followed by embedding in NuSieve GTG agarose (2%, Lonza, cat.no. 859081) in a 35mm dish (Falcon, cat.no. 351008). Imaging was done under a Leica SP8 Multiphoton microscope (Leica, Germany). Merging of tiles was done using the LAS X (v4.8, Leica) with smooth overlap blending. Data was finally visualized with Imaris image analysis software (v9.1.0 and v9.2, Bitplane, UK) using contrast and brightness adjustments.

26. Live 3D multi-photon microscopy

For Live imaging using multi-photon microscopy, live samples were embedded as just above. The imaging medium was the same as the complete medium used for explant culture, but with DMEM/F-12, no- phenol red (Life technologies, 11039021) was used. Time-lapse imaging was performed over 15 hours under the multi-photon microscope. A modified incubation system, with heating and gas control (ibidi 10915 & 11922), was used to guarantee physiologic and stable conditions during imaging. Temperature control was set to 37°C with 5% CO2-supplemented air. 3D data were processed with Imaris 9.1.0 (Bitplane, UK) and ImageJ (1.52i). Contrast and brightness were adjusted for better visibility

27. Manual cell tracking

Manual cell tracking was performed on explants from nuclear reporter lines ($En1^{Cre}$; $R26^{LSL\text{-}H2B\text{-}mCherry}$ or $Adipoq^{Cre}$; $R26^{LSL\text{-}H2B\text{-}mCherry}$). ImageJ software with the "Manual Tracking" plugin (version 2.1.1) was used. In brief, an area of 700µm X 700µm in the explant's scar region was cropped from 3D-Time lapse datasets. Nuclear spots were identified after subjecting to maximum-intensity projection. The migration of individual cells was tracked over time. Trajectories and individual track information with coordinates were exported as TIFF and excel files, respectively. Graphical visualization and analysis of these trajectories were performed using "R." Iterative loops to generate a color-ramp for each track as a function of time and embedded into respective coordinates (Blue; first-time point; Red; last time point). Cell movement pattern was quantified based on whether a cell moved away (towards to epidermis) or towards the scar region (center of the explant).

28. Automated cell tracking

Automated cell tracking was done using 3D-Time lapse datasets of whole explants made from nuclear reporter lines using Imaris software package (v9.2.1, Bitplane, UK). Live videos were generated with a 15 min interval from the explant stages of day 1 and day 4. Tracks were generated from 3D data using mcherry fluorescence and an intensity-based spot detection tool. The resulting data indicating the nuclei of Cre-positive cells were filtered for quality. Tracks were visualized in time-coded color representation, ranging from purple to Red. For snapshot images, full tracks representation of the last 10 time points is shown for better visibility and to prevent overcrowding. Dragon tail representation is used in live videos to visualize better directed collective and non-directed migration patterns.

29. Quantification of cell migration

We calculated the displacement in 3D for every cell between consecutive time frames employing the tracked cell trajectories. To compare experiments, mean cell displacements are added up and plotted over time. To analyze the movement similarity of neighboring cells, the neighborhood is determined via Delaunay triangulation. Neighbors are defined as cells that are direct neighbors in the resulting

neighborhood graph. Next, the 3D movement vectors for a cell and its neighbors for consecutive time points are calculated. The 3D movement similarity for cell 'u' and neighbor 'v' can be assessed by calculating the intermediate angle between the respective movement vectors:

\begin{equation}
\label{eq:angle3d}
\alpha_{u,v}= \mbox{cos}^{-1}\biggl(\frac{u_{x}v_{x}+u_{y}v_{y}+u_{z}v_{z}}{\sqrt{u_{x}^2+u_{y}^2+u_{z}^2}\sqrt{v_{x}^2+v_{y}^2+v_{z}^2}}\biggr)
\end{equation}

Finally, all angles are averaged to produce one movement similarity score. The angles are inverted for display reasons, and the movement similarity ranges from 90° (random movement) to 180° (coordinated movement).

30. Whole-mount immunostaining

Whole-mount samples were pre-incubated in Dulbecco's Phosphate-Buffered Saline (DPBS, Thermo Fisher Scientific 14190169) containing 0.2% gelatin (Sigma G1393), 0.5% Triton-X100 (Sigma X100), and 0.01% Thimerosal (Sigma T8784) (PBS-GT) for 24h at room temperature. Followed by incubation with primary antibodies. The following antibodies were used: Collagen I (1:200 Rockland, cat.no. 600-401-103-0.1), Collagen III (1:200, Abcam ab7778), Fibronectin 1 (1:250, Abcam ab23750), a-SMA (1:200 Abcam ab5694), Plin1 (1:200 , Abcam, ab3526), FSP1 (1:200, Abcam, ab58597), PDGF R alpha (1:200, R&D Systems AF1062), Ki67 (1:200, Abcam, ab15580), TCF21 (1:250, Abcam,ab32981). Primary antibody incubation was carried at room temperature for 72 hours, followed by washing with PBSGT, 3X times, 1 hour each. Fluorophore-conjugated secondary antibodies were procured from Thermo Fisher Scientific. The samples were incubated, rotating, with the labeled antibodies in PBSGT (1:1000) for 24h at room temperature. Samples were washed with PBSGT 3X times, 1 hour each, and stored in fresh PBSGT at 4ºC in the dark until imaging.

31. Lipid tox staining

All procedures followed were in accordance with the manufacturer's instructions. HCS Lipid TOX Deep Red (Thermo Scientific, H34477) was used at 1:200 dilution on PFA

fixed whole-mount explants and incubated at 37° C for 2hr. Whole-mount imaging was done using a Multi-photon microscope.

32. Extracellular matrix deposition assay

In-vitro culture of FAC-sorted cells was obtained from transgenic mouse lines ($En1^{Cre}$; $R26^{mTmG}$ or $Adipoq^{Cre}$; $R26^{mTmG}$) at the P0 or P1 stage. Explants from Cre+ mice were collected on day 1 and day 4. Tissue was minced and digested using 0.5mg/ml Collagenase A and 25units/ml of DNase 1 for 1hr at 37˚C with shaking. Cells were washed with complete media and filtered through cell strainers. $En1^{cre+}$ samples were incubated with the following antibodies for lineage-negative gating. Post centrifugation for 5 min at 300g, the cell pellet was resuspended in 1 ml of FACS buffer containing 2% FBS in PBS. Later incubation with antibodies APC- anti-mCD31, mCD45, EpCam (CD326), PECAM-1, mTie2(CD202b), mTer119, antibodies (BioLegend) and eFluor 660 conjugated anti-mouse Lyve-1 antibody on ice for thirty minutes. Later washed with 5 ml FACS buffer, the antibody-conjugated cell pellet was resuspended in 1 ml of FACS buffer (PBS +2% FBS). The cells were sorted using the instrument FACS Aria III sorter with a 120µm nozzle. The lineage minus cells EPFs (Lin-TomatoRed-GFP+) were sorted based on TomatoRed and GFP fluorescence. For $Adipoq^{Cre}$ positive samples, digestion procedures were similar to those mentioned above but excluded lineage markers. En1+ fibroblasts and adipocytes were later plated in 384 well glass bottom plates coated with 1% Porcine Gelatin. 3000 cells were plated per well and cultured in complete medium with or without 5ng/ml recombinant TGFβ1(rTGFβ1). Adipocytes were cultured in complete medium with or without 5ng/ml rTGFβ1 and 5ng/ml bFGF (basal FGF). Both cultures were maintained in a 37ºC incubator for 72 hours, and media was replenished on alternate days.

33. De-cellularization and extracellular matrix immunostaining

Adipocytes and fibroblasts in 384-well plates were cultured for up to 3 days. Confluent EPFs or adipocytes were de-cellularized as described previously (Bonenfant NR et al., 2013, Van der Velden JL et al., 2018, Jiang D et al., 2018). Confluent culture dishes were incubated sequentially at 4°C for 45 mins with very gentle stirring, first in DDW (double distilled water) with Triton X 100 (0.1%), then in freshly prepared 2% sodium deoxycholate. Two 30-minute incubations at room temperature followed them, first in

DDW containing 1 M NaCl and second in DDW containing pancreatic DNase (30 µg/ml, source porcine), MgSO4 (1.3 mM), CaCl2 (2 mM). Plates were later rinsed very gently with distilled water, and 4% PFA was used to fix the deposited extracellular matrix for 15 mins at RT. After washing gently with PBS two times, permeabilization was done in PBS containing BSA (1%) and Triton X (0.1%). Blocking was carried out for 1hr at RT using PBS containing 1% BSA and 10% serum of the species in which secondary antibody was raised. This was followed by primary antibody incubation at 4˚C overnight, gentle rinsing with PBS, and later secondary antibody incubation was done for 1hr at RT. Lastly, nuclei were stained with DAPI for 10mins at RT. Plates were washed 3X times with 1X PBS and stored in PBS, and images were taken with a confocal microscope (LSM 710, Zeiss). Percent fluorescence was measured after converting the images to binary format in Image J and calculating the fluorescence signal area.

34. Adult splinted wound model

0.5 mm Silicone sheets (Grace Bio-Labs, Cat.no. CWS-S-0.5) were used first to prepare the splinted rings. 12 mm outer diameter and inner was 5 mm. Splints were cleaned with detergent and water thoroughly, disinfected, and sterilized using ethanol (70%) for 30 minutes. Splints were later air-dried in a clean cell culture hood and stored in a sterile, airtight container. Mice were anesthetized using MMF. (Volume- 100 µl, MMF-medetomidine, midazolam, and fentanyl). The dorsal back hair was shaved using a hair clipper (Aesculap Schermaschine Exacta). Followed by an additional application of hair removal cream for about 3-5 min. 5 mm diameter biopsy punch (Stiefel) was used to create two full-thickness (excisional wounds). Superglue, silicone elastomer (Kwik-Sil Adhesive, World Precision Instruments, KWIK-SIL), was applied on one side of the split and placed carefully around the wound. 5 to 6 sutures of 6.0 nylon were made carefully to secure the splint. The wound was later covered with Tegaderm dressing (transparent, 3M). Mice awakened from anesthesia using MMF antagonist and later given postoperative analgesia such as Metamizol (500 mg Metamizol/ 250 ml) in drinking water.

35. Cell harvest and sorting

$En1^{Cre}$; $R26^{mTmG}$ or $Adipoq^{Cre}$; $R26^{mTmG}$, Postnatal day 0 or day 1 was used. Dorsal back skin from these mice was used. First, the back skin taken was taken out and washed with

sterile HBSS solution. Later, skin tissue was transferred to a sterile hood and minced into small pieces using surgical steel blades. This was rewashed with HBSS 3X times. Following this was a digestion step. Minced tissue was incubated with 5ml of digestion mix, and a single-cell suspension was made as mentioned above. Sorting was carried out using Aria III cell sorter, and the 100µm nozzle was used for fibroblast and adipocyte sorting. Cells were sorted into polypropylene tubes containing FACS buffer, and a small number of cells were re-analyzed by flow cytometry to check sort purity.

36. Cell transplantation

FACS sorted cells were first thoroughly and gently washed with PBS. Cells were later resuspended in PBS at 5×10^5 cells per ml. An equal volume of ice-cold Matrigel was mixed with the cell suspension (Phenol red-free, Corning, 356231). Cell suspensions in Matrigel were made to a final concentration of 2.5×10^5 cells per ml. This was stored in an ice bucket until intradermal injections. The Rag2 $^{-/-}$ mice, at age 10–12 weeks, received Adipoq GFP+ and En1 GFP+ cells - Matrigel transplants. 5mm diameter excisional wounds (full-thickness, 2 wounds) as described above were made on mice's dorsal back skin. Following this, two 50 µl injections of AdipoqGFP+ cell or En1GFP+ cell suspension prepared in Matrigel at a concentration of 2.5×10^5 cells per ml were made to the left side wound on opposite sides. 2 intradermal injections of 50 µl PBS were made to control wounds on the right side. After injection, the cells were left for 10 minutes, and the silicone splints were placed carefully. The gentle press was applied around the wound, as mentioned above in the splinted wound method. Harvesting of scar tissue was done 7 days post wounding. Lastly, harvested tissue fixation was done at 4 ° C overnight using 2% PFA. After 3 times PBS washing, the tissues were prepared for histological analysis.

37. Statistics

2-way ANOVA with 95% CI, P value<0.0001(****) calculated using GraphPad Prism 8 software and employed all figures.

38. Data availability

Code to reproduce the analyses and figures based on scRNA-seq data generated in this manuscript can be accessed *https://github.com/theislab/2021_Stromal_Fate_Restriction*. Additional information is available from the corresponding author on request.

IV References

1. Bayat A, McGrouther DA, Ferguson MW. Skin scarring. BMJ. 2003 Jan 11;326(7380):88-92. doi: 10.1136/bmj.326.7380.88. PMID: 12521975; PMCID: PMC1125033.

2. Palmieri TL, Petuskey K, Bagley A, Takashiba S, Greenhalgh DG, Rab GT. Alterations in functional movement after axillary burn scar contracture: a motion analysis study. J Burn Care Rehabil. 2003 Mar-Apr;24(2):104-8. doi: 10.1097/01. BCR.0000054170.62555.09. PMID: 12626930.

3. Prasad JK, Bowden ML, Thomson PD. A review of the reconstructive surgery needs of 3167 survivors of burn injury. Burns. 1991 Aug;17(4):302-5. doi: 10.1016/0305-4179(91)90044-h. PMID: 1930664.

4. Sen CK, Gordillo GM, Roy S, Kirsner R, Lambert L, Hunt TK, Gottrup F, Gurtner GC, Longaker MT. Human skin wounds: a major and snowballing threat to public health and the economy. Wound Repair Regen. 2009 Nov-Dec;17(6):763-71. doi: 10.1111/j.1524-475X.2009.00543.x. PMID: 19903300; PMCID: PMC2810192.

5. Sund, B. New developments in wound care. London: PJB Publications, pp.1-255. Clinical Report CBS 836 (2000)

6. Jiang D, Christ S, Correa-Gallegos D, Ramesh P, Kalgudde Gopal S, Wannemacher J, Mayr CH, Lupperger V, Yu Q, Ye H, Mück-Häusl M, Rajendran V, Wan L, Liu J, Mirastschijski U, Volz T, Marr C, Schiller HB, Rinkevich Y. Injury triggers fascia fibroblast collective cell migration to drive scar formation through N-cadherin. Nat Commun. 2020 Nov 6;11(1):5653. doi: 10.1038/s41467-020-19425-1. PMID: 33159076; PMCID: PMC7648088.

7. Bock O, Schmid-Ott G, Malewski P, Mrowietz U. Quality of life of patients with keloid and hypertrophic scarring. Arch Dermatol Res. 2006 Apr;297(10):433-8. doi: 10.1007/s00403-006-0651-7. Epub 2006 Mar 10. PMID: 16528552

8. Van Loey NE, Bremer M, Faber AW, Middelkoop E, Nieuwenhuis MK. Itching following burns: epidemiology and predictors. Br J Dermatol. 2008 Jan;158(1):95-100. doi: 10.1111/j.1365-2133.2007.08278.x. Epub 2007 Nov 6. PMID: 17986307.

9. Bakker A, Maertens KJ, Van Son MJ, Van Loey NE. Psychological consequences of pediatric burns from a child and family perspective: a review of the empirical literature. Clin Psychol Rev. 2013 Apr;33(3):361-71. doi: 10.1016/j.cpr.2012.12.006. Epub 2013 Jan 9. PMID: 23410718.

10. Monstrey S, Middelkoop E, Vranckx JJ, Bassetto F, Ziegler UE, Meaume S, Téot L. Updated scar management practical guidelines: non-invasive and invasive measures. J Plast Reconstr Aesthet Surg. 2014 Aug;67(8):1017-25. doi: 10.1016/j.bjps.2014.04.011. Epub 2014 May 14. PMID: 24888226.

11. Takeo M, Lee W, Ito M. Wound healing, and skin regeneration. Cold Spring Harb Perspect Med. 2015 Jan 5;5(1):a023267. doi: 10.1101/cshperspect. a023267. PMID: 25561722; PMCID: PMC4292081

12. Krafts KP. Tissue repair: The hidden drama. Organogenesis. 2010 Oct-Dec;6(4):225-33. doi: 10.4161/org.6.4.12555. PMID: 21220961; PMCID: PMC3055648

13. Correa-Gallegos D, Jiang D, Christ S, Ramesh P, Ye H, Wannemacher J, Kalgudde Gopal S, Yu Q, Aichler M, Walch A, Mirastschijski U, Volz T, Rinkevich Y. Patch repair of deep wounds by mobilized fascia. Nature. 2019 Dec;576(7786):287-292. doi: 10.1038/s41586-019-1794-y. Epub 2019 Nov 27. PMID: 31776510.

14. Huang TT, Blackwell SJ, Lewis SR. Ten years of experience in managing patients with burn contractures of axilla, elbow, wrist, and knee joints. Plast Reconstr Surg. 1978 Jan;61(1):70-6. doi: 10.1097/00006534-197801000-00012. PMID: 619389.

15. Marshall CD, Hu MS, Leavitt T, Barnes LA, Lorenz HP, Longaker MT. Cutaneous Scarring: Basic Science, Current Treatments, and Future Directions. Adv Wound Care (New Rochelle). 2018 Feb 1;7(2):29-45. doi: 10.1089/wound.2016.0696. PMID: 29392092; PMCID: PMC5792238.

16. Li Q, Zhang C, Fu X. Will stem cells bring hope to pathological skin scar treatment? Cytotherapy. 2016 Aug;18(8):943-956. doi: 10.1016/j.jcyt.2016.05.008. Epub 2016 Jun 9. PMID: 27293205.

17. Rhett JM, Ghatnekar GS, Palatinus JA, O'Quinn M, Yost MJ, Gourdie RG. Novel therapies for scar reduction and regenerative healing of skin wounds. Trends Biotechnol. 2008 Apr;26(4):173-80. doi: 10.1016/j.tibtech.2007.12.007. Epub 2008 Mar 4. PMID: 18295916.

18. "Juvista (Avotermin) in Breast Reduction Surgery Scars - Full Text View - clinicaltrials.gov." https://clinicaltrials.gov/ct2/show/NCT00432328 (last accessed February4, 2016)

19. "A Clinical Study of Allogeneic Human Dermal Fibroblasts for Remodeling Scar Contractures." https://clinicaltrials.gov/ct2/show/study/NCT01564407 (last update, July 11 2017)

20. Galiano RD. An Antisense Oligonucleotide (EXC 001) Targeting Connective Tissue Growth Factor Reduces Skin Scarring Associated with Abdominoplasty and Reduces CTGF Expression. Plast Reconstr Surg 2011;128:1.

21. "A Study to Evaluate the Effectiveness and Safety of RXI 109 on the Outcome of Revised Hypertrophic Scars." https://clinicaltrials.gov/ct2/show/NCT02246465 (last accessed February 23, 2018)

22. Reinke JM, Sorg H. Wound repair and regeneration. Eur Surg Res. 2012;49(1):35-43. doi: 10.1159/000339613. Epub 2012 Jul 11. PMID: 2279771.

23. Negut I, Grumezescu V, Grumezescu AM. Treatment Strategies for Infected Wounds. Molecules. 2018 Sep 18;23(9):2392. doi: 10.3390/molecules23092392. PMID: 30231567; PMCID: PMC6225154.

24. Mellott AJ, Zamierowski DS, Andrews BT. Negative Pressure Wound Therapy in Maxillofacial Applications. Dent J (Basel). 2016 Sep 6;4(3):30. doi: 10.3390/dj4030030. PMID: 29563472; PMCID: PMC5806940.

25. Pinto AM, Cerqueira MA, Bañobre-Lópes M, Pastrana LM, Sillankorva S. Bacteriophages for Chronic Wound Treatment: from Traditional to Novel Delivery Systems. Viruses. 2020 Feb 20;12(2):235. doi: 10.3390/v12020235. PMID: 32093349; PMCID: PMC7077204.

26. Mokos ZB, Jović A, Grgurević L, Dumić-Čule I, Kostović K, Čeović R, Marinović B. Current Therapeutic Approach to Hypertrophic Scars. Front Med (Lausanne). 2017 Jun 20;4:83. doi: 10.3389/fmed.2017.00083. PMID: 28676850; PMCID: PMC5476971.

27. Alster TS, Tanzi EL. Hypertrophic scars and keloids: etiology and management. Am J Clin Dermatol. 2003;4(4):235-43. doi: 10.2165/00128071-200304040-00003. PMID: 12680802.

28. Brissett AE, Sherris DA. Scar contractures, hypertrophic scars, and keloids. Facial Plast Surg. 2001 Nov;17(4):263-72. doi: 10.1055/s-2001-18827. PMID: 11735059.

29. Xue M, Jackson CJ. Extracellular Matrix Reorganization During Wound Healing and Its Impact on Abnormal Scarring. Adv Wound Care (New Rochelle). 2015 Mar 1;4(3):119-136. doi: 10.1089/wound.2013.0485. PMID: 25785236; PMCID: PMC4352699.

30. Juckett G, Hartman-Adams H. Management of keloids and hypertrophic scars. Am Fam Physician. 2009 Aug 1;80(3):253-60. PMID: 19621835.

31. Goldenberg G, Luber AJ. Use of intralesional cryosurgery as an innovative therapy for keloid scars and a review of current treatments. J Clin Aesthet Dermatol. 2013 Jul;6(7):23-6. PMID: 23882311; PMCID: PMC3718752.

32. Har-Shai Y, Mettanes I, Zilberstein Y, Genin O, Spector I, Pines M. Keloid histopathology after intralesional cryosurgery treatment. J Eur Acad Dermatol Venereol. 2011 Sep;25(9):1027-36. doi: 10.1111/j.1468-3083.2010.03911.x. Epub 2010 Nov 25. PMID: 21108665.

33. J. Poston, "The use of silicone gel sheeting in the management of hypertrophic and keloid scars," Journal of Wound Care, vol. 9, no. 1, pp. 10–16, 2000.

34. O'Brien L, Pandit A. Silicon gel sheeting for preventing and treating hypertrophic and keloid scars. Cochrane Database Syst Rev. 2006 Jan 25;(1):CD003826. doi: 10.1002/14651858.CD003826.pub2. Update in: Cochrane Database Syst Rev. 2013;9:CD003826. PMID: 16437463.

35. Waibel JS, Rudnick A. Current trends and future considerations in scar treatment. Semin Cutan Med Surg. 2015 Mar;34(1):13-6. doi: 10.12788/j.sder.2015.0129. PMID: 25922952.

36. Brewin MP, Lister TS. Prevention or treatment of hypertrophic burn scarring: a review of when and how to treat with the pulsed dye laser. Burns. 2014 Aug;40(5):797-804. doi: 10.1016/j.burns.2013.12.017. Epub 2014 Jan 15. PMID: 24439925

37. Gauglitz GG. Management of keloids and hypertrophic scars: current and emerging options. Clin Cosmet Investig Dermatol. 2013 Apr 24;6:103-14. doi: 10.2147/CCID.S35252. PMID: 23637546; PMCID: PMC3639020.

38. Al-Attar A, Mess S, Thomassen JM, Kauffman CL, Davison SP. Keloid pathogenesis and treatment. Plast Reconstr Surg. 2006 Jan;117(1):286-300. doi: 10.1097/01.prs.0000195073.73580.46. PMID: 16404281.

39. Block L, Gosain A, King TW. Emerging Therapies for Scar Prevention. Adv Wound Care (New Rochelle). 2015 Oct 1;4(10):607-614. doi: 10.1089/wound.2015.0646. PMID: 26487979; PMCID: PMC4593896.

40. Zhang DZ, Liu XY, Xiao WL, Xu YX. Botulinum Toxin Type A and the Prevention of Hypertrophic Scars on the Maxillofacial Area and Neck: A Meta-Analysis of Randomized Controlled Trials. PLoS One. 2016 Mar 17;11(3):e0151627. doi: 10.1371/journal.pone.0151627. PMID: 26985661; PMCID: PMC4795777.

41. Scala J, Vojvodic A, Vojvodic P, Vlaskovic-Jovicevic T, Peric-Hajzler Z, Matovic D, Dimitrijevic S, Vojvodic J, Sijan G, Stepic N, Wollina U, Tirant M, Thuong NV, Fioranelli M, Lotti T. Botulin Toxin Use in Scars/Keloids Treatment. Open Access Maced J Med Sci. 2019 Aug 30;7(18):2979-2981. doi: 10.3889/oamjms.2019.783. PMID: 31850103; PMCID: PMC6910812.

42. Wang H, Chen Z, Li XJ, Ma L, Tang YL. Anti-inflammatory cytokine TSG-6 inhibits hypertrophic scar formation in a rabbit ear model. Eur J Pharmacol. 2015 Mar 15;751:42-9. doi: 10.1016/j.ejphar.2015.01.040. Epub 2015 Feb 3. PMID: 25661977.

43. Kwak DH, Bae TH, Kim WS, Kim HK. Anti-Vascular Endothelial Growth Factor (Bevacizumab) Therapy Reduces Hypertrophic Scar Formation in a Rabbit Ear Wounding Model. Arch Plast Surg. 2016 Nov;43(6):491-497. doi: 10.5999/aps.2016.43.6.491. Epub 2016 Nov 18. PMID: 27896177; PMCID: PMC5122535.

44. Wang P, Jiang LZ, Xue B. Recombinant human endostatin reduces hypertrophic scar formation in rabbit ear model through down-regulation of VEGF and TIMP-1. Afr Health Sci. 2016 Jun;16(2):542-53. doi: 10.4314/ahs.v16i2.23. PMID: 27605970; PMCID: PMC4994545.

45. Shirakami E, Yamakawa S, Hayashida K. Strategies to prevent hypertrophic scar formation: a review of therapeutic interventions based on molecular evidence. Burns Trauma. 2020 Jan 27;8:tkz003. doi: 10.1093/burnst/tkz003. PMID: 32341924; PMCID: PMC7175766.

46. Spiekman M, van Dongen JA, Willemsen JC, Hoppe DL, van der Lei B, Harmsen MC. The power of fat and its adipose-derived stromal cells: emerging concepts for fibrotic scar treatment. J Tissue Eng Regen Med. 2017 Nov;11(11):3220-3235. doi: 10.1002/term.2213. Epub 2017 Feb 3. PMID: 28156060; PMCID: PMC5724515.

47. Baker R, Urso-Baiarda F, Linge C, Grobbelaar A. Cutaneous scarring: a clinical review. Dermatol Res Pract. 2009;2009:625376. doi: 10.1155/2009/625376. Epub 2010 Feb 10. PMID: 20585482; PMCID: PMC2879602.

48. Blacklow NR, Hoggan MD, Rowe WP. Immunofluorescent studies of the potentiation of an adenovirus-associated virus by adenovirus 7. J Exp Med. 1967 May 1;125(5):755-65. doi: 10.1084/jem.125.5.755. PMID: 4225814; PMCID: PMC2138211.

49. Muzyczka N. Use of adeno-associated virus as a general transduction vector for mammalian cells. Curr Top Microbiol Immunol. 1992;158:97-129. doi:10.1007/978-3-642-75608-5_5

50. Zhong L, Chen L, Li Y, Qing K, Weigel-Kelley KA, Chan RJ, Yoder MC, Srivastava A. Self-complementary adeno-associated virus 2 (AAV)-T cell protein tyrosine phosphatase vectors as helper viruses to improve transduction efficiency of conventional single-stranded AAV vectors in vitro and in vivo. Mol Ther. 2004 Nov;10(5):950-7. doi: 10.1016/j.ymthe.2004.07.018. PMID: 15509512.

51. Jayandharan GR, Zhong L, Sack BK, Rivers AE, Li M, Li B, Herzog RW, Srivastava A. Optimized adeno-associated virus (AAV)-protein phosphatase-5 helper viruses for efficient liver transduction by single-stranded AAV vectors: therapeutic expression of factor IX at reduced vector doses. Hum Gene Ther. 2010 Mar;21(3):271-83. doi: 10.1089/hum.2009.100. PMID: 19788390; PMCID: PMC2865358.

52. Grieger JC, Samulski RJ. Adeno-associated virus as a gene therapy vector: vector development, production and clinical applications. Adv Biochem Eng Biotechnol. 2005;99:119-145.

53. Berns KI. Parvovirus replication. Microbiol Rev. 1990 Sep;54(3):316-29. PMID: 2215424; PMCID: PMC372780

54. Zincarelli C, Soltys S, Rengo G, Rabinowitz JE. Analysis of AAV serotypes 1-9 mediated gene expression and tropism in mice after systemic injection. Mol Ther. 2008 Jun;16(6):1073-80. doi: 10.1038/mt.2008.76. Epub 2008 Apr 15. PMID: 18414476.

55. Naso MF, Tomkowicz B, Perry WL 3rd, Strohl WR. Adeno-Associated Virus (AAV) as a Vector for Gene Therapy. BioDrugs. 2017 Aug;31(4):317-334. doi: 10.1007/s40259-017-0234-5. PMID: 28669112; PMCID: PMC5548848.

56. Smits JPH, Niehues H, Rikken G, van Vlijmen-Willems IMJJ, van de Zande GWHJF, Zeeuwen PLJM, Schalkwijk J, van den Bogaard EH. Immortalized N/TERT keratinocytes as an alternative cell source in 3D human epidermal models. Sci Rep. 2017 Sep 19;7(1):11838. doi: 10.1038/s41598-017-12041-y. PMID: 28928444; PMCID: PMC5605545.

57. Liang CC, Park AY, Guan JL. In vitro scratch assay: a convenient and inexpensive method for analysis of cell migration in vitro. Nat Protoc. 2007;2(2):329-33. doi: 10.1038/nprot.2007.30. PMID: 17406593.

58. Seo BF, Lee JY, Jung SN. Models of abnormal scarring. Biomed Res Int. 2013;2013:423147. doi: 10.1155/2013/423147. Epub 2013 Sep 3. PMID: 24078916; PMCID: PMC3775400.

59. Jackson EL, Lu H. Three-dimensional models for studying development and disease: moving on from organisms to organs-on-a-chip and organoids. Integr Biol (Camb). 2016 Jun 13;8(6):672-83. doi: 10.1039/c6ib00039h. Epub 2016 May 9. PMID: 27156572; PMCID: PMC4905804.

60. Hoarau-Véchot J, Rafii A, Touboul C, Pasquier J. Halfway between 2D and Animal Models: Are 3D Cultures the Ideal Tool to Study Cancer-Microenvironment Interactions? Int J Mol Sci. 2018 Jan 18;19(1):181. doi: 10.3390/ijms19010181. PMID: 29346265; PMCID: PMC5796130.

61. Mendoza-Garcia J, Sebastian A, Alonso-Rasgado T, Bayat A. Optimization of an ex vivo wound healing model in the adult human skin: Functional evaluation using photodynamic therapy. Wound Repair Regen. 2015 Sep;23(5):685-702. doi: 10.1111/wrr.12325. Epub 2015 Sep 8. PMID: 26094764.

62. Xu W, Jong Hong S, Jia S, Zhao Y, Galiano RD, Mustoe TA. Application of a partial-thickness human ex vivo skin culture model in cutaneous wound healing study. Lab Invest. 2012 Apr;92(4):584-99. doi: 10.1038/labinvest.2011.184. Epub 2012 Jan 9. PMID: 22231737.

63. Corzo-León DE, Munro CA, MacCallum DM. An ex vivo Human Skin Model to Study Superficial Fungal Infections. Front Microbiol. 2019 Jun 5;10:1172. doi: 10.3389/fmicb.2019.01172. PMID: 31231322; PMCID: PMC6560176.

64. Géniès C, Jamin EL, Debrauwer L, Zalko D, Person EN, Eilstein J, Grégoire S, Schepky A, Lange D, Ellison C, Roe A, Salhi S, Cubberley R, Hewitt NJ, Rothe H, Klaric M, Duplan H, Jacques-Jamin C. Comparison of the metabolism of 10 chemicals in human and pig skin explants. J Appl Toxicol. 2019 Feb;39(2):385-397. doi: 10.1002/jat.3730. Epub 2018 Oct 21. PMID: 30345528; PMCID: PMC6587507.

65. Alves DR, Booth SP, Scavone P, Schellenberger P, Salvage J, Dedi C, Thet NT, Jenkins ATA, Waters R, Ng KW, Overall ADJ, Metcalfe AD, Nzakizwanayo J, Jones BV. Development of a High-Throughput ex-Vivo Burn Wound Model Using Porcine Skin, and Its Application to Evaluate New Approaches to Control Wound Infection. Front Cell Infect Microbiol. 2018 Jun 15;8:196. doi: 10.3389/fcimb.2018.00196. PMID: 29963501; PMCID: PMC6013584.

66. Ng KW, Pearton M, Coulman S, Anstey A, Gateley C, Morrissey A, Allender C, Birchall J. Development of an ex vivo human skin model for intradermal vaccination: tissue viability and Langerhans cell behaviour. Vaccine. 2009 Oct 9;27(43):5948-55. doi: 10.1016/j.vaccine.2009.07.088. Epub 2009 Aug 11. PMID: 19679220; PMCID: PMC2753709.

67. Syed F, Bagabir RA, Paus R, Bayat A. Ex vivo evaluation of antifibrotic compounds in skin scarring: EGCG and silencing of PAI-1 independently inhibit growth and induce keloid shrinkage. Lab Invest. 2013 Aug;93(8):946-60. doi: 10.1038/labinvest.2013.82. Epub 2013 Jul 8. PMID: 23835737.

68. Neil JE, Brown MB, Williams AC. Human skin explant model for the investigation of topical therapeutics. Sci Rep. 2020 Dec 3;10(1):21192. doi: 10.1038/s41598-020-78292-4. PMID: 33273665; PMCID: PMC7712775.

69. Kendall AC, Kiezel-Tsugunova M, Brownbridge LC, Harwood JL, Nicolaou A. Lipid functions in skin: Differential effects of n-3 polyunsaturated fatty acids on cutaneous ceramides, in a human skin organ culture model. Biochim Biophys Acta Biomembr. 2017 Sep;1859(9 Pt B):1679-1689. doi: 10.1016/j.bbamem.2017.03.016. Epub 2017 Mar 21. PMID: 28341437; PMCID: PMC5504780.

70. Faway É, Cambier L, Mignon B, Poumay Y, Lambert de Rouvroit C. Modeling dermatophytosis in reconstructed human epidermis: A new tool to study infection mechanisms and to test antifungal agents. Med Mycol. 2017 Jul 1;55(5):485-494. doi: 10.1093/mmy/myw111. PMID: 27760830

71. Attia-Vigneau J, Terryn C, Lorimier S, Sandre J, Antonicelli F, Hornebeck W. Regeneration of human dermis by a multi-headed peptide. J Invest Dermatol. 2014 Jan;134(1):58-67. doi: 10.1038/jid.2013.290. Epub 2013 Jun 28. PMID: 23812301.

72. Maboni G, Davenport R, Sessford K, Baiker K, Jensen TK, Blanchard AM, Wattegedera S, Entrican G, Tötemeyer S. A Novel 3D Skin Explant Model to Study Anaerobic Bacterial Infection. Front Cell Infect Microbiol. 2017 Sep 14;7:404. doi: 10.3389/fcimb.2017.00404. PMID: 28959685; PMCID: PMC5604072.

73. Burd DA, Longaker MT, Adzick NS, Compton CC, Harrison MR, Siebert JW, Ehrlich HP. Fetal wound healing: an in vitro explant model. J Pediatr Surg. 1990 Aug;25(8):898-901. doi: 10.1016/0022-3468(90)90199-j. PMID: 2401945.

74. Moll I, Houdek P, Schmidt H, Moll R. Characterization of epidermal wound healing in a human skin organ culture model: acceleration by transplanted keratinocytes. J Invest Dermatol. 1998 Aug;111(2):251-8. doi: 10.1046/j.1523-1747.1998.00265.x. PMID: 9699726.

75. Forsberg S, Rollman O. Re-epithelialization from human skin explant cultures is promoted by ligand-activated HER3 receptor. J Dermatol Sci. 2010 Jul;59(1):7-15. doi: 10.1016/j.jdermsci.2010.03.017. Epub 2010 Apr 3. PMID: 20537867

76. Stoll SW, Kansra S, Elder JT. Keratinocyte outgrowth from human skin explant cultures is dependent upon p38 signaling. Wound Repair Regen. 2003 Sep-Oct;11(5):346-53. doi: 10.1046/j.1524-475x.2003.11506.x. PMID: 12950638

77. Lu H, Rollman O. Fluorescence imaging of reepithelialization from skin explant cultures on acellular dermis. Wound Repair Regen. 2004 Sep-Oct;12(5):575-86. doi: 10.1111/j.1067-1927.2004.012510.x. PMID: 15453840

78. Mazzalupo S, Wawersik MJ, Coulombe PA. An ex vivo assay to assess the potential of skin keratinocytes for wound epithelialization. J Invest Dermatol. 2002 May;118(5):866-70. doi: 10.1046/j.1523-1747.2002.01736.x. PMID: 11982766.

79. Frade MA, Andrade TA, Aguiar AF, Guedes FA, Leite MN, Passos WR, Coelho EB, Das PK. Prolonged viability of human organotypic skin explant in culture method (hOSEC). An Bras Dermatol. 2015 May-Jun;90(3):347-50. doi: 10.1590/abd1806-4841.20153645. Epub 2015 Jun 1. PMID: 26131864; PMCID: PMC4516099.

80. Peramo A, Marcelo CL. Visible effects of rapamycin (sirolimus) on human skin explants in vitro. Arch Dermatol Res. 2013 Mar;305(2):163-71. doi: 10.1007/s00403-012-1288-3. Epub 2012 Sep 8. PMID: 22960739.

81. Gothelf A, Gehl J. Gene electrotransfer to skin; review of existing literature and clinical perspectives. Curr Gene Ther. 2010 Aug;10(4):287-99. doi: 10.2174/156652310791823443. PMID: 20557284.

82. Gothelf A, Gehl J. Electroporation-based DNA delivery technology: methods for gene electrotransfer to skin. Methods Mol Biol. 2014;1143:115-22. doi: 10.1007/978-1-4939-0410-5_7. PMID: 24715284.

83. Amante DH, Smith TR, Mendoza JM, Schultheis K, McCoy JR, Khan AS, Sardesai NY, Broderick KE. Skin Transfection Patterns and Expression Kinetics of Electroporation-Enhanced Plasmid Delivery Using the CELLECTRA-3P, a Portable Next-Generation Dermal Electroporation Device. Hum Gene Ther Methods. 2015 Aug;26(4):134-46. doi: 10.1089/hgtb.2015.020. PMID: 26222896; PMCID: PMC5206769.

84. Broderick KE, Chan A, Lin F, Shen X, Kichaev G, Khan AS, Aubin J, Zimmermann TS, Sardesai NY. Optimized in vivo transfer of small interfering RNA targeting dermal tissue using in vivo surface electroporation. Mol Ther Nucleic Acids. 2012 Feb 14;1(2):e11. doi: 10.1038/mtna.2012.1. PMID: 23344722; PMCID: PMC3381603.

85. Fernandes IR, Russo FB, Pignatari GC, Evangelinellis MM, Tavolari S, Muotri AR, Beltrão-Braga PC. Fibroblast sources: Where can we get them? Cytotechnology. 2016 Mar;68(2):223-8. doi: 10.1007/s10616-014-9771-7. Epub 2014 Jul 25. PMID: 25060709; PMCID: PMC4754245.

86. Jiang D, Correa-Gallegos D, Christ S, Stefanska A, Liu J, Ramesh P, Rajendran V, De Santis MM, Wagner DE, Rinkevich Y. Two succeeding fibroblastic lineages drive dermal development and the transition from regeneration to scarring. Nat Cell Biol. 2018 Apr;20(4):422-431. doi: 10.1038/s41556-018-0073-8. Epub 2018 Mar 28. PMID: 29593327.

87. Rinkevich Y, Walmsley GG, Hu MS, Maan ZN, Newman AM, Drukker M, Januszyk M, Krampitz GW, Gurtner GC, Lorenz HP, Weissman IL, Longaker MT. Skin fibrosis. Identification and isolation of a dermal lineage with intrinsic fibrogenic potential. Science. 2015 Apr 17;348(6232):aaa2151. doi: 10.1126/science.aaa2151. PMID: 25883361; PMCID: PMC5088503.

88. Hinz B, Phan SH, Thannickal VJ, Prunotto M, Desmoulière A, Varga J, De Wever O, Mareel M, Gabbiani G. Recent developments in myofibroblast biology: paradigms for connective tissue remodeling. Am J Pathol. 2012 Apr;180(4):1340-55. doi: 10.1016/j.ajpath.2012.02.004. Epub 2012 Mar 2. PMID: 22387320; PMCID: PMC3640252.

89. Spickard EA, Joshi PM, Rothman JH. The multipotency-to-commitment transition in Caenorhabditis elegans-implications for reprogramming from cells to organs. FEBS Lett. 2018 Mar;592(6):838-851. doi: 10.1002/1873-3468.12977. Epub 2018 Feb 1. PMID: 29334121; PMCID: PMC6385892.

90. Merrell AJ, Stanger BZ. Adult cell plasticity in vivo: dedifferentiation and transdifferentiation are back in style. Nat Rev Mol Cell Biol. 2016 Jul;17(7):413-25. doi: 10.1038/nrm.2016.24. Epub 2016 Mar 16. PMID: 26979497; PMCID: PMC5818993.

91. Desai VD, Hsia HC, Schwarzbauer JE. Reversible modulation of myofibroblast differentiation in adipose-derived mesenchymal stem cells. PLoS One. 2014 Jan 23;9(1):e86865. doi: 10.1371/journal.pone.0086865. PMID: 24466271; PMCID: PMC3900664.

92. Giordano A, Smorlesi A, Frontini A, Barbatelli G, Cinti S. White, brown and pink adipocytes: the extraordinary plasticity of the adipose organ. Eur J Endocrinol. 2014 Apr 10;170(5):R159-71. doi: 10.1530/EJE-13-0945. PMID: 24468979.

93. Guerrero-Juarez CF, Dedhia PH, Jin S, Ruiz-Vega R, Ma D, Liu Y, Yamaga K, Shestova O, Gay DL, Yang Z, Kessenbrock K, Nie Q, Pear WS, Cotsarelis G, Plikus MV. Single-cell analysis reveals fibroblast heterogeneity and myeloid-derived adipocyte progenitors in murine skin wounds. Nat Commun. 2019 Feb 8;10(1):650. doi: 10.1038/s41467-018-08247-x. PMID: 30737373; PMCID: PMC6368572.

94. Marangoni RG, Korman BD, Wei J, Wood TA, Graham LV, Whitfield ML, Scherer PE, Tourtellotte WG, Varga J. Myofibroblasts in murine cutaneous fibrosis originate from adiponectin-positive intradermal progenitors. Arthritis Rheumatol. 2015 Apr;67(4):1062-73. doi: 10.1002/art.38990. PubMed: 25504959.

95. Plikus MV, Guerrero-Juarez CF, Ito M, Li YR, Dedhia PH, Zheng Y, Shao M, Gay DL, Ramos R, Hsi TC, Oh JW, Wang X, Ramirez A, Konopelski SE, Elzein A, Wang A, Supapannachart RJ, Lee HL, Lim CH, Nace A, Guo A, Treffeisen E, Andl T, Ramirez RN, Murad R, Offermanns S, Metzger D, Chambon P, Widgerow AD, Tuan TL, Mortazavi A, Gupta RK, Hamilton BA, Millar SE, Seale P, Pear WS, Lazar MA, Cotsarelis G. Regeneration of fat cells from myofibroblasts during wound healing. Science. 2017 Feb 17;355(6326):748-752. doi: 10.1126/science.aai8792. Epub 2017 Jan 5. PMID: 28059714; PMCID: PMC5464786.

96. Schmidt BA, Horsley V. Intradermal adipocytes mediate fibroblast recruitment during skin wound healing. Development. 2013 Apr;140(7):1517-27. doi: 10.1242/dev.087593. PMID: 23482487; PMCID: PMC3596993.

97. Shook BA, Wasko RR, Rivera-Gonzalez GC, Salazar-Gatzimas E, López-Giráldez F, Dash BC, Muñoz-Rojas AR, Aultman KD, Zwick RK, Lei V, Arbiser JL, Miller-Jensen K, Clark DA, Hsia HC, Horsley V. Myofibroblast proliferation and heterogeneity are supported by macrophages during skin repair. Science. 2018 Nov 23;362(6417). pii: eaar2971. doi:10.1126/science. aar2971. PubMed: 30467144.

98. Shook BA, Wasko RR, Mano O, Rutenberg-Schoenberg M, Rudolph MC, Zirak B, Rivera-Gonzalez GC, López-Giráldez F, Zarini S, Rezza A, Clark DA, Rendl M, Rosenblum MD, Gerstein MB, Horsley V. Dermal Adipocyte Lipolysis and Myofibroblast Conversion Are Required for Efficient Skin Repair. Cell Stem Cell. 2020 Jun 4;26(6):880-895.e6. doi: 10.1016/j.stem.2020.03.013. Epub 2020 Apr 16. PMID: 32302523; PMCID: PMC7853423.

99. Zhang Z, Shao M, Hepler C, Zi Z, Zhao S, An YA, Zhu Y, Ghaben AL, Wang MY, Li N, Onodera T, Joffin N, Crewe C, Zhu Q, Vishvanath L, Kumar A, Xing C, Wang QA, Gautron

L, Deng Y, Gordillo R, Kruglikov I, Kusminski CM, Gupta RK, Scherer PE. Dermal adipose tissue has high plasticity and undergoes reversible dedifferentiation in mice. J Clin Invest. 2019 Dec 2;129(12):5327-5342. doi:10.1172/JCI130239. PubMed: 31503545.

100. Ban CR, Twigg SM. Fibrosis in diabetes complications: pathogenic mechanisms and circulating and urinary markers. Vasc Health Risk Manag. 2008;4(3):575-96. doi: 10.2147/vhrm.s1991. PMID: 18827908; PMCID: PMC2515418.

101. Adigun R, Goyal A, Bansal P, Hariz A. Systemic Sclerosis. 2020 Aug 28. In: StatPearls [Internet]. Treasure Island (FL): StatPearls Publishing; 2021 Jan–. PMID: 28613625.

102. Buras ED, Converso-Baran K, Davis CS, Akama T, Hikage F, Michele DE, Brooks SV, Chun TH. Fibro-Adipogenic Remodeling of the Diaphragm in Obesity-Associated Respiratory Dysfunction. Diabetes. 2019 Jan;68(1):45-56. doi: 10.2337/db18-0209. Epub 2018 Oct 25. PMID: 30361289; PMCID: PMC6302533.

103. Contreras O, Cruz-Soca M, Theret M, Soliman H, Tung LW, Groppa E, Rossi FM, Brandan E. Cross-talk between TGF-β and PDGFRα signaling pathways regulates the fate of stromal fibro-adipogenic progenitors. J Cell Sci. 2019 Oct 9;132(19):jcs232157. doi: 10.1242/jcs.232157. PMID: 31434718.

104. Mahmoudi S, Mancini E, Xu L, Moore A, Jahanbani F, Hebestreit K, Srinivasan R, Li X, Devarajan K, Prélot L, Ang CE, Shibuya Y, Benayoun BA, Chang ALS, Wernig M, Wysocka J, Longaker MT, Snyder MP, Brunet A. Heterogeneity in old fibroblasts is linked to variability in reprogramming and wound healing. Nature. 2019 Oct;574(7779):553-558. doi: 10.1038/s41586-019-1658-5. Epub 2019 Oct 23. PMID: 31645721; PMCID: PMC7253295.

105. Tchkonia T, Morbeck DE, Von Zglinicki T, Van Deursen J, Lustgarten J, Scrable H, Khosla S, Jensen MD, Kirkland JL. Fat tissue, aging, and cellular senescence. Aging Cell. 2010 Oct;9(5):667-84. doi: 10.1111/j.1474-9726.2010.00608.x. Epub 2010 Aug 15. PMID: 20701600; PMCID: PMC2941545.

106. Jopling C, Boue S, Izpisua Belmonte JC. Dedifferentiation, transdifferentiation and reprogramming: three routes to regeneration. Nat Rev Mol Cell Biol. 2011 Feb;12(2):79-89. doi: 10.1038/nrm3043. PMID: 21252997.

107. Johansson CB, Youssef S, Koleckar K, Holbrook C, Doyonnas R, Corbel SY, Steinman L, Rossi FM, Blau HM. Extensive fusion of haematopoietic cells with Purkinje neurons in response to chronic inflammation. Nat Cell Biol. 2008 May;10(5):575-83. doi: 10.1038/ncb1720. Epub 2008 Apr 20. PMID: 18425116; PMCID: PMC4230437

108. Blasi A, Martino C, Balducci L, Saldarelli M, Soleti A, Navone SE, Canzi L, Cristini S, Invernici G, Parati EA, Alessandri G. Dermal fibroblasts display similar phenotypic and differentiation capacity to fat-derived mesenchymal stem cells, but differ in anti-inflammatory and angiogenic potential. Vasc Cell. 2011 Feb 8;3(1):5. doi: 10.1186/2045-824X-3-5. PMID: 21349162; PMCID: PMC3044104.

109. G. Invernici, E. A. Parati, G. Alessandri, Dermal fibroblasts display similar phenotypic and differentiation capacity to fat-derived mesenchymal stem cells, but differ in anti-inflammatory and angiogenic potential. Vasc Cell 3, 5 (Feb 8, 2011).

110. Denu RA, Nemcek S, Bloom DD, Goodrich AD, Kim J, Mosher DF, Hematti P. Fibroblasts and Mesenchymal Stromal/Stem Cells Are Phenotypically Indistinguishable. Acta Haematol. 2016;136(2):85-97. doi: 10.1159/000445096. Epub 2016 May 18. PMID: 27188909; PMCID: PMC4988914.

111. Wagers AJ, Weissman IL. Plasticity of adult stem cells. Cell. 2004 Mar 5;116(5):639-48. doi: 10.1016/s0092-8674(04)00208-9. PMID: 15006347.

112. Straub LG, Scherer PE. Metabolic Messengers: Adiponectin. Nat Metab. 2019 Mar;1(3):334-339. doi: 10.1038/s42255-019-0041-z. Epub 2019 Mar 14. PMID: 32661510; PMCID: PMC7357716.

113. Bagnoli JW, Ziegenhain C, Janjic A, Wange LE, Vieth B, Parekh S, Geuder J, Hellmann I, Enard W. Sensitive and powerful single-cell RNA sequencing using mcSCRB-seq. Nat Commun. 2018 Jul 26;9(1):2937. doi: 10.1038/s41467-018-05347-6.PubMed: 30050112.

114. Parekh S, Ziegenhain C, Vieth B, Enard W, Hellmann I. zUMIs - A fast and flexible pipeline to process RNA sequencing data with UMIs. Gigascience. 2018 Jun 1;7(6). doi: 10.1093/gigascience/giy059. PubMed: 29846586.

115. Dobin A, Davis CA, Schlesinger F, Drenkow J, Zaleski C, Jha S, Batut P, Chaisson M, Gingeras TR. STAR: ultrafast universal RNA-seq aligner. Bioinformatics. 2013 Jan 1;29(1):15-21. doi: 10.1093/bioinformatics/bts635. Epub 2012 Oct 25. PubMed: 23104886.

116. auf dem Keller U, Kümin A, Braun S, Werner S. Reactive oxygen species and their detoxification in healing skin wounds. J Investig Dermatol Symp Proc. 2006 Sep;11(1):106-11. doi: 10.1038/sj.jidsymp.5650001. PMID: 17069017.

117. Townsend LK, Weber AJ, Barbeau PA, Holloway GP, Wright DC. Reactive oxygen species-dependent regulation of pyruvate dehydrogenase kinase-4 in white adipose tissue. Am J Physiol Cell Physiol. 2020 Jan 1;318(1):C137-C149. doi: 10.1152/ajpcell.00313.2019. Epub 2019 Nov 13. PMID: 31721616; PMCID: PMC6985839.

118. Fan Y, Zhang G, Vong CT, Ye RD. Serum amyloid A3 confers protection against acute lung injury in Pseudomonas aeruginosa-infected mice. Am J Physiol Lung Cell Mol Physiol. 2020 Feb 1;318(2):L314-L322. doi: 10.1152/ajplung.00309.2019. Epub 2019 Dec 18. PMID: 31851532.

119. Nguyen XX, Muhammad L, Nietert PJ, Feghali-Bostwick C. IGFBP-5 Promotes Fibrosis via Increasing Its Own Expression and That of Other Pro-fibrotic Mediators. Front Endocrinol (Lausanne). 2018 Oct 15;9:601. doi: 10.3389/fendo.2018.00601. PMID: 30374330; PMCID: PMC6196226.

120. Liu Z, Cao Y, Liu G, Yin S, Ma J, Liu J, Zhang M, Wang Y. p75 neurotrophin receptor regulates NGF-induced myofibroblast differentiation and collagen synthesis through MRTF-A. Exp Cell Res. 2019 Oct 1;383(1):111504. doi: 10.1016/j.yexcr.2019.111504. Epub 2019 Jul 17. PMID: 31325438.

121. Palazzo E, Marconi A, Truzzi F, Dallaglio K, Petrachi T, Humbert P, Schnebert S, Perrier E, Dumas M, Pincelli C. Role of neurotrophins on dermal fibroblast survival and differentiation. J Cell Physiol. 2012 Mar;227(3):1017-25. doi: 10.1002/jcp.22811. PMID: 21503896.

122. Gubern A, Barceló-Torns M, Casas J, Barneda D, Masgrau R, Picatoste F, Balsinde J, Balboa MA, Claro E. Lipid droplet biogenesis induced by stress involves triacylglycerol synthesis that depends on group VIA phospholipase A2. J Biol Chem. 2009 Feb 27;284(9):5697-708. doi: 10.1074/jbc.M806173200. Epub 2008 Dec 30. PMID: 19117952.

123. Cabodevilla AG, Sánchez-Caballero L, Nintou E, Boiadjieva VG, Picatoste F, Gubern A, Claro E. Cell survival during complete nutrient deprivation depends on lipid droplet-fueled β-oxidation of fatty acids. J Biol Chem. 2013 Sep 27;288(39):27777-88. doi: 10.1074/jbc.M113.466656. Epub 2013 Aug 12. PMID: 23940052; PMCID: PMC3784694.

124. Boren J, Brindle KM. Apoptosis-induced mitochondrial dysfunction causes cytoplasmic lipid droplet formation. Cell Death Differ. 2012 Sep;19(9):1561-70. doi: 10.1038/cdd.2012.34. Epub 2012 Mar 30. PMID: 22460322; PMCID: PMC3422477.

125. Bensaad K, Favaro E, Lewis CA, Peck B, Lord S, Collins JM, Pinnick KE, Wigfield S, Buffa FM, Li JL, Zhang Q, Wakelam MJO, Karpe F, Schulze A, Harris AL. Fatty acid uptake and lipid storage induced by HIF-1α contribute to cell growth and survival after hypoxia-reoxygenation. Cell Rep. 2014 Oct 9;9(1):349-365. doi: 10.1016/j.celrep.2014.08.056. Epub 2014 Sep 25. PMID: 25263561.

126. Yang ZK, Niu YF, Ma YH, Xue J, Zhang MH, Yang WD, Liu JS, Lu SH, Guan Y, Li HY. Molecular and cellular mechanisms of neutral lipid accumulation in diatom following nitrogen deprivation. Biotechnol Biofuels. 2013 May 4;6(1):67. doi: 10.1186/1754-6834-6-67. PMID: 23642220; PMCID: PMC3662598.

127. Xue M, Jackson CJ. Extracellular Matrix Reorganization During Wound Healing and Its Impact on Abnormal Scarring. Adv Wound Care (New Rochelle). 2015 Mar 1;4(3):119-136. Review. PubMed: 25785236

128. Gabbiani G, Ryan GB, Majne G. Presence of modified fibroblasts in granulation tissue and their possible role in wound contraction. Experientia. 1971 May 15;27(5):549-50. doi: 10.1007/BF02147594. PMID: 5132594.

129. Nagamoto T, Eguchi G, Beebe DC. Alpha-smooth muscle actin expression in cultured lens epithelial cells. Invest Ophthalmol Vis Sci. 2000 Apr;41(5):1122-9. PMID: 10752950.

130. Blobe GC, Schiemann WP, Lodish HF. Role of transforming growth factor beta in human disease. N Engl J Med. 2000 May 4;342(18):1350-8. doi: 10.1056/NEJM200005043421807. PMID: 10793168.

131. Krastev TK, Schop SJ, Hommes J, Piatkowski A, van der Hulst RRWJ. Autologous fat transfer to treat fibrosis and scar-related conditions: A systematic review and meta-analysis. J Plast Reconstr Aesthet Surg. 2020 Nov;73(11):2033-2048. doi: 10.1016/j.bjps.2020.08.023. Epub 2020 Aug 20. PMID: 32948494

132. 40. Hao H, Bian H, Bu X, Zhang S, Zhang P, Yu J, Lai X, Li D, Zhu C, Yao L, Su J. Targeting of Discoidin Domain Receptor 2 (DDR2) Prevents Myofibroblast Activation and Neovessel Formation During Pulmonary Fibrosis. Mol Ther. 2016 Oct;24(10):1734-1744. doi: 10.1038/mt.2016.109. Epub 2016 May 27. PMID: 27350126; PMCID: PMC5112036.

133. 41. Hsia LT, Ashley N, Ouaret D, Wang LM, Wilding J, Bodmer WF. Myofibroblasts are distinguished from activated skin fibroblasts by the expression of AOC3 and other associated markers. Proc Natl Acad Sci U S A. 2016 Apr 12;113(15):E2162-71. doi: 10.1073/pnas.1603534113. Epub 2016 Mar 28. PMID:27036009

134. Bielczyk-Maczynska E. White Adipocyte Plasticity in Physiology and Disease.Cells. 2019 Nov 25;8(12). pii: E1507. doi: 10.3390/cells8121507. Review. PubMed: 31775295

135. Sun KH, Chang Y, Reed NI, Sheppard D. α-Smooth muscle actin is an inconsistent marker of fibroblasts responsible for force-dependent TGFβ activation or collagen production across multiple models of organ fibrosis. Am J Physiol Lung Cell Mol Physiol. 2016 May 1;310(9):L824-36. doi: 10.1152/ajplung.00350.2015. Epub 2016 Mar 4. PMID: 2694408

136. Wynn TA. Cellular and molecular mechanisms of fibrosis. J Pathol. 2008 Jan;214(2):199-210. Review.PMID:18161745

137. 47. Carthy JM. TGFβ signaling and the control of myofibroblast differentiation: Implications for chronic inflammatory disorders. J Cell Physiol. 2018 Jan;233(1):98-106. doi: 10.1002/jcp.25879. Epub 2017 May 15. Review.PMID:28247933

138. Marangoni RG, Masui Y, Fang F, Korman B, Lord G, Lee J, Lakota K, Wei J, Scherer PE, Otvos L, Yamauchi T, Kubota N, Kadowaki T, Asano Y, Sato S, Tourtellotte WG, Varga J. Adiponectin is an endogenous anti-fibrotic mediator and therapeutic target. Sci Rep. 2017 Jun 30;7(1):4397. doi: 10.1038/s41598-017-04162-1. PMID: 28667272; PMCID: PMC5493638.

139. Simonacci F, Bertozzi N, Grieco MP, Grignaffini E, Raposio E. Procedure, applications, and outcomes of autologous fat grafting. Ann Med Surg (Lond). 2017 Jun 27;20:49-60. doi: 10.1016/j.amsu.2017.06.059. PMID: 28702187; PMCID: PMC5491488.

140. Pellegrinelli V, Carobbio S, Vidal-Puig A. Adipose tissue plasticity: how fat depots respond differently to pathophysiological cues. Diabetologia. 2016 Jun;59(6):1075-88. doi: 10.1007/s00125-016-3933-4. Epub 2016 Apr 4. PMID: 27039901; PMCID: PMC4861754.

141. Seale P, Conroe HM, Estall J, Kajimura S, Frontini A, Ishibashi J, Cohen P, Cinti S, Spiegelman BM. Prdm16 determines the thermogenic program of subcutaneous white adipose tissue in mice. J Clin Invest. 2011 Jan;121(1):96-105. doi: 10.1172/JCI44271. Epub 2010 Dec 1. PMID: 21123942; PMCID: PMC3007155.

142. Rosenwald M, Perdikari A, Rülicke T, Wolfrum C. Bi-directional interconversion of brite and white adipocytes. Nat Cell Biol. 2013 Jun;15(6):659-67. doi: 10.1038/ncb2740. Epub 2013 Apr 28. PMID: 23624403.

143. Bochet L, Lehuédé C, Dauvillier S, Wang YY, Dirat B, Laurent V, Dray C, Guiet R, Maridonneau-Parini I, Le Gonidec S, Couderc B, Escourrou G, Valet P, Muller C. Adipocyte-

derived fibroblasts promote tumor progression and contribute to the desmoplastic reaction in breast cancer. Cancer Res. 2013 Sep 15;73(18):5657-68. doi: 10.1158/0008-5472.CAN-13-0530. Epub 2013 Jul 31. PMID: 23903958.

144. Tabit CJ, Slack GC, Fan K, Wan DC, Bradley JP. Fat grafting versus adipose-derived stem cell therapy: distinguishing indications, techniques, and outcomes. Aesthetic Plast Surg. 2012 Jun;36(3):704-13. doi: 10.1007/s00266-011-9835-4. Epub 2011 Nov 9. PMID: 22069062.

145. F. A. Wolf, P. Angerer, F. J. Theis, SCANPY: large-scale single-cell gene expression data analysis. Genome Biol 19, 15 (Feb 6, 2018).

146. A. T. Lun, D. J. McCarthy, J. C. Marioni, A step-by-step workflow for low-level analysis of single-cell RNA-seq data with Bioconductor. F1000Res 5, 2122 (2016).

147. D. V. Klopfenstein, L. Zhang, B. S. Pedersen, F. Ramirez, A. Warwick Vesztrocy, A. Naldi, C. J. Mungall, J. M. Yunes, O. Botvinnik, M. Weigel, W. Dampier, C. Dessimoz, P. Flick, H. Tang, GOATOOLS: A Python library for Gene Ontology analyses. Sci Rep 8, 10872 (Jul 18, 2018).

148. N. R. Bonenfant, D. Sokocevic, D. E. Wagner, Z. D. Borg, M. J. Lathrop, Y. W. Lam, B. Deng, M. J. Desarno, T. Ashikaga, R. Loi, D. J. Weiss, The effects of storage and sterilization on de-cellularized and re-cellularized whole lung. Biomaterials 34, 3231-3245 (Apr, 2013).

149. J. L. van der Velden, D. E. Wagner, K. G. Lahue, S. T. Abdalla, Y. W. Lam, D. J. Weiss, Y. M. W. Janssen-Heininger, TGF-beta1-induced deposition of provisional extracellular matrix by tracheal basal cells promotes epithelial-to-mesenchymal transition in a c-Jun NH2-terminal kinase-1-dependent manner. Am J Physiol Lung Cell Mol Physiol 314, L984-L997 (Jun 1, 2018).

V Acknowledgements

First and foremost, I want to express my sincere gratitude to my supervisor, Dr. Yuval Rinkevich, for his guidance and support during my PhD study. This work could not have been possible without his help. I am very grateful for all the knowledge that he has imparted and the encouragement he has given during my study.

I would like to extend my sincere thanks to Prof. Silke Meiners for the constant support and inputs during the revision of my dissertation. I would like to thank my supervisors Prof.Silke Meiners, Dr. Claudia Staab-Weijnitz, and Dr. Siegfried Ussar, for their untimely support, guidance, and motivation for my project. Their inputs during thesis committee meetings were insightful and helped me progress through the project.

I immensely want to thank Harisha, for his unconditional support, a perfect work life balance throughout my Ph.D. and my little daughter Aaryahi for bearing my absence and understanding. I am indebted to my mother Shubha, father Gopal, family and friends for their everlasting support and care throughout.

It has been my good fortune to work with the best colleagues one can ever imagine I would like to thank my dear friends and lab mates Pushkar, Vijay, Simon, Anna, Aydan, Qing, Li, Donovan, Haifeng, Martin, Tim, Jule, Tankut, Andy, Dongsheng, Shaohua, Adrian, Valeria, Arunima and Asheesh with whom I share endless memories. Further on, I want to convey my deepest gratitude to Sandra, who always helped with administrative work.

Moreover, I want to express my deepest thanks to the CPC research school and HELENA for all the support and training I received. My sincere thanks to my collaborators from the Schiller group- Herbert, Ilias, Meshal for their constant involvement in data analysis. I would also like to extend my gratitude to Theis Group at ICB and Enard group at the LMU for their support.

Last but not least, I want to thank Dr. Steffen Dietzel, BMC-Bioimaging, Dr. Lisa Richter FACS core facility Biomedical center, Dr. Gerald Burgestellat CPC imaging and the Animal facility at Helmholtz Zentrum. I want to acknowledge the funding from Helmholtz Zentrum München for financial support during the study.